UNIVERSITÀ DI PARMA

UNIVERSITA’ DEGLI STUDI DI PARMA

DOTTORATO DI RICERCA IN SCIENZE CHIMICHE

CICLO XXXVI

Salification and cocrystallization to ameliorate physiochemical properties of drugs. Investigation of their interactions inside liposomal formulation with Small Angle X-ray Scattering.

Coordinatore:

Chiar.mo Prof. Alessia Bacchi

Tutore:

Chiar.mo Prof. Luciano Marchiò Luciano Marchiò

Co-Tutore:

Chiar.mo Prof. Alessia Bacchi

Laura Baraldi

Dottorando: Laura Baraldi

Anni Accademici 2020/2021 – 2022/2023

Index

Abstract

The pharmaceutical industry is in a state of constant evolution, driven by the pursuit of innovative strategies to address persistent challenges in drug delivery. These challenges include, on one side, the burning need for more accessible and cost-effective methods to enhance solubility, dissolution rate, and permeability of drugs and, on the other side, the implementation of characterization methods of lipid nanoparticles that has never been so crucial.

In this work, salification of theophylline with squaric acid represents the first step in this direction, addressing the challenges posed by its infamous narrow therapeutic indices. Salification reduces API dissolution by a remarkable 54% within the critical first 10 minutes, simulating a controlled released formulation and therefore better controlling the therapeutic and adverse effects of theophylline.

Meanwhile, the cocrystallization technique is revolutionizing the delivery of caffeine, a psychoactive substance known for its adverse effects like nervousness and anxiety due to unstable blood concentration levels. By co-crystallizing caffeine with various small molecules, solubility, dissolution rate, and permeability can be meticulously modulated. The caffeine-xinafoic acid cocrystal, for instance, significantly lowers caffeine solubility, decreases dissolution rate, and increases permeability, promising a more controlled and efficient caffeine delivery system.

Similarly, we explored the potential of salts and cocrystals to enhance the pharmacokinetics of benzocaine, a widely used local anesthetic. Nine new salts and one cocrystal have been synthesized, each offering substantial improvements in dissolution rates and permeability. These findings not only open avenues for increased bioavailability but also the prospect of extended duration of action for benzocaine.

Diving even deeper into the ability of a counterion to affect the physiochemical properties of a drug, the encapsulation of benzocaine salts into a lipid-base formulation like liposomes has been investigated.

Therefore, liposomal formulations are meticulously characterized using noninvasive techniques like Small-Angle X-ray Scattering (SAXS). Unique drug localization between lipid tails and alterations in liposome arrangement are unveiled. Furthermore, to make these advanced methods more accessible, a simplified SAXS data analysis method, the beating wave approach, is introduced.

This new data analysis method is compared with two different techniques: Fluorescence lifetime imaging microscopy (FLIM) and NanoDSC, both utilized to study all-trans retinoic acid (ATRA) nanoencapsulated in liposomes, and both suggesting interactions between ATRA and the liposomal membrane in good agreement with SAXS data.

In conclusion, these multifaceted innovations in pharmaceutical research promise to revolutionize drug delivery, enhance drug performance, and streamline characterization methods. Our aim is to continuously push boundaries, ushering in a new era of pharmaceutical science that addresses the demands for precision, efficiency, and accessibility in drug development.

Aim and Scope

The aim of this PhD thesis dissertation is to advance pharmaceutical science by addressing key challenges in the delivery of drugs. Indeed, this thesis has a two-fold objective: ameliorating the early pharmacokinetic profile of some model drugs using crystal engineering and, furthermore, assessing the impact of these modification on the drug's interactions inside a lipid base formulation. Focusing on the salification of theophylline with squaric acid, the research targets the enhancement of drug solubility and controlled release, addressing the notorious narrow therapeutic indices associated with theophylline. The application of cocrystallization techniques to caffeine provides a groundbreaking approach to modulate solubility, dissolution rate, and permeability, promising a more controlled and efficient caffeine delivery system. The study extends to benzocaine, a widely used local anesthetic, where the synthesis of new salts and a cocrystal demonstrates significant improvements in dissolution rates and permeability, offering potential advancements in bioavailability and duration of action. Additionally, the investigation delves into the encapsulation of benzocaine salts in lipid-based formulations like liposomes, employing noninvasive techniques such as Small-Angle X-ray Scattering (SAXS) for meticulous but hands-on characterization. The introduction of the beating wave approach for SAXS data analysis provides a simplified method for assessing liposomal formulations, which is compared with Fluorescence Lifetime Imaging Microscopy (FLIM) and NanoDSC in the study of all-trans retinoic acid (ATRA) nanoencapsulated in liposomes. Overall, the thesis contributes multifaceted innovations to pharmaceutical research, with the overarching goal of revolutionizing drug delivery, improving drug performance, and streamlining characterization methods to meet the demands for precision, efficiency, and accessibility in drug development.

Abbreviations

ACN: Acetonitrile

API: Active Pharmaceutical Ingredient

ATRA: All-Trans Retinoic Acid

BB: Benzocaine Benzenesulfonate

BC: Benzocaine Camphorsulfonate

BCS: Biopharmaceutics Classification System

BE: Benzocaine Esylate

BL: Benzocaine-Ligustrazine

BMA: Benzocaine Maleate

BME: Benzocaine Mesylate

BN: Benzocaine Naphthalenesulfonate

BO: Benzocaine Oxalate

BT: Benzocaine Tartrate

BTS: Benzocaine p-Toluenesulfonate

CA-MA: Caffeine - Malonic Acid

CA-MO: Caffeine – Morin

CA-NA H1: Caffeine - Naringin Hydrate 1

CA-NA H2. Caffeine - Naringin Hydrate 2

CA-OX: Caffeine - Oxalic Acid

CA-XA P1: Caffeine - Xinafoic Acid Polymorph 1

CA-XA P2: Caffeine - Xinafoic Acid Polymorph 1

CA: Caffeine

COPD: Chronic Obstructive Pulmonary Disease

DLS: Dynamic Light Scattering

DOTAP: 1,2-dioleoyl-3-trimethylammonium-propane

DPPC: 1,2-dipalmitoyl-sn-glycero-3-phosphocholine

DSC: Differential Scanning Calorimetry

DSPE-PEG2000: 1,2-distearoyl-sn-glycero-3-phosphoethanolamine-N-[succinyl(polyethylene glycol)-2000]

DVS: Dynamic Vapor Sorption

EMA: European Medicine Agency

EtOH: Ethanol

FLIM: Fluorescence Lifetime Imaging Microscopy

FTIR: Fourier Transform Infrared

HB: Hydrogen Bond

LAG: Liquid Assisted Grinding

nDSC: Nano-Differential Scanning Calorimetry

PBS: Phosphate-Buffered Saline

PC: Phosphatidylcholine

PSA: Polar Surface Area

RMSE: Root Mean Square Error

SC-XRD: Single Crystal X-Ray Diffraction

TGA: Thermal Gravimetric Analysis

TLE: Thin-Layer Evaporation

TS3w: Theophylline Squarate Trihydrate

TSan: Theophylline Squarate Anhydrous

USFDA: United States Food and Drug Administration

VH-XRPD: Variable Humidity X-Ray Powder Diffraction

VT-XRPD: Variable Temperature X-Ray Powder Diffraction

XRPD: X-Ray Powder Diffraction

Chapter 1

1. Introduction

1.1. Drug delivery

In the dynamic landscape of modern medicine, the precise and effective delivery of pharmaceutical agents to their intended targets within the body is a cornerstone of therapeutic success. The journey of a drug from its point of administration to its pharmacological impact is a complex interplay of factors encompassing drug delivery strategies, the diverse routes of administration, and the intrinsic physiochemical properties of the drug itself.[1]

Pharmaceutical researchers and clinicians employ a diverse array of routes for drug administration, each tailored to optimize therapeutic outcomes. These routes include oral ingestion,[2] parenteral injections,[3] transdermal patches,[4] inhalation methods,[5] and more (FIGURE 1.1). The selection of the administration route hinges on a nuanced understanding of the drug's target site, its physiochemical characteristics, the desired onset of action, and patient factors such as comfort and compliance.[1]

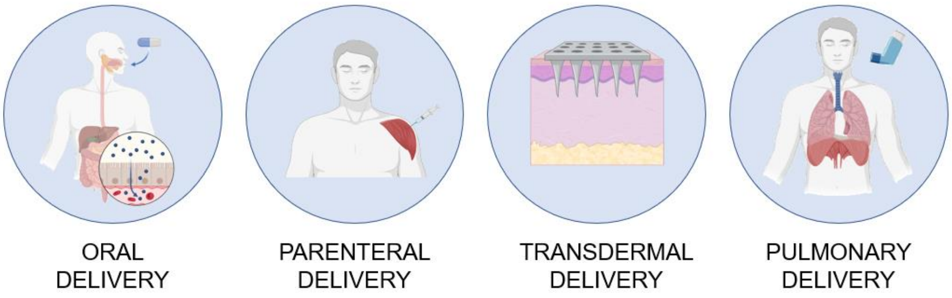

FIGURE 1. 1 *Schematic representation of oral, parenteral, transdermal, and pulmonary delivery. Image produced with Biorender®.*

Central to the successful design of drugs and their delivery systems is a grasp of the drug's physiochemical properties.

The renowned "Rule of 5", a guiding principle in drug discovery, dictates that for optimal oral absorption: a drug's molecular weight should be under 500 Daltons, log P (partition coefficient) under 5, and hydrogen bond donors and acceptors should be limited to 5 and 10 respectively.[6] These properties directly influence a drug's ability to navigate the intricate landscape of biological barriers and interact with targeted receptors. Recently, the “Rule of 5” expansion has been discussed to encompass additional physiochemical parameters to account for more complex interactions between drugs and biological systems.[7]

Indeed, conformational flexibility has been suggested to significantly influence drug properties beyond the Rule of 5 criteria. A robust correlation has been observed between cell permeability and the minimum solvent-accessible 3D polar surface areas (PSA) of the compounds, while aqueous solubility appears to be less depending on specific 3D conformations. Aromatic side chains and dynamically forming intramolecular hydrogen bonds prove particularly effective in conferring "chameleonic" characteristics to compounds, enabling them to simultaneously exhibit both high permeability and solubility.[8]

Within this intricate interplay, solubility, dissolution rate, and permeability emerge as pivotal factors. A drug's solubility can dictate its dissolution, impacting the amount available for absorption. Sluggish dissolution rates can lead to delayed therapeutic effects.[9] Permeability, determining a drug's ability to traverse cellular membranes, affects its systemic availability. Poor permeability can hinder the drug's journey to its target.[10]

A crucial tool in understanding the interplay of these factors is the Biopharmaceutics Classification System (BCS). Categorizing drugs based on solubility and permeability, BCS offers insights into their potential *in vivo* performance. Class I drugs, with high solubility and permeability, typically exhibit superior absorption. As one moves through the classes, formulation strategies need to be tailored to address the challenges posed by reduced solubility or permeability.[11]

As represented in FIGURE 1.2, the success of drug delivery hinges upon an intricate understanding of how the physiochemical properties of a drug orchestrate its journey through various administration routes, its solubility, dissolution rate, and permeability, all harmonized within the framework of the Biopharmaceutics Classification System. This symphony of knowledge empowers pharmaceutical scientists to innovate and optimize drug delivery strategies that achieve therapeutic objectives with precision and efficacy.

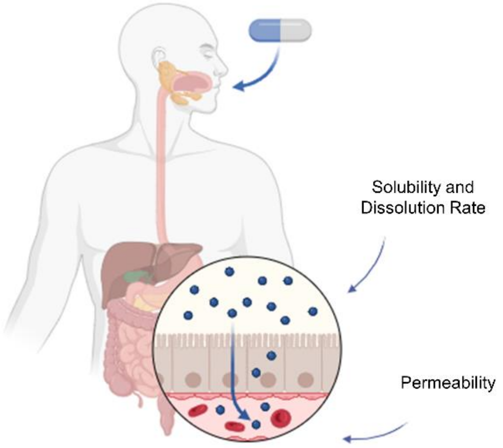

FIGURE 1. 2 *Representation of the oral administration, highlighting the solubility and dissolution steps leading to the absorption of the drug. Image produced with Biorender®.*

1.1.1. Solubility

Solubility, a fundamental physicochemical property of drug molecules, represents the equilibrium between the dissolved and undissolved states in a specific solvent under defined conditions. It is a critical determinant of drug formulation, bioavailability, and systemic exposure; indeed, it dictates the concentration gradient driving dissolution, which influences the rate and extent of drug absorption.[12] Poor solubility can lead to insufficient drug release and subsequent limited absorption, constraining therapeutic effectiveness. Quantitative solubility measurements, often expressed as molarity or mass per unit volume of solvent, serve as a foundational parameter for designing drug delivery systems. Techniques such as solubility enhancement through co-solvents, complexation, particle size reduction, and formulation with lipids are routinely employed to overcome solubility challenges, ultimately optimizing drug dissolution and enhancing therapeutic outcomes.[13]

1.1.2. Dissolution rate

Dissolution rate, a paramount attribute within drug development, characterizes the rate at which a drug substance dissolves from a solid dosage form and enters a solution. This process significantly influences drug bioavailability and subsequent pharmacological response. A high dissolution rate can expedite the availability of drug molecules for absorption, which is especially critical for drugs with limited solubility. Conversely, slow dissolution can impede the therapeutic onset, necessitating prolonged exposure to attain therapeutic levels. Experimental determination of dissolution rate results is often reported as the amount of drug dissolved per unit of time. Formulation strategies, including particle engineering, amorphous solid dispersion, and the use of super disintegrants, can effectively modulate dissolution rates, enhancing the bioavailability and overall efficacy of drug products across various administration routes.[14,15]

1.1.3. Permeability

Permeability, a pivotal parameter in pharmaceutical sciences, delineates the ability of a drug molecule to traverse biological barriers and gain access to systemic circulation. It constitutes a decisive factor governing oral absorption, transdermal delivery, and other administration routes.

Permeability is influenced by physicochemical attributes such as lipophilicity, molecular size, and charge, alongside cellular efflux mechanisms and transporter proteins. A high permeability coefficient facilitates efficient absorption by enabling rapid drug movement across biological membranes, while low permeability restricts passage, potentially limiting bioavailability.[16] Experimental methods like the Caco-2 cell monolayer assay[11] and parallel artificial membrane permeability assay (Permeapad ®)[17] quantitatively assess permeability. Formulation strategies, including prodrugs and permeation enhancers, can be employed to optimize drug permeability, thus facilitating effective drug delivery to target tissues and enhancing therapeutic outcomes.[18]

In this work, a different strategy, crystal engineering, has been used and holds promise in addressing challenges related to solubility, dissolution rate, and permeability of drug molecules. By tailoring crystal structures through precise manipulation of molecular interactions, crystal engineering can lead to modifications in drug properties that influence these key factors.

1.2. Crystal engineering

Crystal engineering was formally defined by Desiraju in 1989 as *"the understanding of intermolecular interactions in the context of crystal packing and in the utilization of such understanding in the design of new solids with desired physical and chemical properties."*[19] Essentially, crystal engineering serves as a potent approach to exert control over the arrangement of molecules and ions in the solid state through non-covalent interactions like hydrogen and halogen bonding, ionic interactions, van der Waals forces, and π-interactions. Indeed, the way building blocks (molecular and/or ionic) are packed in the solid state can profoundly influence the properties of materials. Achieving this ambitious goal necessitates comprehending and, where possible, predicting the spatial distribution and intermolecular interactions of components within the solid.

Apparently, a significant number of materials with practical applications exhibit crystalline properties. Crystals, inherently, are supramolecular entities composed of molecular and/or ionic building blocks. According to Dunitz, *"A crystal is, in a sense, the supramolecule par excellence: a lump of matter, of macroscopic dimensions, millions of molecules long, held together in a periodic arrangement by just the same kind of interactions as are responsible for molecular recognition and complexation at all levels - ion-ion, ion-dipole, dipole-dipole interactions, hydrogen bonding, London forces, and so on".*[20] This characterization positions crystals as "supramolecules," wherein molecules are united through mutual recognition. While molecules are constructed from atoms linked by covalent bonds, the molecules/ions comprising such "supramolecules" are bound by intermolecular interactions.[21] Consequently, the concept of "making crystals by design" epitomizes crystal engineering.[22] Supramolecular chemistry is defined as a discipline extending "beyond the chemistry of the molecule" or as "the chemistry of the intermolecular bond".[23]

In practice, the process of creating crystals resembles traditional chemical experimentation for designing new molecules: modeling a molecule, devising an optimal synthetic pathway, characterizing resultant products, and evaluating their properties.[22] Similarly, the crystal fabrication process necessitates a well-defined project, encompassing the formulation of novel crystalline materials, development of suitable design strategies, characterization of produced materials, and performance evaluation.[22–24] Moreover, just as organic synthesis employs a retrosynthetic approach to formulate synthetic strategies,[25] the creation of crystals similarly engages "supramolecular synthons." These synthons, as defined by Desiraju, are *"structural units within supermolecules which can be formed and/or assembled by known or conceivable synthetic operations involving* *intermolecular interactions".*[21] In essence, supramolecular synthons embody spatial configurations of intermolecular interactions, and the core objective of crystal engineering is to discern and astutely exploit them in material design.

Indeed, the realm of intermolecular interactions plays an essential role in shaping the behavior and properties of matter.

1.2.1. Ionic and Dipolar Interactions

Ionic and dipolar interactions, grounded in Coulombic forces, encompass three key categories: ion-ion (200-300 kJ/mol), ion-dipole (50-200 kJ/mol), and dipole-dipole (5-50 kJ/mol) interactions. Although non-directional, dipole-associated interactions necessitate alignment to optimize attraction and repulsion. Among these, ionic interactions prevail at long ranges due to higher charge densities, exemplified by cation-anion associations.[26,27]

1.2.2. Hydrogen Bonding

Hydrogen bonding, a distinctive subset of dipole-dipole interactions, occurs between proton donors (D) and acceptors (A). This interaction is characterized by donors featuring hydrogen atoms attached to electronegative atoms and acceptors housing electron-rich terminations (4-120 kJ/mol). Hydrogen bonds exhibit directionality, with bond strength correlated to the D-H···A angle. Classifications into strong, moderate, and weak bonds provide insights into their energies and lengths. Hydrogen bonding's geometric attributes, coupled with the prevalence of hydrogen-bearing groups, underlie its prominence in crystal engineering and supramolecular design.[28]

1.2.3. Halogen Bonding

Similar to hydrogen bonding, halogen bonding involves electrophilic regions of halogen atoms interacting with nucleophilic counterparts. Analogous to hydrogen bonds, halogen bonds exhibit directionality, with halogen atoms acting as electron acceptors. The strengths of halogen bonds are modulated by the halogen atom, with iodine forming the strongest bonds (10-150 kJ/mol).[29,30]

1.2.4. π-π Interactions

Aromatic interactions, known as π-π interactions, stem from electrostatic, van der Waals, and charge transfer effects (2-50 kJ/mol). These context-dependent interactions encompass face-to-face and T-shaped arrangements between aromatic rings (FIGURE 1.3). Despite limited theoretical understanding, π-π interactions offer a geometric framework to describe interactions in unsaturated molecules.[31–33]

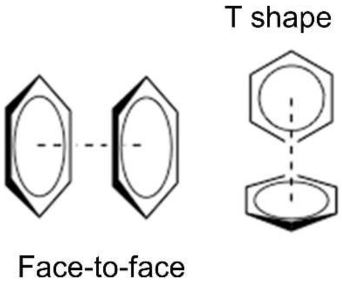

***FIGURE 1. 3** Examples of π-π interactions: fate-to-face and T shape.*

1.2.5. Van der Waals Interactions

Van der Waals interactions arise from electron density fluctuations, contributing to attractive London and Debye forces, and repulsive exchange interactions (<5 kJ/mol). These short-range, non-directional interactions impact molecular arrangements and are pivotal in close packing and crystallization principles.[34]

1.3. Intermolecular interactions in multicomponent crystals

The pursuit of novel solid forms with improved physicochemical attributes, including solubility, intrinsic dissolution rate, morphology, thermal stability, and hydration stability, has led to a significant focus on multicomponent crystalline assemblies. These assemblies offer the potential to finely adjust these critical properties, making them a valuable target in various domains, with pharmaceuticals being of dominant significance.[35,36] Solid-state chemists have at their disposal an array of strategies to manipulate the chemical and physical characteristics of materials of interest. These strategies encompass the generation of salts and co-crystals (FIGURE 1.4).[15]

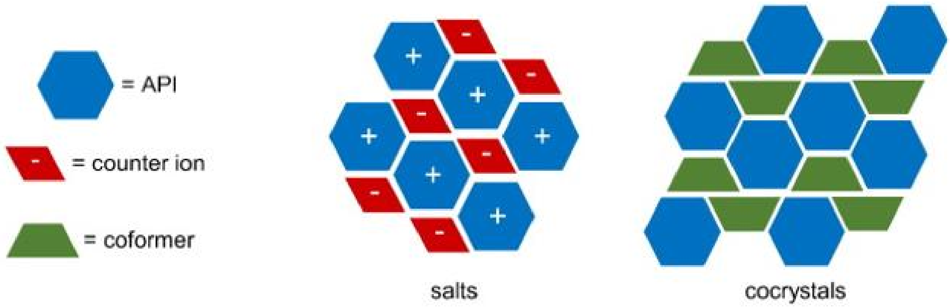

FIGURE 1. 4 *Arrangement of salts and cocrystals showcasing the interaction between the Active Pharmaceutical Ingredient (API) and the counterion or coformer.*

1.3.1. Salts

In the domain of generating multicomponent crystalline solids enriched with augmented attributes, a well-explored pathway involves the formation of salts. While enhancing aqueous solubility is a prominent motive behind adopting salt formation strategies, pharmaceutical enterprises utilize the creation of distinct salt derivatives to tackle a diverse array of physicochemical and biological challenges.[37–39] The significance of salt forms is underscored by the fact that around 50% of the drugs approved by the United States Food and Drug Administration (US FDA) are in the form of active pharmaceutical ingredients (APIs) as salts.[40] Moreover, a substantial portion of the top 200 prescription drugs in the United States are composed of pharmaceutical salts.[41] This strategic maneuver hinges upon the presence of ionizable functional groups within the compound of interest. Salts materialize by coupling the active pharmaceutical ingredient (API) with a suitable counterion, typically derived from inorganic or organic acids or bases. This process results in creating an ionic compound, where the API's ionizable moieties interact with the counterion to yield a stable crystalline structure. Such interactions are often complemented by hydrogen bonding or coordination interactions, potentially leading to charge-assisted hydrogen bonding scenarios.[39]

1.3.2. Cocrystals

Cocrystals denote crystalline materials wherein two or more distinct molecules, encompassing the drug and coformers, coexist within the same crystal lattice.[42] In the pharmaceutical realm, cocrystals have garnered immense significance due to their capacity to finely adjust the physicochemical attributes of drugs.[43] Esteemed regulatory bodies, such as the United States Food and Drug Administration (USFDA) and the European Medicine Agency (EMA), have distinctly defined pharmaceutical cocrystals.[44,45] According to the USFDA, cocrystals are characterized as "crystalline materials composed of two or more molecules in the same crystal lattice".[44] Conversely, the EMA defines cocrystals as "homogeneous (single phase) crystalline structures made up of two or more components in a definite stoichiometric ratio, where the arrangement in the crystal lattice is not predicated on ionic bonds, as is the case with salts".[45] The stabilization of cocrystals primarily hinges on robust intermolecular non-covalent adhesive interactions of short-range order,[46] manifesting between the drug and coformer molecules. The inception of cocrystals traces back to the pioneering work of Friedrich Wohler in 1844, who synthesized the first documented cocrystal, quinhydrone, utilizing benzoquinone and hydroquinone.[47] Remarkably, this milestone marked the first cocrystal structure recorded in the Cambridge Structural Database.[48] The triumphant formation of cocrystals during a cocrystallization event pivots upon the orchestration of intermolecular interactions,[49] structural compatibility,[50] and the precise stoichiometry of API and coformer molecules.[51]

Chapter 2

2. Theophylline *in vitro* release modulation by salification with squaric acid

2.1. Introduction

Theophylline belongs to the xanthine, which are classified as alkaloids, exerting mild stimulant effects and acting as bronchodilators. Theophylline, indeed, displays an anti-inflammatory impact on conditions like asthma and COPD at lower dose.[52]

The mechanism of action attributed to theophylline involves the inhibition of phosphodiesterase, a key factor in smooth muscle relaxation. However, theophylline is renowned for its narrow therapeutic index (ranging from 30 to 100 μM), stemming from its notably low selectivity. Impressively, concentrations as low as 110 μM can trigger an array of adverse reactions, including nausea, metabolic acidosis, and arrhythmias.[53]

Therefore, even though it proves effective as an active pharmaceutical component, theophylline is not the favored option in managing asthma. Typically, it is delivered orally through slow-release formulations in chronic therapies, often combined with a short-acting β2-agonist, a long-acting β2 agonist, or an inhaled corticosteroid.[54–56]

Significant efforts have been devoted to optimizing theophylline's absorption profile within the formulation field. Exemplary studies by Pezoa et al.,[57] Rodrigues et al.,[58] and Jian et al.[59] underscore the considerable endeavor to enhance *in vivo* performance. These investigations involve formulation modifications utilizing excipients like Eudragit or nanoparticles to extend therapeutic effects and ameliorate adverse reactions.[60] During the formulation optimization process, numerous considerations come into play,[61] encompassing the roles of individual components and their impacts on final delivery or developability. Equally crucial are the interactions between excipients and the API, as well as interactions among different excipients. Potential drawbacks include drug hydrolysis, ion interactions creating less soluble forms, or physical issues such as API adsorption onto excipient surfaces.[62]

This study employs a distinct approach to tailor the properties of theophylline, employing a salification technique with squaric acid to control and reduce its dissolution rate and therefore, potentially ameliorate its pharmacokinetic profile, better controlling the administrated dose and avoiding the undesirable side effects.

Squaric acid, a potent acid within the oxocarbon family,[63] stands out for its distinctive physical attributes[64] and its utilization in dye synthesis.[65,66] While squaric acid derivatives have garnered interest in fields such as immunosensitizers,[67] enzyme inhibitors, and receptor antagonists,[68] its application in forming API salts remains unexplored. The choice of squaric acid as a salt-forming agent was guided by crystal engineering principles, taking into account its notable acidity (with pKa values of 0.6 and 3.4),[69] symmetric nature, and the tendency to form layered hydrogen-bonded structures,[70,71] which harmonize effectively with predominantly planar molecules like xanthines.

In typical cases seeking improved pharmacokinetic feature of a drug, hydrate forms are generally discouraged due to their heightened thermodynamic stability leading to slower dissolution profiles.[72,73] However, this unique scenario presents an opportunity, as the hydrate form could offer better control over drug release. Furthermore, the salification process might prove more expedient than extensive formulation development. Once synthesized, the salt can be incorporated into known manufacturing procedures, including traditional tablets and capsules. While certain theophylline salts have been examined,[74,75] specific systems designed to enhance bioactivity[76] or stability[77] generally exhibit greater solubility than theophylline alone. Consequently, this study introduces a novel application of salification to theophylline with the aim of addressing therapeutic index concerns, marking a noteworthy innovation.

2.2. Materials and Method

2.2.1. General

Theophylline and Squaric acid were used as received from MERCK-Sigma Aldrich. Tetrahydrofuran (THF), Diethyl Ether and Ethanol were commercially available and used without any other purification. Water was used after filtration with Milli-Q Advantage A10 technology from Millipore.

2.2.2. Theophylline squarate

The bulk powder of the hydrate form (TS3w) was obtained via LAG (liquid assisted grinding). Theophylline and Squaric Acid were weighed in an equimolar ratio (1:1, total mass 163 mg), the sample was transferred to a 4.0 mL vial with three grinding balls (5 mm ϕ, zirconia type) and the desired solvent was added (20 µL of water Milli-Q). Then, the mixture was ground for 1h using a multi-sample vibrating ball mill (Pulverisette 6 – Fritsch, Germany) under a rotational speed of 300 rpm and a temperature of 25 °C.

Along with TS3w, an anhydrous form was obtained (TSan). In order to obtain TSan, Theophylline (100 mg) and Squaric Acid (63 mg) were both dissolved in water (10 ml) at room temperature and lyophilized. An amorphous powder was obtained and crystallized through slurry in acetone 10 mg/mL at room temperature for three days.

2.2.3. Single-crystal X-ray diffraction (SC-XRD)

Crystals of TS3w suitable for SC-XRD analysis were obtained alternatively from slow evaporation of an EtOH solution of TS3w and from stratification of Diethylether over an EtOH solution of TS3w.

Single crystal data were collected at 220K with a Bruker D8 Venture diffractometer equipped with a Photon II detector, using a CuKα microfocus radiation source (λ = 1.54184 Å). The intensity data were integrated from several series of exposure frames covering the sphere of reciprocal space. Data reductions were performed with APEX3. Absorption corrections were applied using the program SADABS.[78] The structures were solved by intrinsic phasing with the program SHELXT. Fourier analysis and refinement were performed by the full-matrix least-squares methods based on F^2 using SHELXL-2014,[79,80] implemented in Olex2 software.[81] Non-H atoms were refined anisotropically, and H atoms were placed in calculated positions and refined with a riding model. Crystallographic data can be found in Chapter 2.5, TABLE S1.

CCDC 2124344 contains the supplementary crystallographic data for this paper.

2.2.4. X-ray powder diffraction (XRPD)

The crystalline state of samples was investigated by X-ray powder diffraction (XRPD) with an Emyrean Panalytical V 2.0 instrument equipped with Cu radiation source. Samples were placed on zero background sample holders. The measurements were performed in reflection mode with 2Theta scans from 1.5 to 45°, step size 0.02°, soller slit 0.02 rad, divergence slit 1/8°, antiscatter slit 1/4°. The variable temperature and humidity XRPD analyses were carried out with an Anton Paar CHC+ camera equipped with CCU100 temperature control and MHG-32 humidity generator. The measurements were performed in reflection mode, 2Theta scan from 1.5 to 45°, step size 0.02°, soller slit 0.02 rad, divergence slit 1/8°, antiscatter slit 1/4°.

2.2.5. Differential scanning calorimetry (DSC)

DSC analyses were performed using a routinely calibrated TA Instruments differential scanning calorimeter Discovery equipped with a computer analyzing system (TRIOS). Indium standard and a sapphire disk were used for temperature/enthalpy calibration and heat capacity calibration, respectively. The system was equipped with a refrigerated cooling system (RCS90) accessory under a dry nitrogen purge (50 mL/min). About 1-5 mg of each sample were placed into a Tzero Aluminum hermetic DSC pan covered with a lid. The sample cell was equilibrated at 0 °C and heated under a nitrogen purge (50 mL/min). All samples were given similar thermal histories by linearly heating to 300 °C at a heating rate of 10 °C/min.

2.2.6. Thermogravimetric Analysis (TGA)

TGA analyses were performed using a TA Instruments Discovery equipped with a computer analyzing system (TRIOS). About 2 mg of each sample were placed into a Platinum 100 µl pan. Heating rate was 10 °C/min to 300 °C.

2.2.7. Dynamic Vapour Sorption (DVS)

Moisture sorption/desorption data were collected on a TA Instruments Vapor Sorption Analyzer Q5000SA. First step: sorption data was collected in the range 40% to 90% relative humidity. Second Step: desorption, sorption and desorption data were collected over a range of 0% to 90% relative humidity (RH) at 10% RH intervals under a nitrogen purge. Samples were not dried prior to the analysis. Equilibrium criteria used for analyses were less than 0.100% weight change in 20 minutes, with a maximum equilibration time of 1 hour if the weight criterion was not met. Data were not corrected for the initial moisture content of the samples. NaBr was used as humidity verification.

2.2.8. Dissolution studies

Dissolution studies of theophylline and theophylline squarate trihydrate were carried out using water Milli-Q (pH 5.5) at room temperature.

8 suspensions at a concentration of 1.5 mg/mL were prepared for both theophylline and theophylline squarate trihydrate. Each suspension corresponds to a different time point (1min-2min-4min-6min-8min-10min-15min-30min). From each sample 200 µL were taken at the corresponding time point and filtered. 20 µL from each taken solution were then diluted (1:10) with H2O and injected.

Ultra-high-performance liquid chromatography with ultraviolet detection (UHPLC-UV) was used for quantitative analysis of the dissolved drug which absorb UV-light in the range of 200–290 nm with an absorbance maximum at 254 nm. UHPLC-UV analysis was conducted on a Waters Acquity UPLC system that was connected to a diode array detector and equipped with a reversed phase Kinetex® EVO C8 LC-column (100 × 2.1 mm; particle size 1.7 µm; pore size 100 Å, Phenomenex®). The mobile phase consisted of 25 mM of ammonium formiate buffer (pH 3) and 0.1% formic acid in acetonitrile, the flow rate was 0.5 ml/min and the column oven was set to 50°C. The injection volume was 2 µL.

2.3. Results

2.3.1. Single crystal molecular structure

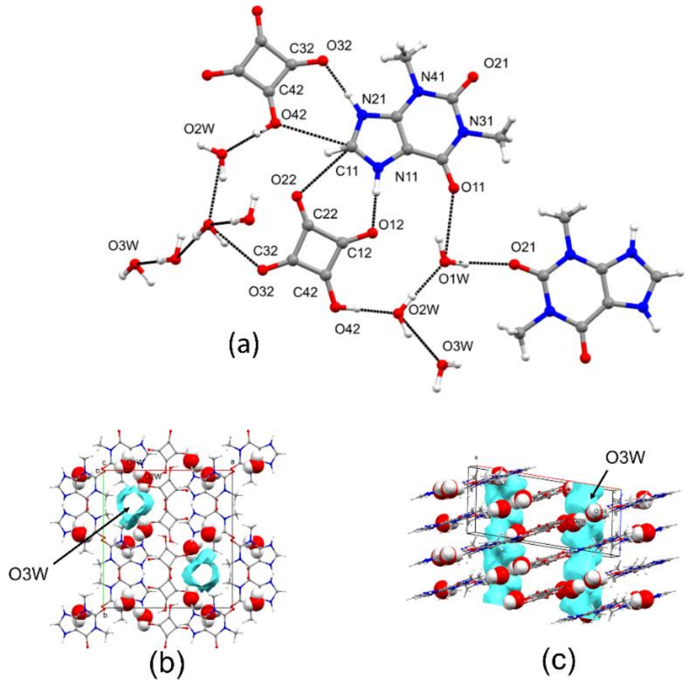

FIGURE 2. 1 *Molecular structure of Theophylline squarate trihydrate with thermal ellipsoids plotted at the 30% probability level* ***(a)****. The water channel embedding O3W is oriented along the c-axes* ***(b)*** *and along a diagonal direction* ***(c)****.*

The asymmetric unit of the crystal structure is composed of one molecule of theophylline, one molecule of squaric acid, and three water molecules (refer to Chapter 2.5 - FIGURE S8). The interactions within the crystal lattice are characterized by multiple hydrogen bonds (HBs) involving these constituents (N11⋯O12, 2.63 Å; N21⋯O32, 2.64 Å; C11⋯O22, 3.03 Å; C11⋯O42, 3.12 Å). Specifically, the theophylline molecule engages in hydrogen bonding with two squarate anions via its N11, N21, and C11 atoms. Notably, a bifurcated hydrogen bond is formed by C11 with two squarate anions. Additionally, the oxygen atoms O11 and O21 of theophylline act as hydrogen bond acceptors, interacting with two symmetry-related water molecules, namely O1W and O2W. The interactions between these components are further facilitated by a network of hydrogen bonds, including two water molecules (O1W and O2W). O1W participates in three hydrogen bonds, serving as both a donor and acceptor (ranging from 2.74 Å to 2.92 Å). Similarly, O2W engages in three hydrogen bonds, acting as a donor and acceptor (ranging from 2.53 Å to 2.82 Å). O3W forms hydrogen bonds as a donor with a symmetry-related molecule (at a distance of 3.31 Å) and with O32 of a squarate anion (at a distance of 2.84 Å), while also accepting a hydrogen bond from O2W (at a distance of 2.82 Å), as depicted in FIGURE 2.1. Conversely, O3W is situated within a channel-like cavity. Interestingly, its weaker hydrogen bonding interactions, evident from the elongated distances, suggest a looser binding to the surrounding molecules, as shown in Chapter 2.5 - FIGURE S8.

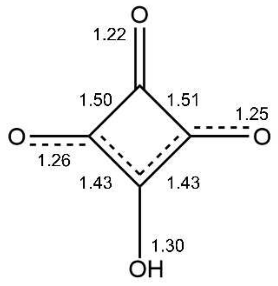

FIGURE 2. 2 *Resonance structure of monodeprotonated squarate anion with bond distance (Å) indicated.*

Among the carbon-oxygen (C-O) bonds within the structure, the C42-O42 bond stands out as the longest, representing the sole pure single bond of this type. In contrast, the C22-O22 bond emerges as the shortest, signifying the only pure double bond within the structure. The remaining two C-O bonds exhibit intermediate lengths, characterized by a partial double bond character.[82] Consequently, the C32-C42 and C42-C12 bonds are the shortest covalent bonds due to their association with a partial double bond character (FIGURE 2.2).

The arrangement of water molecules in the network also imparts distinctive characteristics to the structure. As mentioned earlier, O3W occupies a channel that extends parallel to the c-axis (refer to FIGURES 2.1b and 2.1c). Notably, O3W displays the most relaxed binding with its surroundings, suggesting that it is likely to be the first molecule to depart the structure upon dehydration. This deduction finds support in calorimetric analysis, as elaborated further below.

2.3.2. Thermal and structural characterization

A Variable Temperature - X-ray Powder Diffraction (VT-XRPD) experiment was conducted on TS3w, involving a gradual increase in temperature from 25 °C to 70 °C, 120 °C, 155 °C, and finally 190 °C, as depicted in FIGURE 2.3. Remarkably, upon water removal at 120 °C, the structure does not collapse nor transform into the anhydrous form TSan. Instead, it disassembles into its original constituents. Notably, a distinctive diffraction peak emerges at elevated temperatures (155 °C - 190 °C), attributed to a distinct polymorph of theophylline (elusive form V).[83] Nonetheless, by the experiment's conclusion, theophylline is readily discernible, and no diffraction lines characteristic of the TS3w pattern are detected.

Thermogravimetric analysis (TGA) performed on TS3w (refer to Supplementary Materials, Chapter 2.5 - FIGURE S2) unveils a two-stage weight loss as temperature rises. The initial stage is likely indicative of the removal of channel-water molecule O3W, followed by the second stage, which can be interpreted as the departure of the other two molecules, consistent with the respective weight changes (5.4% and 10.2%). The differential scanning calorimetry (DSC) thermogram (refer to Supplementary Materials, Chapter 2.5 - FIGURE S1) reveals two endothermic peaks at 68.9 °C and 89.6 °C, aligned with the two TGA events. VT-XRPD experimentation substantiates the structural integrity at 70 °C. As detailed earlier, the disruption of the salt structure only occurs once all water molecules have dissociated from the hydrogen-bond network (> 70 °C), interlinking theophylline and squarate. The ensuing exothermic event around 138.0 °C likely corresponds to the reorganization of the molecules into their respective components, as illustrated in FIGURE 2.3. The melting point of TS3w at 227.7 °C coincides with the melting point of the anhydrous form (see DSC thermogram of TSan in Supplementary Materials, Chapter 2.5 - FIGURE S5), hinting at the prior crystallization of TSan, potentially coinciding with the detection of the second exothermic peak (170.5 °C).

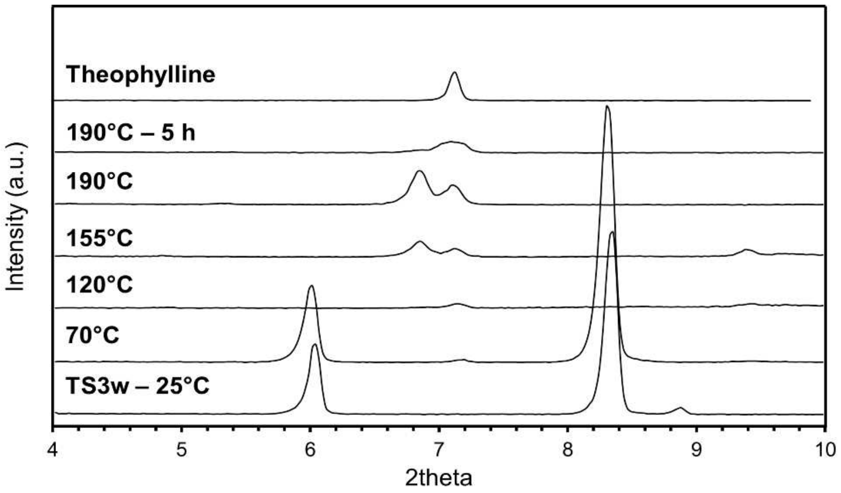

FIGURE 2. 3 *VT-XRPD of Theophylline Squarate trihydrate starting from 25°C to 190°C. Above the reference Theophylline.*

Additionally, a Variable Humidity - X-ray Powder Diffraction (VH-XRPD) experiment was conducted. Theophylline and squaric acid powders (in a molar ratio of 1:1) were combined and subjected to an environment with 95% relative humidity (RH) for a duration of 3 days, as illustrated in FIGURE 2.4.

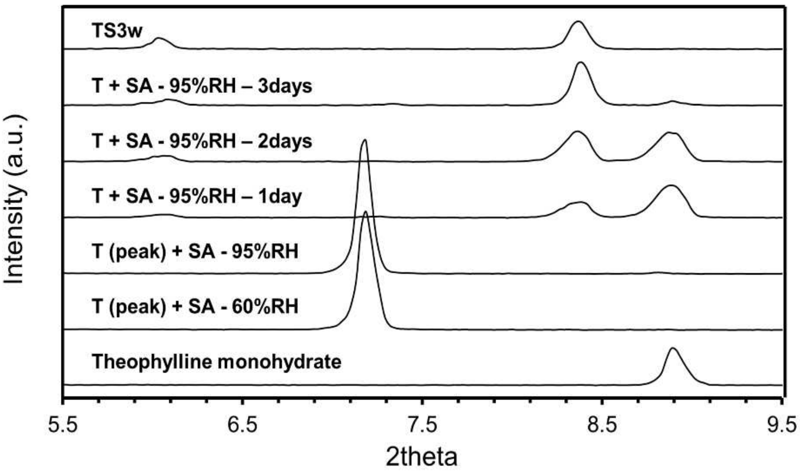

***FIGURE 2. 4** VH-XRPD of Theophylline (T) and Squaric Acid (SA). Theophylline monohydrate and Theophylline squarate trihydrate (TS3w) are reported at the bottom and top, respectively.*

These experiments provided supporting evidence for the formation of salts between the two substances in a humidity chamber through a solid-state mechanism, eliminating the need to dissolve the components in large quantities of solvents or resort to energy-intensive milling procedures. This remark is in perfect agreement with the results obtained from the Variable Temperature - X-ray Powder Diffraction (VT-XRPD) study.

Moreover, in tandem with the formation of the salts, a rapid augmentation in theophylline monohydrate content was discerned. Nonetheless, over time, the signal of the monohydrate subsided while the peak intensity of TS3w ascended. A conjecture can be put forth suggesting that the creation of theophylline monohydrate constitutes an essential preliminary phase in the salt formation process. This inference is substantiated by the VH-XRPD analysis of pure Theophylline, which displays the initiation and completion of the monohydrate transformation within a span of less than eleven hours (Supplementary Materials, Chapter 2.5 - FIGURE S9). The VH-XRPD experiment, albeit informative, did not allow us to observe the full transformation into the pure theophylline salt, likely due to the limitations of mixing the powder during the experiment, as the sample was positioned on a zero-background XRPD sample stage.

Confirmation of salt formation was further obtained through Fourier Transform Infrared (FTIR) analysis, which displayed the signal of protonated nitrogen, providing additional validation of the process (See Supplementary Materials, Chapter 2.5 - FIGURE S7).

Dynamic Vapor Sorption (DVS) measurements on TS3w (See Chapter 2.5 - FIGURE S3) indicated that it could be deemed a stable form. After subjecting it to cycles of varying humidity levels, the XRPD pattern remained consistent, affirming the enduring crystallinity of the powder (See Supplementary Materials, Chapter 2.5 - FIGURE S4). This reiterated the notion that the anhydrous form might be considered as a metastable variant.

FIGURE 2.5 illustrates the distinct powder patterns of commercial Theophylline, Squaric acid, Theophylline squarate trihydrate (TS3w), and Theophylline Squarate anhydrous (TSan). Thermogravimetric analysis conducted on TSan revealed negligible weight loss (See Supplementary Materials, Chapter 2.5 - FIGURE S5-S6).

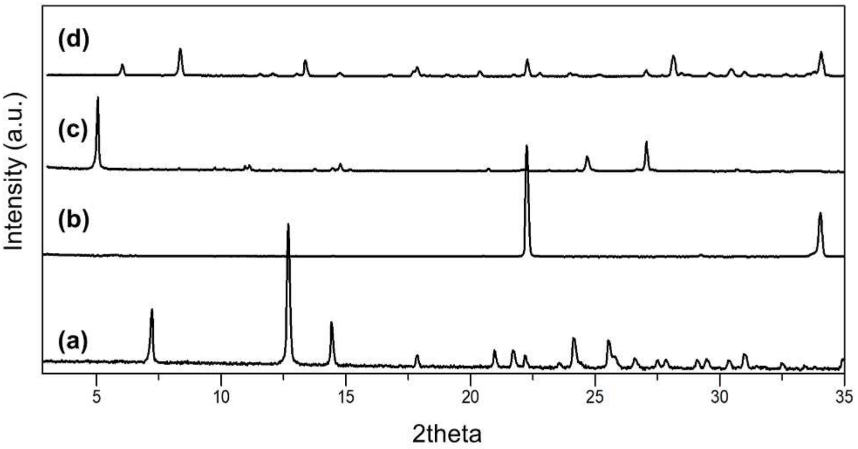

FIGURE 2. 5 *Powder X-ray diffraction of Theophylline (a), Squaric acid (b), Theophylline Squarate anhydrous (TSan, c) and Theophylline squarate trihydrate (TS3w, d).*

2.3.3. Dissolution studies

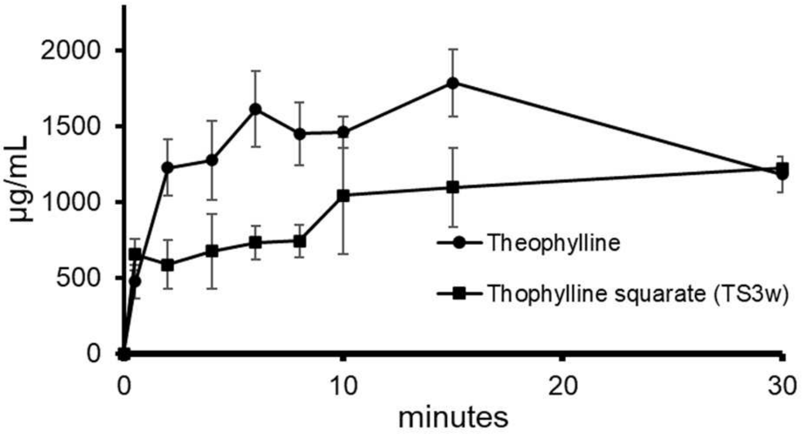

FIGURE 2. 6 *Dissolution study of Theophylline (squares) and Theophylline Squarate trihydrate (rounds).*

Dissolution investigations were undertaken to assess whether the process of salification could potentially enhance the pharmacokinetic profile during the dissolution phase (FIGURE 2.6). Theophylline is known for its high bioavailability, primarily attributed to its swift and effective dissolution rate. Consequently, our emphasis was on attaining a more gradual dissolution process to enhance our ability to regulate the drug's release into the bloodstream. This adjustment is intended to reduce potential adverse effects as we approach the therapeutic dosage.

The outcomes of these studies unveiled a notably improved dissolution behavior for the salt when contrasted with the base alone, resulting in a reduction of 52% at 2 minutes, 54% at 6 minutes, and 38% at 15 minutes for TS3w. This significant improvement shows potential for translating into better in vivo outcomes, enabling finer management of the administered medication concerning therapeutic advantages and the possibility of unwanted side effects. Such control becomes particularly valuable in scenarios with narrow therapeutic indices, a characteristic exemplified in the case of Theophylline.

2.4. Conclusion

Theophylline underwent a salification process with squaric acid, resulting in the formation of two distinct forms: anhydrous theophylline squarate and theophylline squarate trihydrate. A comprehensive analysis, including thermal studies and Variable Humidity (VH-XRPD) and Variable Temperature (VT-XRPD) experiments, enabled the characterization of the stability of TS3w and the evolution of these different forms. Significantly, TS3w exhibited remarkable stability up to 70 °C, only dissociating into its initial components at temperatures exceeding 70 °C. This property renders it suitable for various pharmaceutical processes, including tablet manufacturing.

Furthermore, when theophylline and squaric acid were combined independently in a high humidity environment, salt formation was observed.

In the context of dissolution studies, TS3w demonstrated a substantial reduction in the amount of drug dissolved in the medium over time. This characteristic offers a valuable strategy to finely control the administered dose, effectively mitigating adverse effects while preserving therapeutic efficacy.

In conclusion, the salification of theophylline emerges as a valuable and versatile strategy for modifying its physicochemical properties. This approach can be considered an alternative method for achieving controlled drug release, with significant implications for pharmaceutical applications.

2.5. Supporting Information

Crystal data	
Empirical formula	$C_{11}H_{16}N_4O_9$
Formula weight	348.28
Temperature/K	150.0
Crystal system	monoclinic
Space group	$P2_1/c$
a/Å	14.8686(7)
b/Å	15.1485(7)
c/Å	6.5200(3)
α/°	90
β/°	97.598(4)
γ/°	90
Volume/Å^3	1455.65(12)
Z	4
ρ_{calc}g/cm^3	1.589
μ/mm^{-1}	1.217
F(000)	728.0
Crystal size/mm^3	0.21 × 0.11 × 0.05
Radiation	CuKα (λ = 1.54184 Å)
2Θ range for data collection/°	5.834 to 141.292
Index ranges	$-18 \leq h \leq 18, -18 \leq k \leq 18, -7 \leq l \leq 7$
Reflections collected	27139
Independent reflections	2695 [R_{int} = 0.1182, R_{sigma} = 0.0519]
Data/restraints/parameters	2695/1/256
Goodness-of-fit on F^2	1.054
Final R indexes [I>=2σ (I)]	R_1 = 0.0790, wR_2 = 0.1973
Largest diff. peak/hole/e Å^{-3}	0.49/-0.37

***TABLE S1**. Summary of crystallographic data for Theophylline Squarate trihydrate (TS3w).*

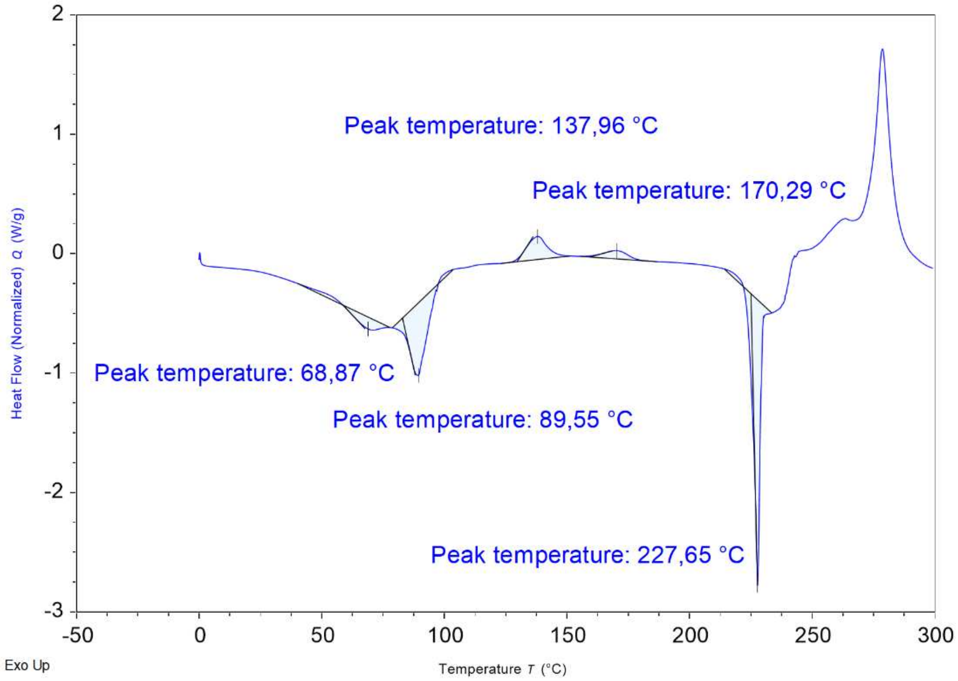

FIGURE S1. *DSC thermogram of TS3w (10°C/min).*

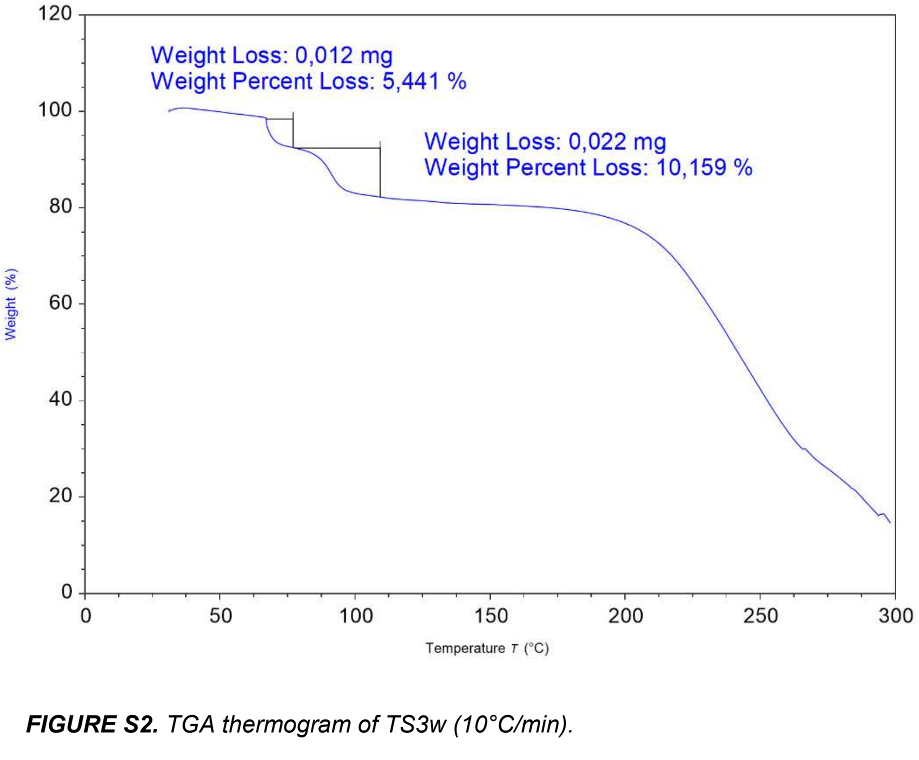

FIGURE S2. *TGA thermogram of TS3w (10°C/min).*

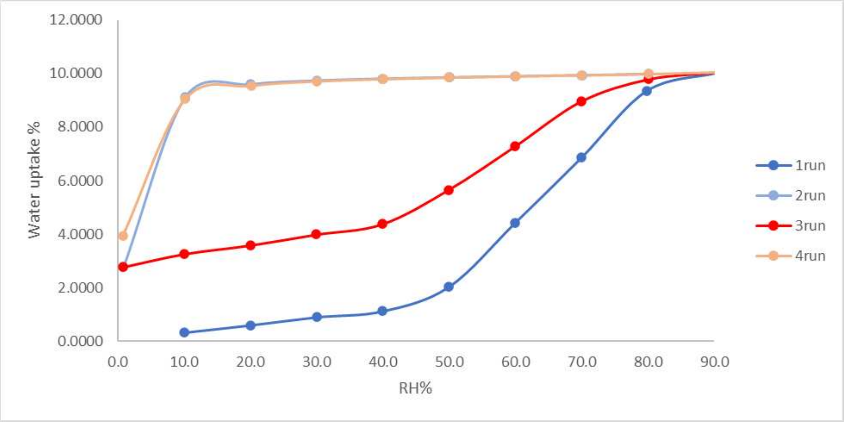

FIGURE S3. *DVS of TS3w. The hysteresis represents the gain and the loss of the channel water molecule.*

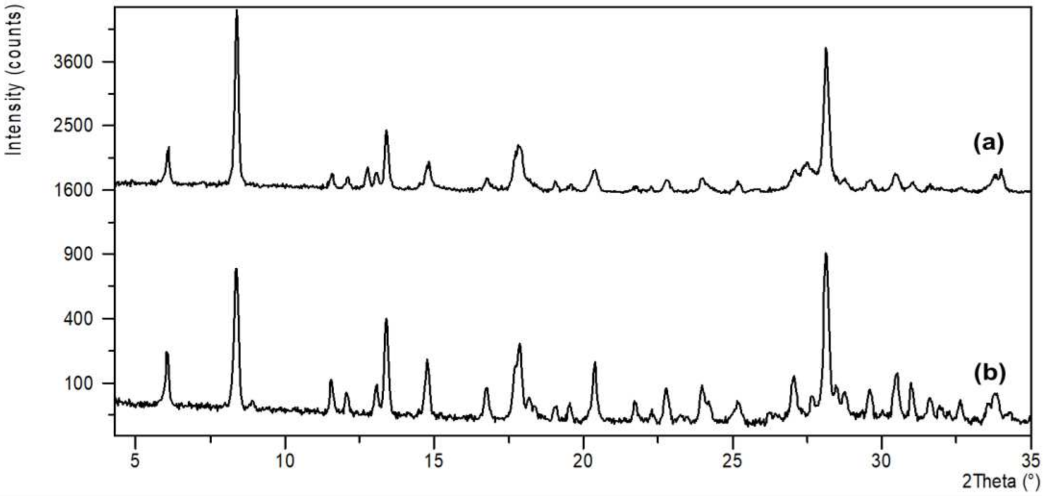

FIGURE S4. *XRPD of TS3w after DVS* ***(a)*** *compared to its pattern before DVS* ***(b)****.*

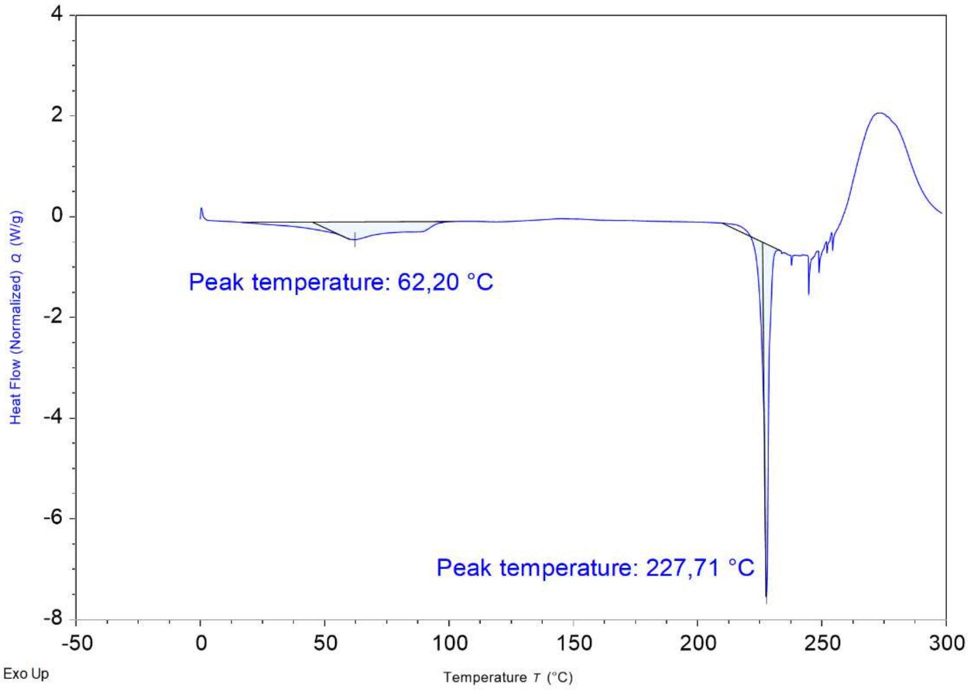

FIGURE S5. *DSC thermogram of TSan (10°C/min).*

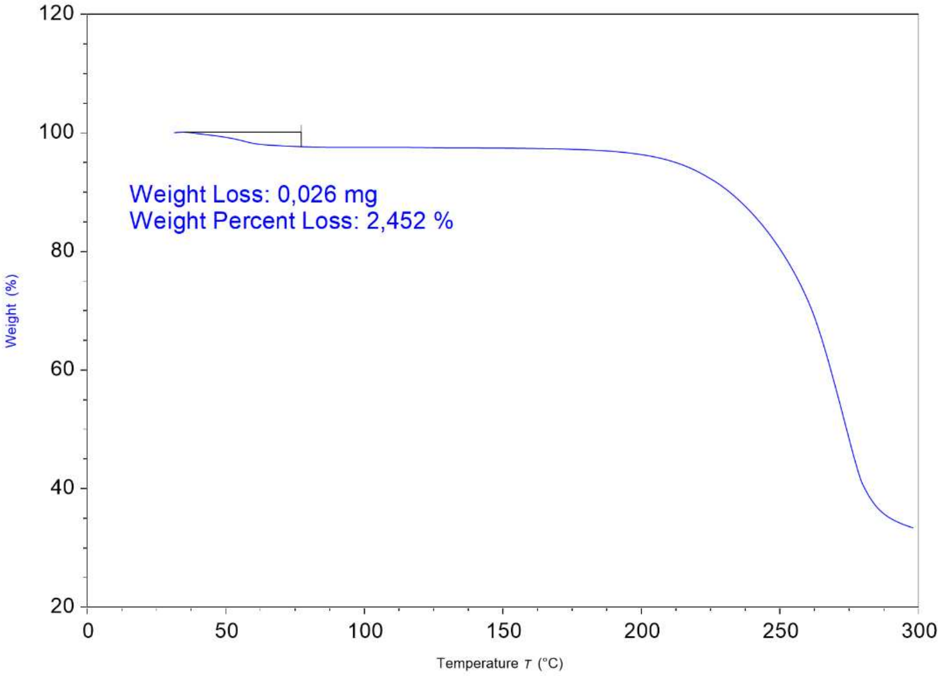

FIGURE S6. *TGA thermogram of TSan (10°C/min).*

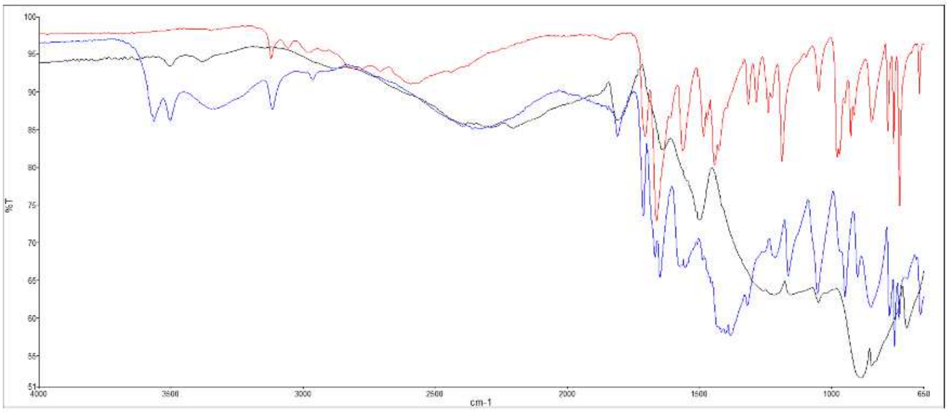

FIGURE S7. *FTIR spectra of Theophylline (red), Squaric Acid (black) and Theophylline squarate trihydrate (blue).*

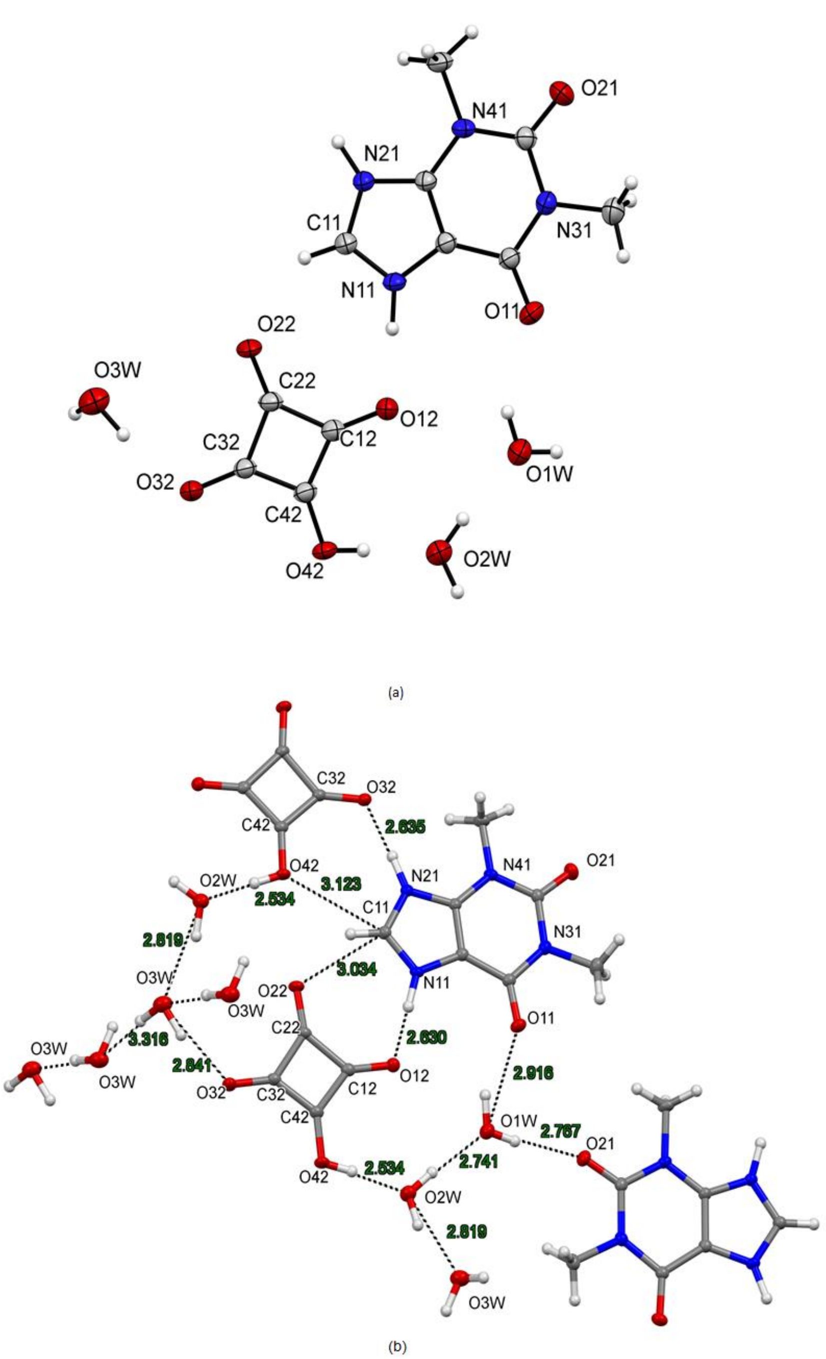

FIGURE S8. *Asymmetric unit of Theophylline squarate trihydrate* ***(a)*** *and molecular structure highlighting the HB connections and distances* ***(b).***

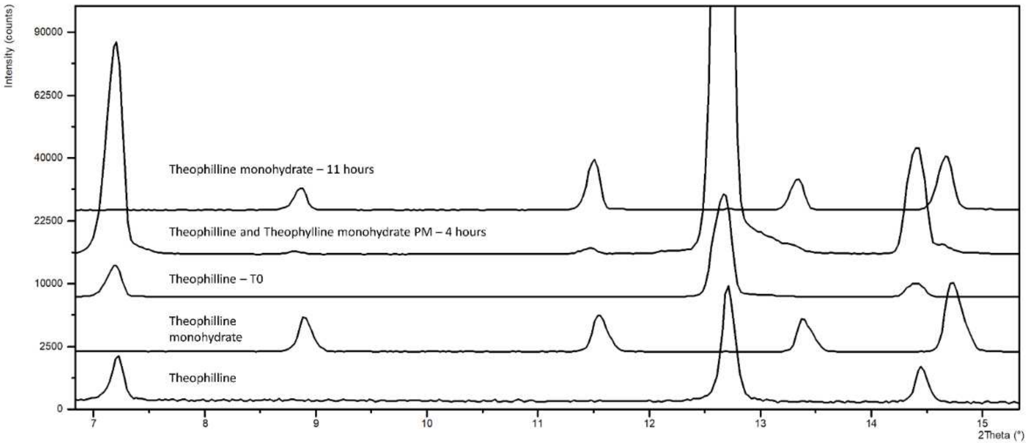

FIGURE S9. *VH-XRPD of pure Theophylline.*

Chapter 3

3. Cocrystallization of Caffeine with Carboxylic Acid and Flavonoids. *In vitro* study to control the “Caffeine crash”

3.1. Introduction

Caffeine, a well-known stimulant,[84] is valued for enhancing alertness, attention, and concentration. It falls into Class I of the Biopharmaceutics Classification System (BCS), indicating high solubility and permeability, desirable traits for active pharmaceutical ingredients (APIs).[85–87] However, conventional caffeine administration can result in negative mood swings, anxiety, and a "jolt and crash" effect due to rapid spikes and drops in bloodstream concentration.[88] Concerns about caffeine addiction, even among young individuals, have also surfaced.[89]

To address these pharmacokinetic challenges,[90,91] strategies for sustained caffeine release have been explored, including controlled-release formulations and innovative platforms like spray-dried or lipid nanoparticles.[92–94] However, these approaches can be complex, time-consuming,[95] and prone to unexpected interactions between the drug and excipients,[96] as well as issues related to drug polymorphism.[97,98]

An alternative strategy involves cocrystallization, wherein caffeine is combined with a coformer to create a cocrystal. This approach simplifies drug product development, as it eliminates the need for complex formulation engineering (FIGURE 3.1). Cocrystallization can significantly improve *in vitro* performance metrics such as solubility, dissolution rate, permeability, and ultimately, bioavailability.[15]

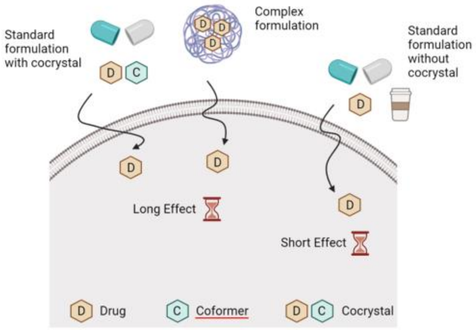

***FIGURE 3. 1** Comparison between the controlled release of caffeine with the immediate release of caffeine alone or as a cocrystal made of the drug (D) and the coformer (C). Biorender® was used to produce the image.*

Indeed, caffeine can interact with various classes of molecules (coformers) through weak interactions, including hydrogen bonds, π-π stacking, CH-π interactions, and halogen bonds. The judicious selection of coformers capable of complementary interactions with caffeine falls within the domain of crystal engineering. This approach allows for the exploration of numerous cocrystal combinations, streamlining drug development.[99–101]

Several caffeine cocrystals have been synthesized previously using different coformers, such as carboxylic acids[102–104] and flavonoids.[105,106] In this study, various small molecules were chosen as coformers for caffeine, each selected for its potential to interact with caffeine through carboxylic groups, hydroxyl groups, and aromatic moieties. The aim was to modulate caffeine's properties through cocrystallization and investigate their solid-state characteristics, solubility, dissolution rate, and permeability.

The study involved seven cocrystals, including caffeine-oxalic acid,[102] caffeine-malonic acid,[107] caffeine-xinafoic acid polymorph 1,[108] caffeine-xinafoic acid polymorph 2,[109] as well as new systems encompassing caffeine-naringin hydrate form 1, caffeine-naringin hydrate form 2, and caffeine-morin. The coformers were chosen to represent a range of molecular complexities and predictable lipophilicities, targeting the modulation of caffeine's properties through cocrystallization. Moreover, their interesting activities to be coupled with caffeine was considered: naringin is a flavanone-7-O-glycoside recently reckon as a potential anticancer,[110] while morin is an anti-inflammatory and anti-oxidant molecule.[111]

The seven cocrystals underwent analysis to evaluate their solid-state characteristics and preliminary pharmacokinetic features such as solubility, dissolution rate, and permeability. While solubility and dissolution rate are generally more straightforward to interpret, permeability can present critical interpretative challenges. Permeability assessment necessitates both solubility and dissolution profiles, as proper dissolution kinetics and absorption are crucial for the drug to effectively reach its active site. Problems can arise when the drug is absorbed too rapidly or too slowly, excessively, or inadequately.[112,113] This issue is particularly pertinent for drugs with slow and poor absorption, but caffeine exhibits the opposite behavior. In Chapter 2,[113] we managed to reduce theophylline's dissolution rate by up to 54% in the initial minutes through crystallization with squaric acid. In this research, we employed cocrystallization to decrease caffeine's solubility and dissolution rate while preserving suitable permeability.

The selection of various coformers aimed to create a limited range of molecules with increasing complexity and predictable lipophilicity, facilitating the modulation of caffeine properties via co-crystallization. Since permeability involves traversing a bilayer membrane, the coformer's lipophilicity plays a crucial role in transporting caffeine between aqueous environments through a lipid membrane. It's important to note that the caffeine-coformer adduct formed in the solid state must somehow remain stable in a liquid biological environment, enabling the coformer to influence and modify caffeine's permeability profile. Indeed, the weak interaction between caffeine and the various coformers could lead to dissociation and solvation of the components upon cocrystal dissolution, potentially nullifying the coformer's effect. To assess the stability of the caffeine-coformer in an aqueous environment, extensive density functional theory (DFT) calculations were conducted on potential solution adducts, testing their resistance to dissociation. In all studied systems, the results confirmed the presence of at least one stable entity (caffeine-coformer) in solution, supporting the idea that even weak interactions can alter caffeine's physico-chemical characteristics.

Among the seven cocrystals examined in this study, the most promising candidate is caffeine-xinafoic acid polymorph 1. This combination effectively reduced caffeine's solubility and dissolution rate while concurrently enhancing its permeability. This strategy provides superior control over caffeine's in-vitro release while ensuring the drug's permeability, a crucial factor for achieving beneficial effects.

3.2. Materials and Method

3.2.1. Materials

Caffeine, oxalic acid, malonic acid, xinafoic acid, naringin, morin hydrate, PBS tablets, acetonitrile (ACN), ethyl acetate (EtOAc), tetrahydrofuran (THF), water, and methyl ethyl ketone (MEK) were all sourced from MERCK-Sigma Aldrich (Taufkirchen, Germany, EU) and used without further purification. The solvents were commercially available and utilized without additional purification. For permeability studies, the Permeapad barrier was procured from innoME GmbH (Espelkamp, Germany).

3.2.2. Cocrystal Preparations

3.2.2.1. Caffeine - Oxalic Acid 2:1

The conventional slurry crystallization method was employed to obtain the white solid powder. Caffeine (100 mg, 515 mmol) was suspended in 4 mL of ACN at room temperature (RT) in a 10 mL closed vial. Oxalic acid (23 mg, 258 mmol) was treated similarly. Subsequently, the oxalic acid solution was combined with the caffeine suspension under constant stirring. A solid precipitate formed immediately, and the mixture was left in slurry overnight. After 24 hours, the remaining solid was vacuum-filtered to yield the desired product, which underwent characterization using XRPD, DSC, TGA, SC-XRD, and ^{1}H NMR.

3.2.2.2. Caffeine - Malonic Acid 2:1

A white solid powder co-crystal was obtained through the classic slurry crystallization method. A solution of malonic acid (30 mg, 258 mmol) in 4 mL of ACN was added to a solution of caffeine (100 mg, 515 mmol) in a 10 mL closed vial. The resulting suspension was left in slurry under stirring overnight at RT. After 24 hours, the residual solid was filtered under vacuum to yield the desired product, which was characterized using XRPD, DSC, TGA, SC-XRD, and ^{1}H NMR.

3.2.2.3. Caffeine - Xinafoic Acid Polymorph 1 and 2

A brown solid powder co-crystal was obtained through the classic slurry crystallization method. Initially, caffeine (100 mg, 515 mmol) was combined with an equimolar amount of xinafoic acid (97 mg, 515 mmol) in a 10 mL closed vial. ACN (4 mL) was added, and the resulting suspension was stirred at RT overnight. The isolated solid was obtained via vacuum filtration, yielding a pure co-crystal with a quantitative yield. This co-crystal underwent full characterization using XRPD, DSC, TGA, SC-XRD, and ^{1}H NMR.

3.2.2.4. Caffeine - Naringin Hydrate Form 1

A yellow solid powder co-crystal was obtained through the classic slurry crystallization method. Caffeine (100 mg, 515 mmol) and naringin (299 mg, 515 mmol) were weighed and suspended in 4 mL of ACN at RT in a 10 mL closed vial. After 24 hours of magnetic stirring, the residual solid was filtered under vacuum to yield the desired product. This co-crystal was characterized using XRPD, DSC, TGA, SC-XRD, and ^{1}H NMR.

3.2.2.5. Caffeine - Naringin Hydrate Form 2

A yellow solid powder co-crystal was obtained through the classic slurry crystallization method. Initially, caffeine (100 mg, 515 mmol) was weighed with an equimolar amount of naringin (299 mg, 515 mmol) in a 10 mL closed vial. Ethyl acetate (EtOAc, 4 mL) was added, and the resulting suspension was stirred at RT overnight. After 24 hours, the isolated solid was obtained by vacuum filtration, yielding a pure co-crystal with a quantitative yield. This co-crystal was fully characterized using XRPD, DSC, TGA, SC-XRD, and ^{1}H NMR.

3.2.2.6. Caffeine - Morin

A brown solid powder co-crystal was obtained through the classic slurry crystallization method. The synthesis was performed in a 10 mL closed vial under stirring, adding caffeine (100 mg, 515 mmol) as the starting material and an equimolar amount of morin hydrate (165 mg, 515 mmol) in 4 mL of ACN at RT overnight. The resulting suspension was filtered under vacuum to yield the desired co-crystal. The residual solid was characterized using XRPD, DSC, TGA, SC-XRD, and ^{1}H NMR. Single crystals were grown as EtOAc-H2O solvate-hydrate in a crystallization medium using a CHCl3:EtOAc 1:1 mixture.

3.2.3. Single-Crystal X-ray Diffraction (SC-XRD)

Crystals suitable for Single Crystal X-ray Diffraction (SC-XRD) analysis of caffeine-morin were acquired by employing the method of gradual solvent evaporation. Specifically, a solution of caffeine-morin in CHCl3:EtOAc in a

1:1 ratio was allowed to evaporate slowly. The data collection for single crystal analysis was carried out at a temperature of 220 K using a Bruker (US) D8 Venture diffractometer furnished with a Photon II detector. The diffractometer utilized a microfocus CuKα radiation source (with a wavelength of λ = 1.54184 Å). The intensity data originated from multiple sequences of exposure frames, encompassing the entire reciprocal space. Corrections for absorption were applied through the utilization of the SADABS program.[78] The determination of crystal structures was accomplished through intrinsic phasing, utilizing the SHELXT program.[79] Following this, Fourier analysis and refinement were carried out utilizing full-matrix least-squares methodologies, relying on F^2, and leveraging the SHELXL-2017 software,[80] implemented within the Olex2 software (version 1.3).[81] Anisotropic refinement was applied to non-hydrogen atoms, while hydrogen atoms were positioned based on calculations and then refined using a riding model. The detailed crystallographic data can be located in the Supplementary Materials section. For this paper, the supplementary crystallographic data is deposited under CCDC 2124344. Furthermore, a search in the Cambridge Structural Database (CSD) was conducted using version 5.43, facilitated by the ConQuest tool.[48,114]

3.2.4. X-ray Powder Diffraction (XRPD)

X-ray powder diffraction (XRPD) analyses of the crystalline samples were conducted with a Panalytical Emyrean V 2.0 instrument equipped with a Cu radiation source. The measurements were performed in reflection mode with 2Theta scans ranging from 1.5 to 45°, utilizing a step size of 0.02°, soller slit of 0.02 rad, divergence slit of 1/8°, and antiscatter slit of 1/4°.

3.2.5. Thermal Methods

See Chapter 2.2.5 and 2.2.6.

3.2.6. ^{1}H-NMR

All the NMR experiments were acquired at the ^{1}H proton resonance frequency of 600 MHz, at a temperature of 298 K, using a Bruker AVANCE III HD 600 instrument equipped with a triple resonance TCI INVERSE H-C/N-D-0.5-Z ATMA 5 mm cryoprobe.

3.2.7. Solubility Studies

The initial phase of the study involved assessing the apparent solubility of co-crystals within a pH 7.4 PBS buffer. The solubility assessment encompassed the creation of a saturated solution (50 mg/mL) for each co-crystal, including the original active pharmaceutical ingredient (API), caffeine. These co-crystal suspensions were placed in a slurry under stirring at room temperature. After 24 hours, a 200 μL sample was extracted, subjected to filtration through RC Membrane Syringe Filters (0.22 μm), and then diluted at a 1:50 ratio using ACN:H2O (60:40). Each compound underwent triplicate testing, with subsequent injection into an LC/UV/MS system for caffeine concentration monitoring and apparent solubility determination. Ultra-high-performance liquid chromatography with ultraviolet detection (UHPLC-UV) was the technique employed for quantifying the dissolved drug, with UV absorption occurring in the 200–290 nm range, and a maximum absorbance at 273 nm. UHPLC-UV analysis was conducted using a Waters Acquity UPLC system, coupled with a diode array detector, and equipped with a reversed-phase Kinetex® EVO C8 LC column (100 × 2.1 mm; particle size 1.7 μm; pore size 100 Å, Phenomenex®). The mobile phase consisted of an ammonium formate buffer (pH 3) and 0.1%

formic acid in acetonitrile (ACN), with a flow rate of 0.5 mL/min and a column oven temperature of 50 °C. Each injection volume was 2 µL.

3.2.8. Dissolution Rate Studies

Dissolution studies for caffeine cocrystals were conducted using a pH 7.4 PBS buffer at room temperature. Suspensions at a concentration of 1 mg/mL were prepared for each cocrystal, corresponding to various time points (0, 5 min, 10 min, 20 min, 30 min, 40 min, 60 min, 120 min). From each sample, 200 µL were collected at the designated time, followed by filtration. A 20 µL portion of the filtered solution was then diluted (1:10) using ACN:H2O (60:40) and introduced into the LC/UV/MS system. Similar to the solubility assessment, triplicate testing was performed for each compound, allowing monitoring of caffeine concentration over time to create dissolution rate curves.

3.2.9. Permeability Studies

Permeability was assessed using the Permeapad® tool, a 96-well plate with donor and acceptor compartments separated by a phosphatidylcholine artificial membrane.[17] For each cocrystal, a lag time was implemented (in line with the dissolution rate assay) prior to filling the donor compartment (200 µL) with the cocrystal solution (1 mg/mL). The acceptor compartment was filled with pure PBS (400 µL). Experiments were carried out at room temperature, with the plate covered throughout to preserve membrane integrity. At specified time intervals (0, 0.25, 0.5, 1, 2, 4, 6, 8 hours), 10 µL of sample was withdrawn, diluted (1:10) using ACN:H2O (60:40), and then injected into the LC/UV/MS system. UHPLC-UV analysis was once again employed for quantifying the dissolved drug, utilizing the same equipment setup and chromatographic conditions as previously described for dissolution and solubility studies. Apparent Permeability (Papp) is calculated as reported by Tzanova et al.[115]

3.2.10. Computational Methodology

Density Functional Theory (DFT) calculations were executed using the Gaussian 16 program suite.[116] Molecular geometries were optimized for cocrystals in the ground state without symmetry constraints, beginning with the X-ray geometries of the cocrystals (excluding CA-NA due to lack of a single crystal X-ray structure). Geometries for different caffeine-caffeine and caffeine-coformer adducts were considered. For CA-OX, a π-stacking adduct not present in the single crystal structure was generated, positioning the oxalic acid molecule above the caffeine plane at a 3.4 Å distance. Geometries of isolated caffeine and coformers were also optimized. The B3LYP-D3 functional[117] was employed along with 6-31+G(d)[118] and def2-TZVP basis sets.[119] Calculations incorporated the polarizable continuum model (PCM)[120] using the dielectric constant of water to account for solvation effects. Frequency calculations were performed to verify stationary points as minima on the potential energy surface. Thermochemical values were calculated at 298.15 K and 1.0 atm.

3.3. Results

3.3.1. Characterization of Cocrystals in Solid State

Prior to conducting dissolution and permeability experiments, comprehensive characterization of the cocrystals CA-OX, CA-MA, CA-XA P1, CA-XA P2 was accomplished through X-ray powder diffraction (XRPD), differential scanning calorimetry (DSC), thermogravimetric analysis (TGA), and proton nuclear magnetic resonance spectroscopy (^{1}H-NMR). The obtained data demonstrated a close alignment with existing literature findings (Chapter 3.5 - FIGUREs S1-S11).[107–109] All cocrystals exhibited anhydrous forms, displaying exceptional crystallinity and distinctive sharp melting points.

In the case of the caffeine-naringin cocrystal, it manifested two distinct hydrate forms, as evidenced by XRPD analysis (FIGURE 3.2). Naringin, owing to its intricate molecular structure and consequential conformational flexibility stemming from numerous rotable bonds, was inclined to generate diverse structures.[121]

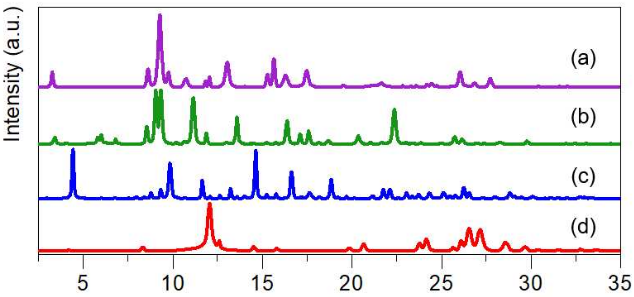

FIGURE 3. 2 *Overlay of experimental X-ray diffraction patterns for (a) CA-NA H2, (b) CA-NA H1, (c) Naringin, and (d) Caffeine.*

Hydrate form 1 was synthesized in acetonitrile (ACN) and exhibited a notably crystalline X-ray diffraction pattern (FIGURE 3.2b). DSC and TGA thermograms (Chapter 3.5 - FIGURE S12) showcased characteristics indicative of a potential hydrate form. Furthermore, ^{1}H-NMR analysis of the dissolving CA-NA-H1 substantiated a 1:1 stoichiometry between caffeine and naringin, with no traces of acetonitrile solvent residues (Chapter 3.5 - FIGURE S13).

Hydrate form 2 of the caffeine-naringin cocrystal was produced in ethyl acetate (EtOAc). It displayed slightly diminished crystallinity (FIGURE 3.2a) and thermograms suggestive of a hydrate form akin to form 1 (Chapter 3.5 - FIGURE S14). Deuterated dimethyl sulfoxide (DMSO) ^{1}H-NMR spectra revealed no EtOAc residuals, confirming a 1:1 caffeine-naringin stoichiometry (Chapter 3.5 - FIGURE S15).

Caffeine-morin cocrystal was synthesized in ACN and featured a fairly crystalline X-ray diffraction pattern (FIGURE 3.3), distinct from caffeine and morin alone. DSC and TGA thermograms (Chapter 3.5 - FIGURE S16) indicated multiple thermal events, indicating a potential dihydrate form. Notably, ^{1}H-NMR spectra in deuterated DMSO demonstrated the absence of ACN residues. Furthermore, a 1:1 stoichiometry between caffeine and morin was determined (Chapter 3.5 - FIGURE S17).

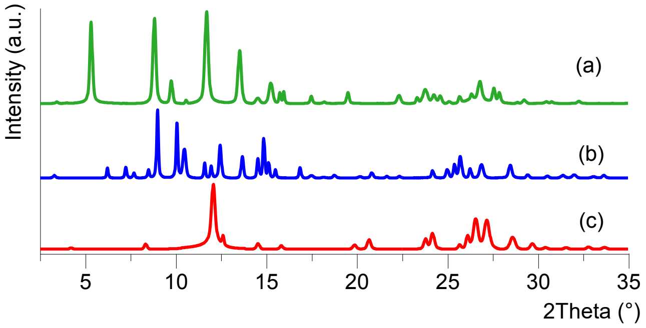

***FIGURE 3. 3** Overlay of experimental X-ray diffraction patterns for (a) CA-MO, (b) Morin hydrate, and (c) Caffeine.*

To gain deeper insights into the structural arrangement of the caffeine-morin and caffeine-naringin systems, attempts were made to cultivate single crystals suitable for X-ray diffraction analysis in various solvents. The goal was to attain a comprehensive understanding of the interactions between caffeine and different coformers. Single crystal X-ray structures of CA-OX, CA-MA, and CA-XA-P1 were previously reported and are summarized in Chapter 3.5 - FIGURE S18. Successful growth of caffeine-morin single crystals in ethyl acetate led to the molecular structure of CA-MO EtOAc H2O being revealed (Chapter 3.5 - FIGURE S19). The crystal structure exhibited the presence of a water molecule and an ethyl acetate molecule as components of crystallization, indicating a distinct solvate form compared to the dihydrate form used in *in vitro* studies. The supramolecular arrangement observed in CA-MO EtOAc H2O unveiled key interactions between caffeine and morin (FIGURE 3.4). The stoichiometry between caffeine and morin was confirmed as 1:1, with two primary types of interactions evident: hydrogen bonding between the nitrogen atom of caffeine (HB acceptor) and a hydroxyl group of morin, as well as π-π stacking involving one of the aromatic rings of morin and the hexa-atomic ring of caffeine.

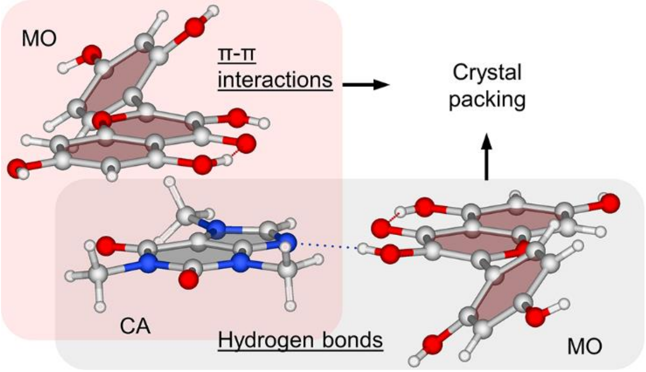

FIGURE 3. 4 *Selected fragment from the X-ray molecular structure of CA-MO EtOAc H2O, highlighting two of the possible types of interaction between Caffeine and Morin in the solid state. Two molecules of Morin are reported, however the ratio of Caffeine and Morin in the structure is 1:1. Solvent molecules were omitted for clarity.*

3.3.2. DFT calculations

To assess the stability of caffeine-coformer adducts within solution, dispersion-corrected density functionals were employed in DFT calculations. These calculations aimed to replicate the weak intermolecular interactions between the two components. The Single Crystal X-ray structures of both cocrystals and caffeine were utilized to identify principal adducts, which fell into two categories: i) hydrogen bonds (HBs); and ii) π-π interactions (the latter being absent in CA-OX cocrystals). For caffeine's isolated structure, only π-π interactions were considered due to their prevalence in other caffeine structures documented in the literature. Hence, these interactions were deemed more favorable compared to the weaker HB formed by caffeine. The interactions between caffeine and the coformers, employed for DFT calculations, are depicted schematically in FIGURE 3.5, while the outcomes of the calculations are recorded in Chapter 3.5 – FIGURE S20-S25 (three for caffeine, two for caffeine-oxalic acid, three for caffeine-maleic acid and caffeine-xinafoic acid, and five for caffeine-morin).

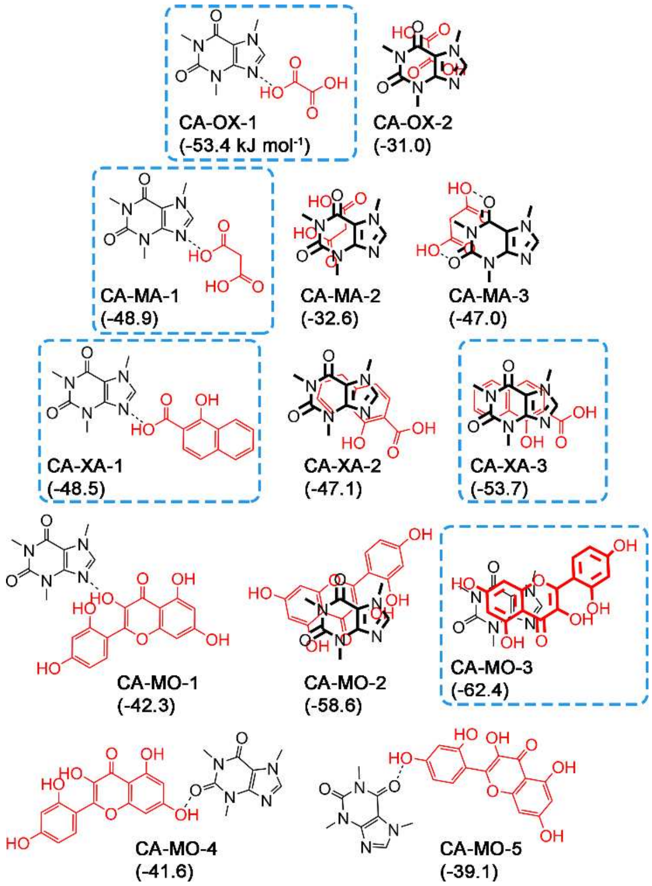

FIGURE 3. 5 *Schematic illustration of interactions present in solid-state structures of Caffeine (black)-coformer (red) adducts. Calculated interaction energies at B3LYP-D3/6-31+G(d), PCM (water) are shown in parentheses for each interaction. Adducts with favorable or nearly favorable calculated ΔG°int are highlighted in cyan.*

Non-covalent interaction energies among the adducts were computed using the equation:

$$E_{int.} = E(adduct) - E(caffeine) - E(coformer)$$

For all considered adducts, interaction energies between caffeine and coformers demonstrated energetic favorability (negative E_{int} values, Chapter 3.5 – TABLE S1). Furthermore, all adducts between caffeine and caffeine exhibited negative interaction energies (ranging from -57.1 to -56.2 kJ mol-1). Within CA-OX and CA-MA, HB interactions displayed more negative values (ranging from -53.4 to -46.3 kJ mol-1) compared to π-stacking interactions (ranging from -32.6 to -29.7 kJ mol-1). In CA-XA, interaction energies showed narrower variance (ranging from -53.8 to -45.5

kJ mol-1), with CA-XA-3's stacking interaction having the highest absolute value (-53.76 kJ mol-1). CA-MO exhibited the most negative E_{int} values, linked to two distinct π-stacking interactions, namely CA-MO-2 (-58.6 kJ mol-1) and CA-MO-3 (-62.4 kJ mol-1), as shown in Chapter 3.5 – FIGURE S24. The HB adducts CA-MO-1, CA-MO-4, and CA-MO-5 presented less favorable E_{int} values (ranging from -42.3 to -39.1 kJ mol-1). Notably, E_{int} values for HB interactions were directly proportional to the strength of the acid employed as a coformer (in the order of Oxalic, Malonic, Xinafoic Acid, and Morin). Conversely, the presence of extensive π-systems and expansive molecular surfaces in Xinafoic Acid and Morin augmented the interaction area with caffeine, rendering π-π stacking interactions more favorable for these systems (Chapter 3.5 – FIGURES S20-25).

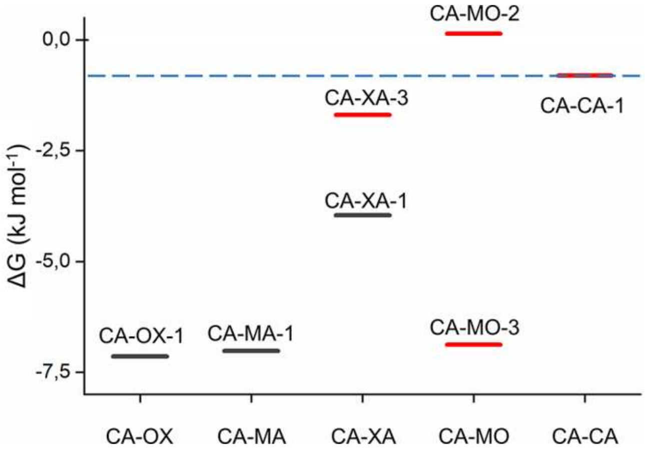

FIGURE 3. 6 *Free energy of formation (ΔG°int) for adducts calculated at B3LYP-D3/6-31+G(d), PCM (water) level of theory. (Black bars denote hydrogen bonds, red bars denote π-π stacking interactions). The value for the only energetically favored caffeine-caffeine adduct (CA-CA-1) is depicted as a dashed line. Only adducts with negative or nearly zero ΔG°int values are shown.*

To understand the fate of various caffeine-coformer systems in water, the free energy for adduct formation at 298 K (ΔG°int) in the presence of water as an implicit solvent was computed. The equation utilized was:

$$\Delta G°_{int.} = \Delta G°(adduct) - \Delta G°(caffeine) - \Delta G°(coformer)$$

Computations indicated that, for every caffeine-coformer pairing, at least one adduct exhibited a negative $\Delta G°_{int}$ (FIGURE 3.6 and Chapter 3.5 – TABLE S1). This implies the favorable formation of solvated adducts in comparison to the solvated parent components, caffeine, and coformer. Moreover, these values were lower than $\Delta G°_{int}$ for the most favorable caffeine-caffeine adduct (CA-CA-1, Chapter 3.5 – FIGURE S20). For Oxalic and Malonic Acid, HB interactions emerged as the only favorable interaction (CA-OX-1 and CA-MA-1 model structures in Chapter 3.5 – FIGURES S21 and S22). Xinafoic Acid yielded two favorable interactions, comprising the HB of CA-XA-1 (where the carboxylic function served as HB donor) and the π-π interaction of CA-XA-3. Morin's weaker HB donor moieties may explain why only the π-π interactions CA-MO-2 and CA-MO-3 were favorable (FIGUREs 3.4 and 3.5). MO and XA possessed extensive molecular surfaces with numerous functional groups, thereby enhancing the potential for favorable interactions in CA-XA and CA-MO. Consequently, XA and MO could modulate caffeine-coformer properties in solution, influencing factors such as lipophilicity and potential membrane permeability (Chapter 3.5 – FIGUREs S20-25).

3.3.3. Solubility studies

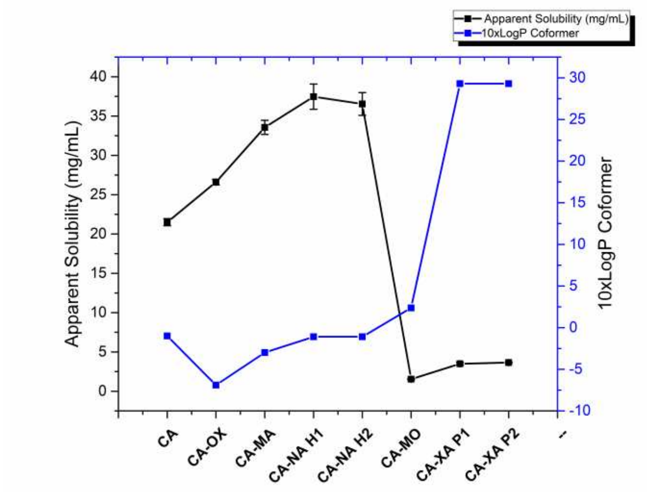

FIGURE 3. 7 *Apparent solubilities (S) of caffeine (CA) and caffeine cocrystals (black) together with 10xLogP values (blu).*

We conducted an evaluation of the apparent solubility (S) for all caffeine-coformer adducts, including various polymorphs involving xinafoic acid and naringin. These solubility values were then compared to the solubility of caffeine itself. FIGURE 3.7 shows the outcomes, illustrating apparent solubility S (mg/mL) as the solubility at a specific pH, without considering potential salt species formation with buffer constituents.[122] Substantial distinctions emerged between caffeine's lone solubility and that of all cocrystals. Comparatively minor differences were observed between polymorphs, such as caffeine-xinafoic acid systems, and hydrates like caffeine-naringin systems. Indeed, distinct forms of the same system yielded similar solubility values. As various polymorphs for a single system share identical chemical entities and stoichiometry, they tend to attain comparable maximum concentrations in solution at chemical equilibrium. Conversely, diverse coformers yielded notably divergent solubilities.

Coformers were categorized based on LogP values from TABLE 3.1. The more hydrophilic group encompassed oxalic acid (-0.69), malonic acid (-0.30), and naringin (-0.11), while the more lipophilic set comprised morin (2.36) and xinafoic acid (2.93). Although our exploration encompassed a limited number of coformers, an observable correlation between hydrophilicity and solubility emerged. Co-crystals with oxalic acid, malonic acid, and naringin exhibited higher solubility. In contrast, cocrystals with xinafoic acid and morin were less soluble. This overarching pattern aligns with expectations, as the most hydrophilic coformers should theoretically enhance solubility within a water-based environment. However, variations deviated from the solubility-hydrophilicity relationship. For instance, oxalic acid demonstrated higher hydrophilicity than naringin, yet CA-OX was marginally less soluble than CA-NA. This data suggests that other factors contribute to the solubility profile and that sole reliance on LogP is insufficient to describe cocrystal solubility. It is evident, nevertheless, that complexation notably influences caffeine's solubility properties in solution.

Compound	**$\Delta G°_{int}^{*}$**	**$\log P_{coformer}$**	**Caffeine $\bar{S}$ (mg/mL)**
caffeine (CA)	-	-	21.50
caffeine - oxalic acid (CA-OX)	-8.48	-0.69	26.60
caffeine - malonic Acid (CA-MA)	-6.95	-0.30	33.56
caffeine - naringin 1 (CA-NA H1)	-	-0.11	37.46
caffeine - naringin 2 (CA-NA H2)			36.53
caffeine – morin (CA-MO)	-4.35	2.36	1.53
caffeine - xinafoic acid 1 (CA-XA P1)	-4.58	2.93	3.65
caffeine - xinafoic acid 1 (CA-XA P2)			3.49

***TABLE 3. 1** Comparison between the apparent solubilities of the cocrystals, the lipophilicity of the coformer alone and the computed free energy of formation in water.*

* kJ mol^{-1}, most stable adduct

3.3.4. Dissolution Studies

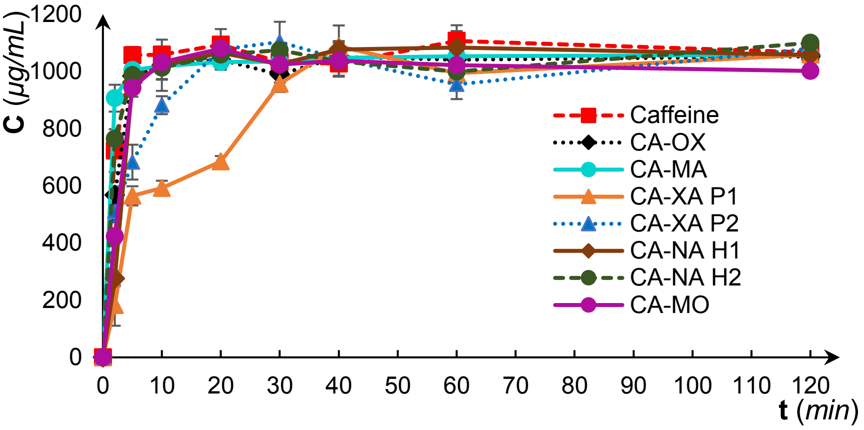

FIGURE 3. 8 *Dissolution profiles of caffeine and the caffeine cocrystals in the 0-120 min range.*

In dissolution measurements, the concentration of caffeine is tracked at various time intervals for each system. This approach assesses the rate of drug concentration increase in a biomimetic PBS solution (pH 7.4) over time, providing insight into the system's evolution in terms of caffeine concentration within the unsaturation regime. In contrast, solubility measures the equilibrium amount of caffeine after a prolonged duration and within the saturation regime. The dissolution experiment spans 8 hours, yet FIGURE 3.8 illustrates data for the initial 120 minutes. Beyond this point, negligible alterations in caffeine concentration were observed, as each system reaches its maximum concentration (1 mg/mL). Caffeine in isolation and most cocrystals exhibit rapid dissolution behavior. Caffeine, CA-OX, CA-MA, CA-NA H1, CA-NA H2, and CA-MO achieve a plateau of 1 mg/mL within 5 minutes. Conversely, caffeine-xinafoic acid cocrystals (both polymorphs) display a distinct dissolution rate profile, reaching peak dissolution after 20 minutes (polymorph 2) and 40 minutes (polymorph 1). It's intriguing to note that although these systems share identical molecular entities and stoichiometry, the dissolution rates between the two polymorphs slightly diverge. This variance could potentially reflect differing structural arrangements inherent to the solid state of the two polymorphs.

3.3.5. Permeability Studies

To gauge the potential impact of cocrystallization on caffeine's membrane diffusion, permeability studies were conducted. These investigations aimed to assess whether the coformer molecules could influence the movement of caffeine across membranes. This consideration gains significance when aiming to achieve controlled drug release, where maintaining permeability despite reduced solubility and dissolution rates is crucial. To ensure independence from solubility or dissolution rate, samples were entirely dissolved before being introduced to the donor compartment, rendering permeability unaffected by these factors.

Fascinatingly, each system exhibited distinct apparent permeability (P_{app}) in the testing medium, signifying that coformer molecules can indeed modulate membrane crossing. Delving deeper, the P_{app} data revealed that caffeine-xinafoic acid cocrystals (both polymorphs) demonstrated higher permeability than caffeine alone, CA-OX, and CA-MA (FIGURE 3.9). Conversely, CA-NA systems showcased the highest permeability. Hence, the adduct formed between caffeine and the coformer in solution notably influences caffeine's permeability.

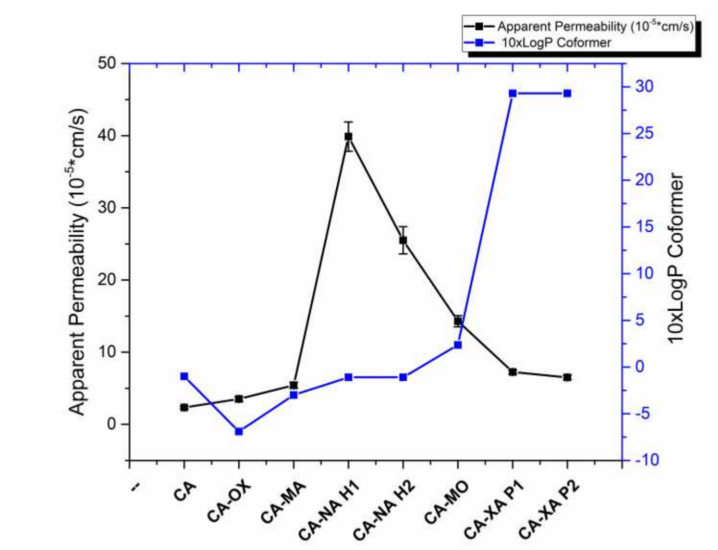

FIGURE 3. 9 *Apparent permeability (Papp) of caffeine and caffeine cocrystals. All of the cocrystals show an increased permeability compared with caffeine alone. 10x LogP of the coformer alone is reported.*

For the CA-XA systems, the notably high LogP of xinafoic acid within the series facilitated its diffusion through the membrane, compared to caffeine alone. Simultaneously, xinafoic acid's high LogP within CA-XA also contributed to reduced solubility and dissolution rates. This interplay could potentially sustain steady blood concentration levels, minimizing abrupt changes in caffeine's effects such as alertness.

Despite naringin's LogP not matching that of xinafoic acid, CA-NA emerged as the most permeable cocrystals. Remarkably, CA-NA H1 displayed a 20-fold higher permeability than caffeine alone, suggesting factors beyond lipophilicity play a role in modulating membrane crossing. One factor we considered was the possible impact on the integrity of the diffusive membrane (Permeapad®). Naringin shares structural similarities with saponins, organic chemicals derived from plants known to disrupt lipidic membranes.[123] To address this, we performed an additional permeability assay using a physical mixture of caffeine and naringin under the same conditions as the CA-NA system (entry 1 in TABLE 3.2). Worth noting is naringin's inherently low solubility, preventing the formation of the caffeine-naringin complex that could influence caffeine's properties in solution, even if starting from separate solid-state forms. Additionally, we carried out permeability tests with caffeine alone, followed by well washing with PBS, and then initiated a new CA-NA H1 co-crystal experiment. After further well washing, we assessed the permeability of the same caffeine solutions used in the first experiment (entry 2 TABLE 3.2). These controlled experiments with fixed variables confirmed that the elevated P_{app} value for CA-NA is a result of adduct formation and effectively ruled out potential membrane damage.

Experiment	**Compound**	**P_{app}**	**SD%**
1	caffeine + naringin physical mixture	1.49	2.1
2	caffeine	2.33	4.5
	caffeine - naringin 1 (CA-NA H1)	34.32	6.3
	caffeine	1.76	6.8

TABLE 3. 2 *Apparent permeability (P_{app}) of the physical mixture of caffeine and naringin (experiment 1) and subsequential permeability measurements of caffeine and caffeine-naringin hydrate form 1 cocrystal in the same well (experiment 2).*

3.4. Conclusion

This study delved into the manipulation of the *in vitro* pharmacokinetic attributes of the active pharmaceutical ingredient, caffeine, through the strategic approach of cocrystallization. Caffeine, with its basic nitrogen atom, two carbonyl groups, and flat aromatic structure, offers the potential for various intermolecular interactions with molecules possessing complementary interaction sites. Notably, molecules featuring acidic hydrogen atoms, planar aromatic structures, or a combination of both, are ideal candidates for interacting with caffeine through hydrogen bonds and/or π-π stacking. In this project, we carefully selected a small group of molecules capable of forming well-defined stoichiometric cocrystals with caffeine in the solid state.

Specifically, the cocrystals CA-OX and CA-MA were formed with oxalic and malonic acids, respectively, via hydrogen bonds. On the other hand, the more complex molecular structures of xinafoic acid, naringin, and morin could engender various hydrogen bonds and π-π stackings. The occurrence of these intermolecular interactions was evident from the solid-state structures, leading to alterations in the caffeine concentration in the solution phase. Oxalic and malonic acids, as well as naringin, increased caffeine's solubility in the solution, while xinafoic acid and morin considerably diminished it within the studied timeframe. Notably, in the case of CA-XA, the presence of the coformer XA led to a reduction in caffeine's dissolution rate during the initial 40 minutes, potentially extending caffeine's effects over time.

Subsequent computational analysis revealed the stability of caffeine-coformer interactions in the aqueous environment for all systems. This suggests that these intermolecular entities in solution could influence caffeine's permeability through a bilayer, depending on the coformer's molecular complexity. Intriguingly, all cocrystals (CA-OX, CA-MA, CA-XA, CA-NA, and CA-MO) exhibited increased permeability compared to caffeine alone. Among these, the most promising outcomes emerged with the caffeine-xinafoic acid polymorph 1 cocrystal. This system showcased reduced solubility and dissolution rates, yet a three-fold increase in permeability (assessed after dissolution completion). Consequently, cocrystallization could offer a method for controlled caffeine delivery, circumventing the need for intricate formulation development processes and optimization. This strategy holds potential for mitigating adverse effects and the "caffeine crash," as coupling caffeine with other molecules to curtail dissolution rates while potentially preserving drug permeability might lead to more stable blood concentrations over an extended period. This, in turn, could mitigate the rapid decline in alertness and the tendency toward caffeine overuse.

3.5. Supporting Information

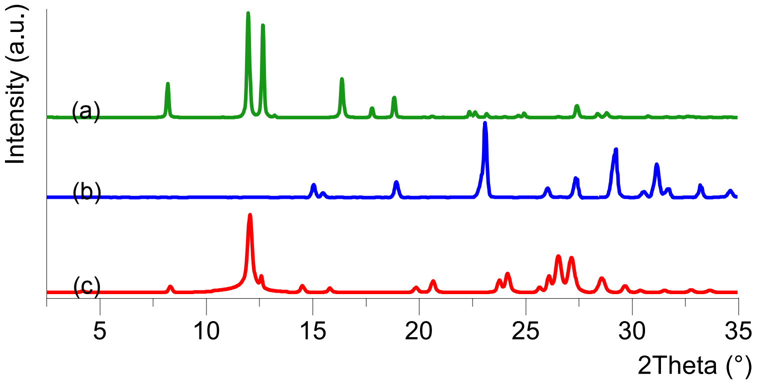

FIGURE S1. *Superimposition of experimental patterns of (a) Caffeine – Oxalic acid (CA-OX), (b) Oxalic acid and (c) Caffeine.*

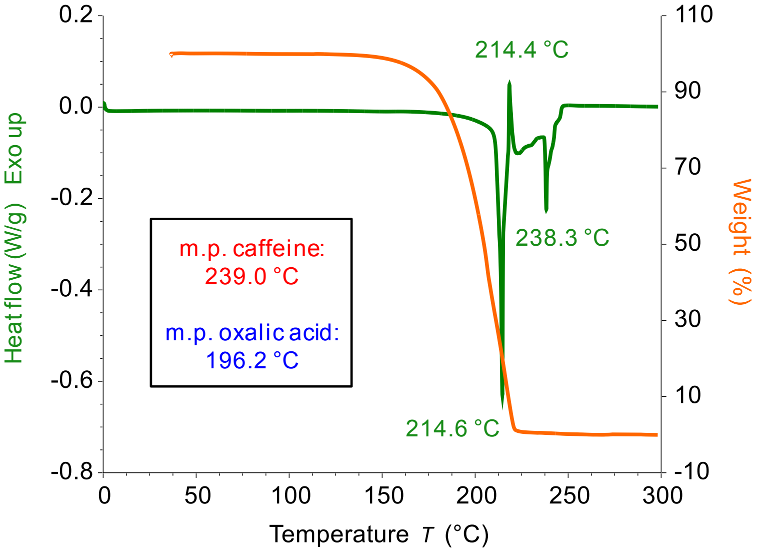

FIGURE S2. *Left, DSC thermogram of CA-OX (10 °C/min) in the 0-300 °C range. Melting points of caffeine and oxalic acid are indicated. Right, TGA profile of CA-OX (10 °C/min) in the 0-300 °C range.*

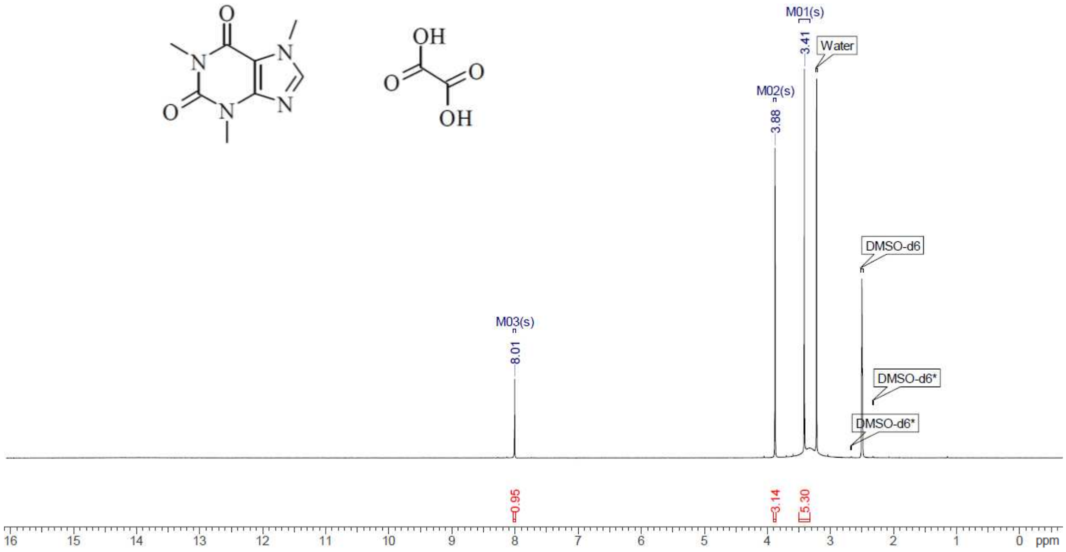

FIGURE S3. *^{1}H NMR spectra of CA-OX dissolved in DMSO-d6.*

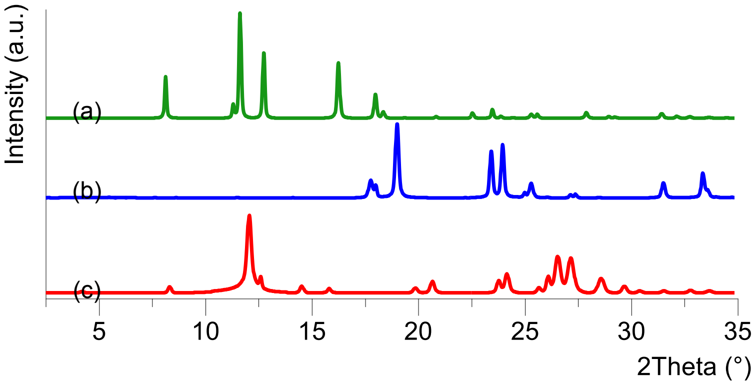

FIGURE S4. *Superimposition of experimental patterns of (a) Caffeine – Malonic acid (CA-MA), (b) Malonic acid and (c) Caffeine.*

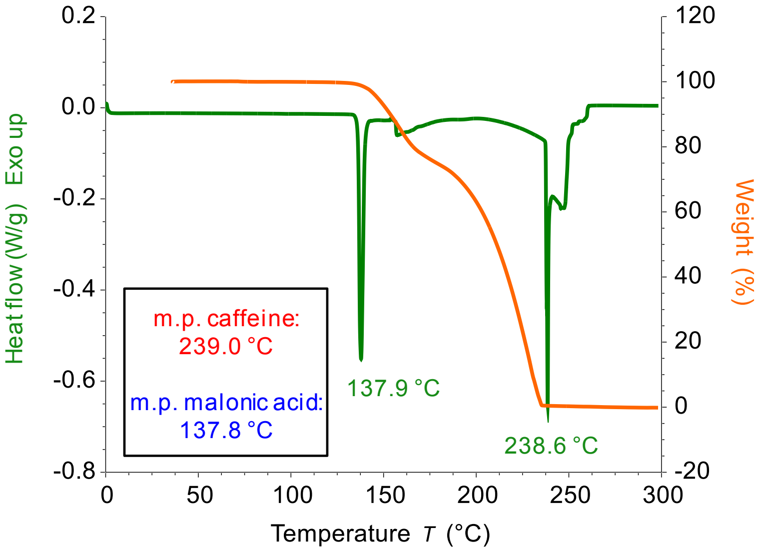

FIGURE S5. *Left, DSC thermogram of CA-MA (10 °C/min) in the 0-300 °C range. Melting points of caffeine and malonic acid are indicated. Right, TGA profile of CA-MA (10 °C/min) in the 0-300 °C range.*

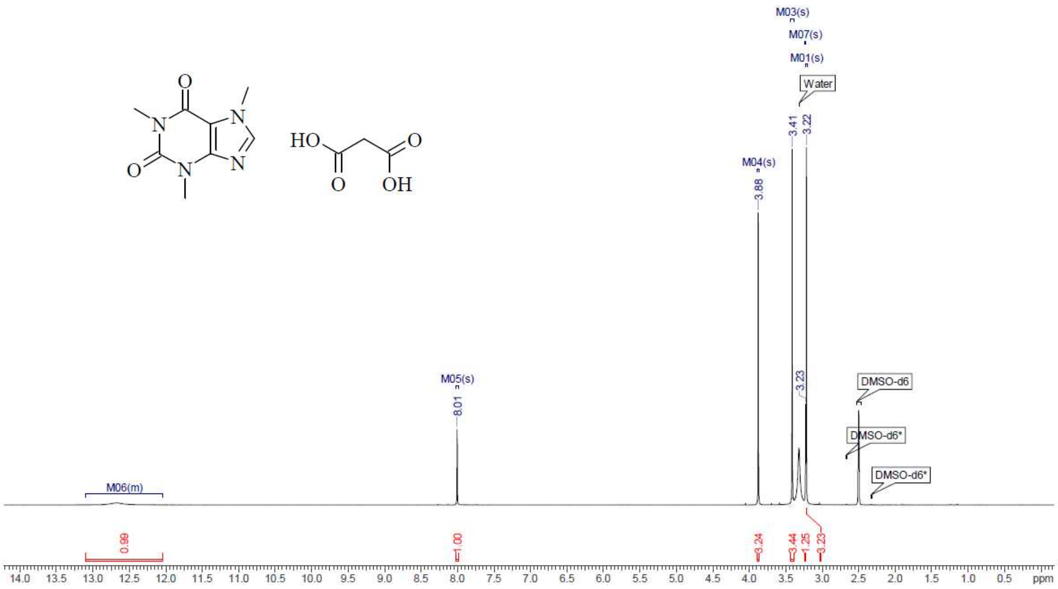

FIGURE S6. *^{1}H NMR spectra of CA-MA dissolved in DMSO-d6.*

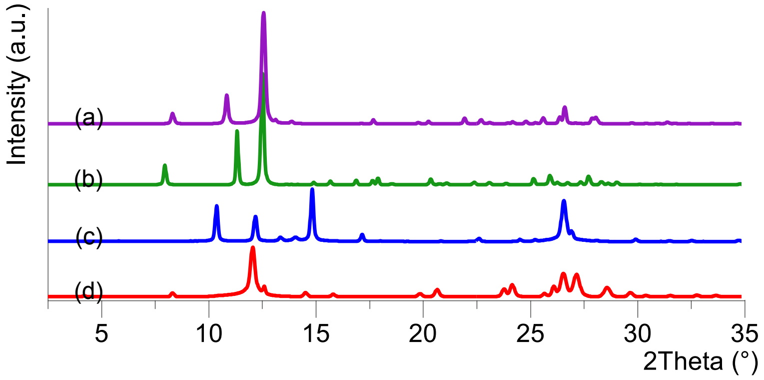

FIGURE S7. *Superimposition of experimental patterns of (a) Caffeine – Xinafoic acid P2 (CA-XA P2), (b) Caffeine – Xinafoic acid P1 (CA-XA P1), (c) Xinafoic acid and (d) Caffeine.*

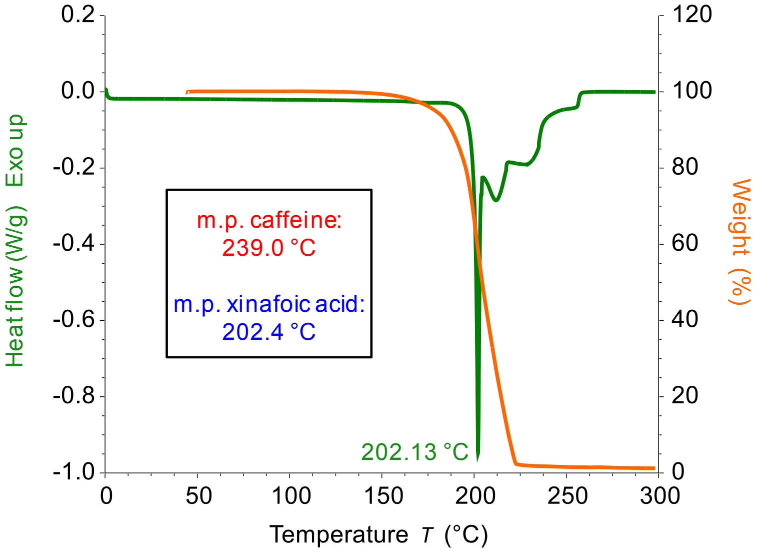

FIGURE S8. *Left, DSC thermogram of CA-XA P1 (10 °C/min) in the 0-300 °C range. Melting points of caffeine and xinafoic acid are indicated. Right, TGA profile of CA-XA P1 (10 °C/min) in the 0-300 °C range.*

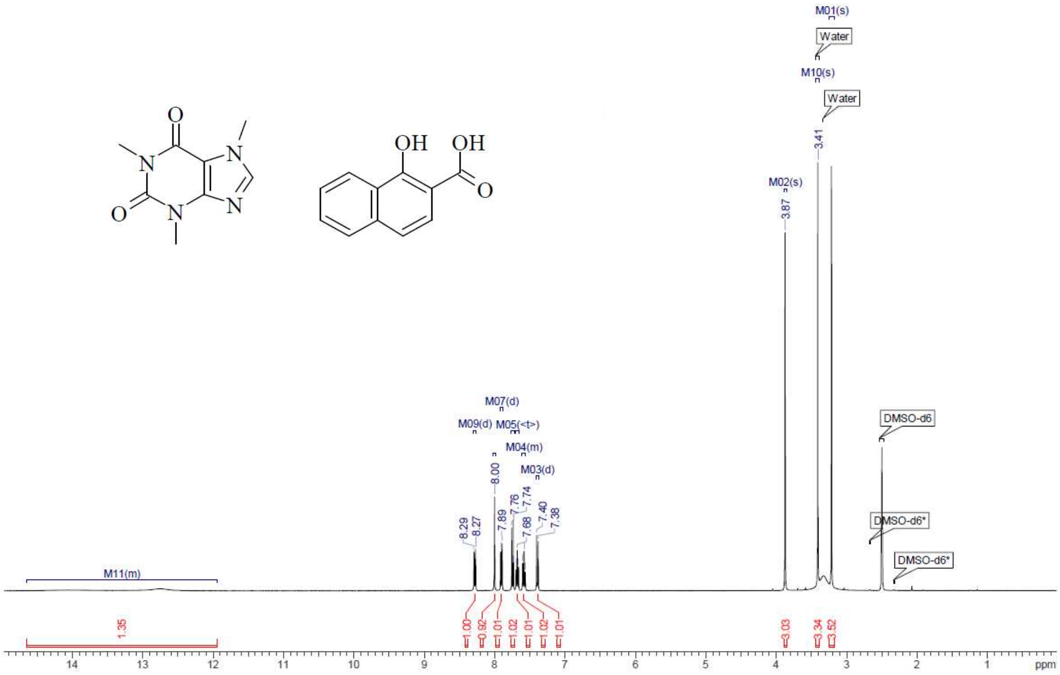

FIGURE S9. *^{1}H NMR spectra of CA-XA P1 dissolved in DMSO-d6.*

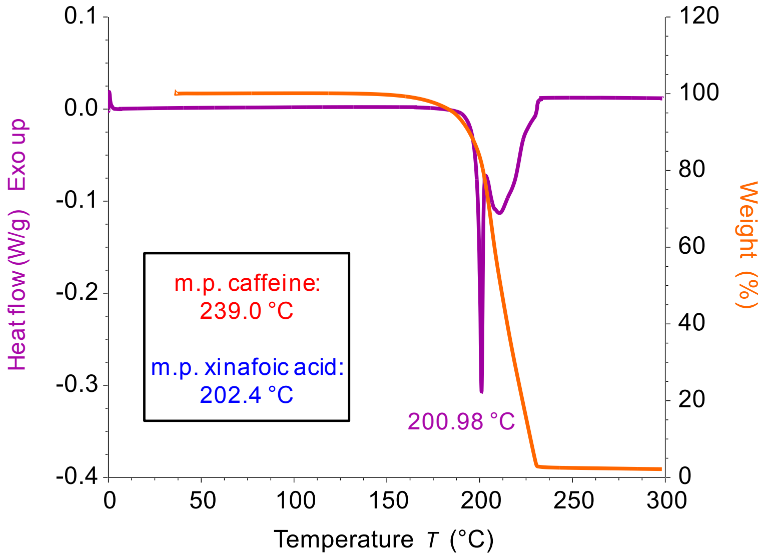

FIGURE S10. *Left, DSC thermogram of CA-XA P2 (10 °C/min) in the 0-300 °C range. Melting points of caffeine and xinafoic acid are indicated. Right, TGA profile of CA-XA P2 (10 °C/min) in the 0-300 °C range.*

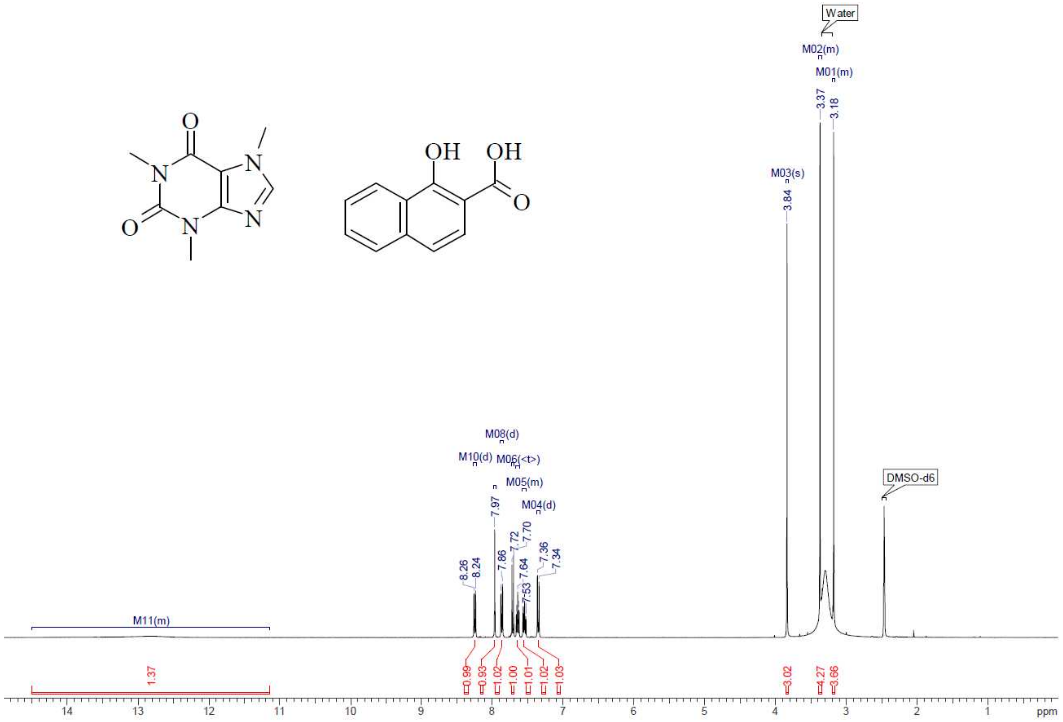

FIGURE S11. *^{1}H NMR spectra of CA-XA P2 dissolved in DMSO-d6.*

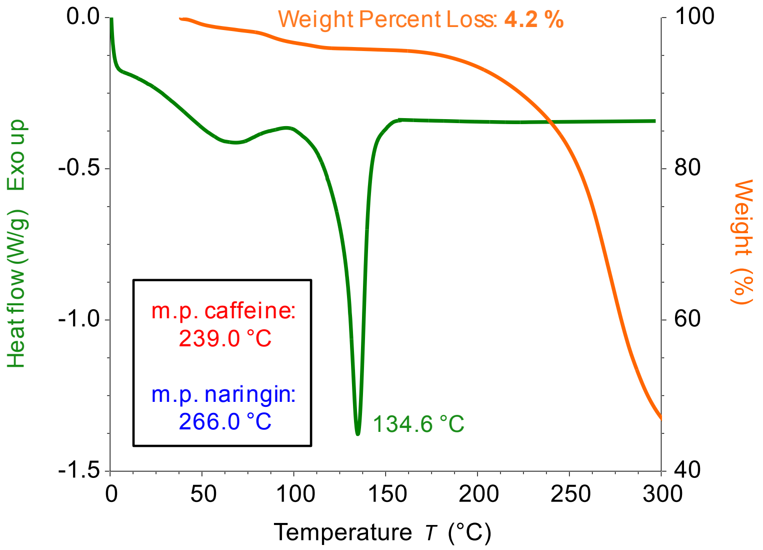

FIGURE S12. *Left, DSC thermogram of CA-NA H1 (10 °C/min) in the 0-300 °C range. Melting points of caffeine and naringin are indicated. Right, TGA profile of CA-NA H1 (10 °C/min) in the 0-300 °C range.*

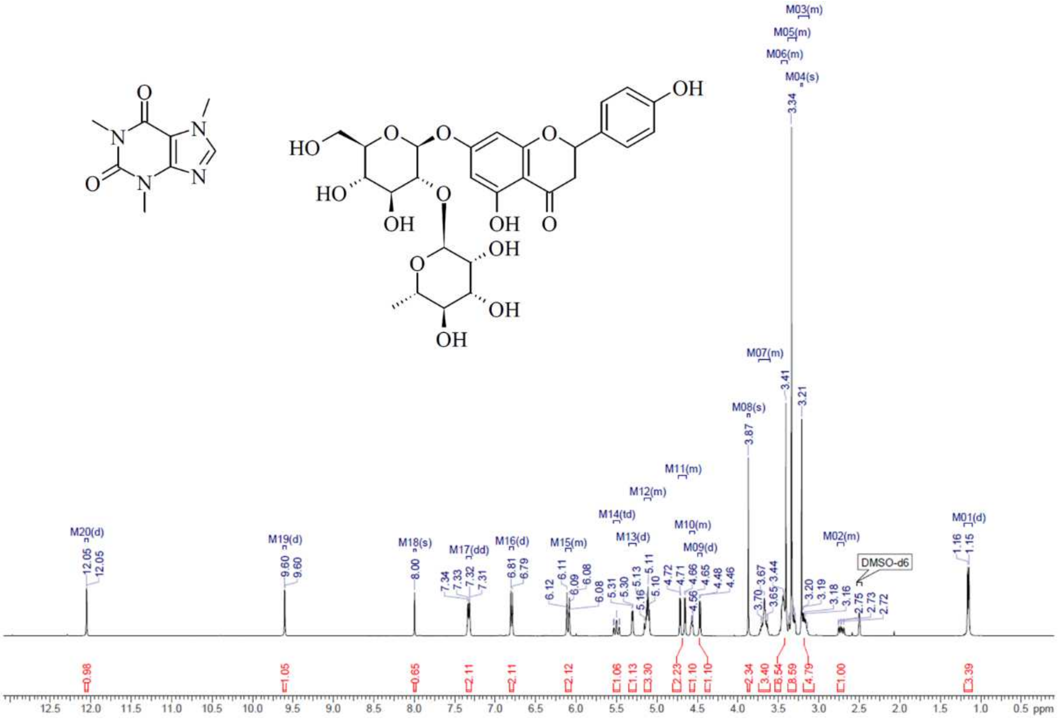

FIGURE S13. *^{1}H NMR spectra of CA-NA H1 dissolved in DMSO-d6.*

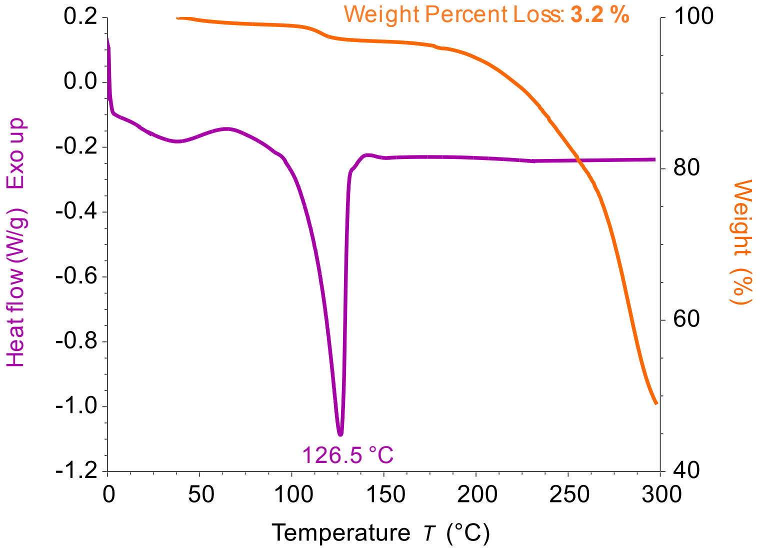

FIGURE S14. *Left, DSC thermogram of CA-NA H2 (10 °C/min) in the 0-300 °C range. Melting points of caffeine and naringin are indicated. Right, TGA profile of CA-NA H2 (10 °C/min) in the 0-300 °C range.*

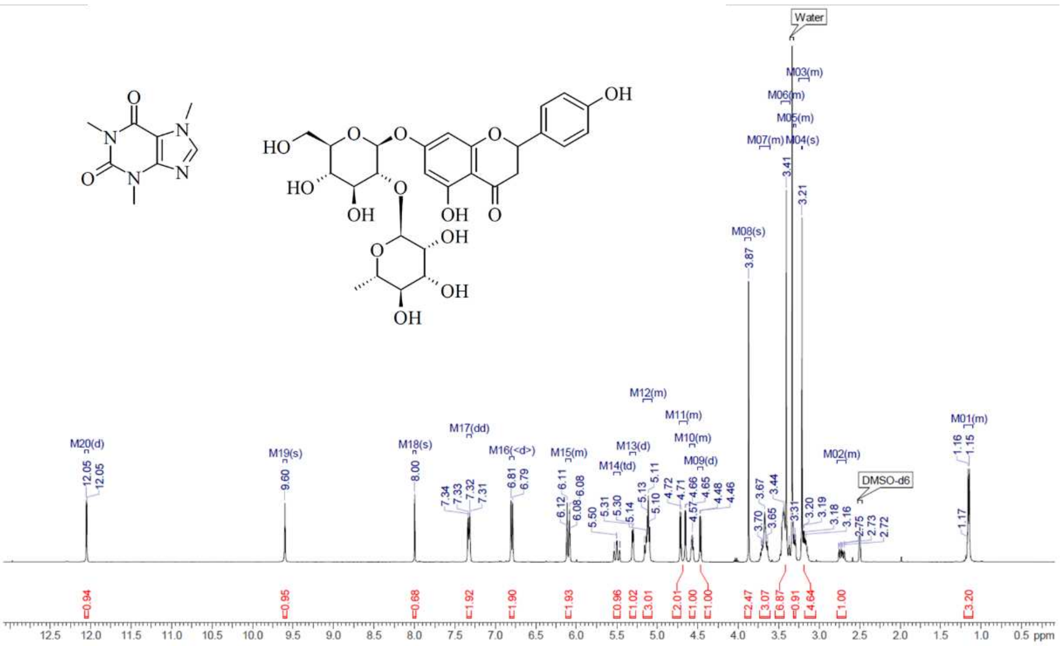

FIGURE S15. *^{1}H NMR spectra of CA-NA H2 dissolved in DMSO-d6.*

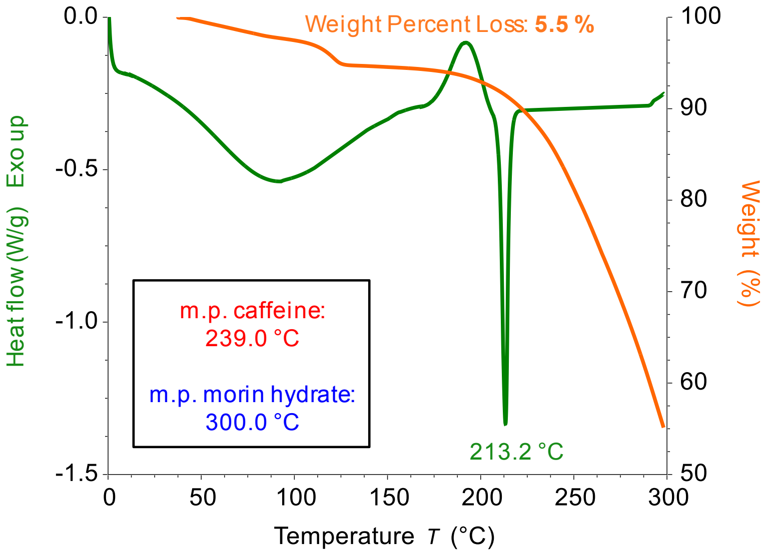

FIGURE S16. *Left, DSC thermogram of CA-MO (10 °C/min) in the 0-300 °C range. Melting points of caffeine and morin hydrate are indicated. Right, TGA profile of CA-MO P2 (10 °C/min) in the 0-300 °C range.*

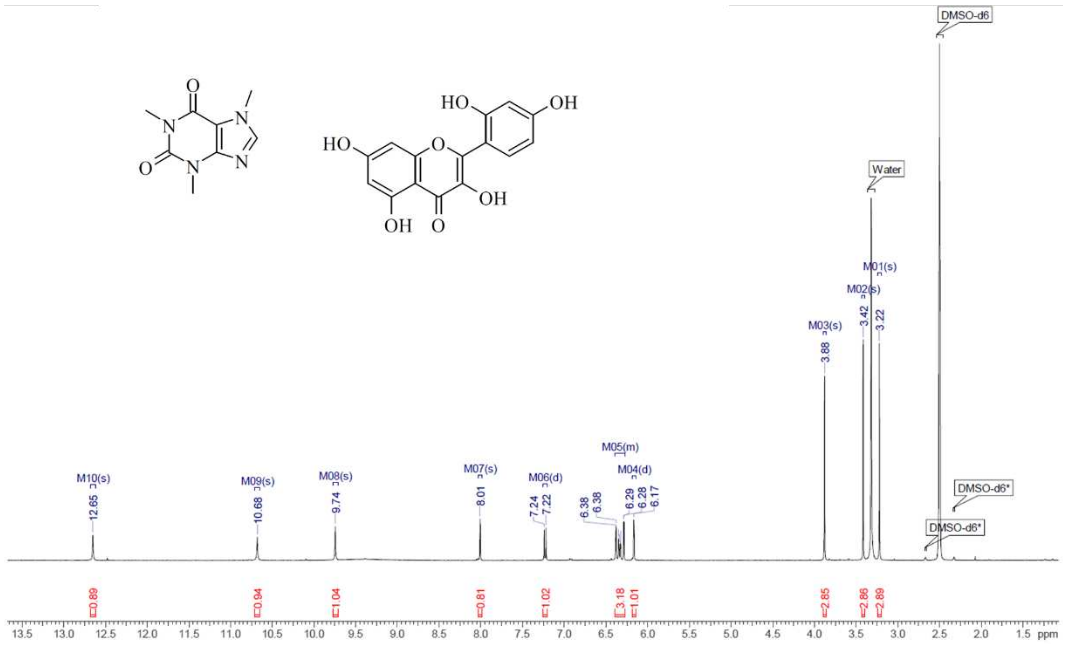

FIGURE S17. *^{1}H NMR spectra of CA-MO dissolved in DMSO-d6.*

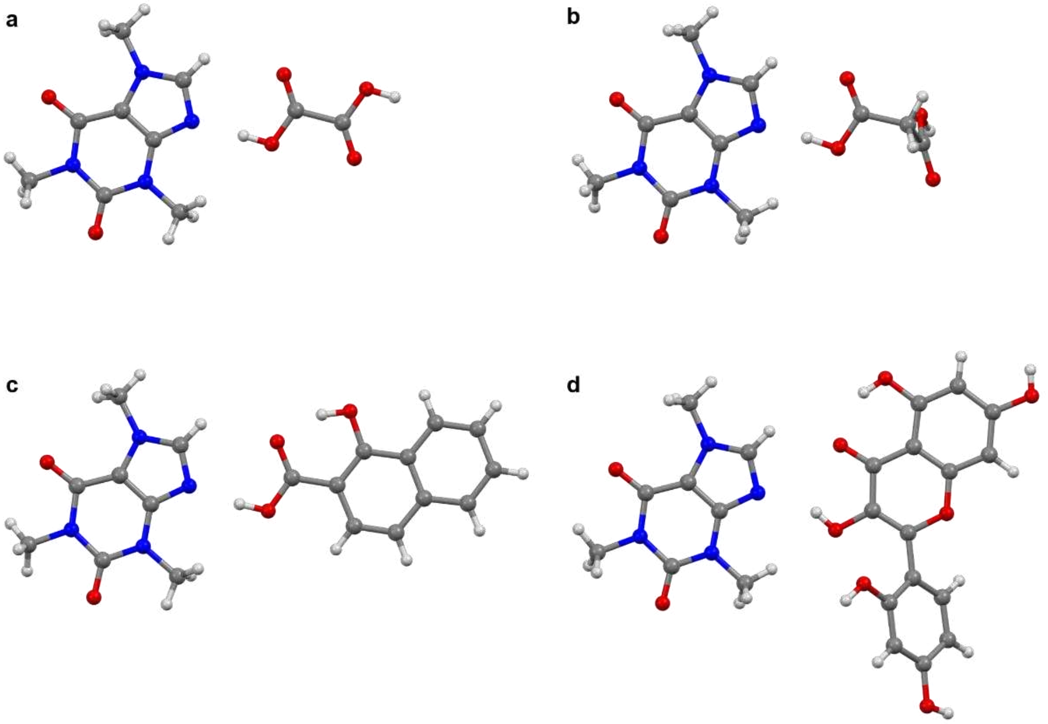

FIGURE S18. *Experimental X-ray structures of a) CA-OX (CCDC 272620), b) CA-MA (CCDC 272621), c) CA-XA-P1 (CCDC 1583505) and d) CA-MO highlighting only the hydrogen bond interaction between caffeine and the coformers with the nitrogen atom of caffeine acting as hydrogen bond acceptor.*

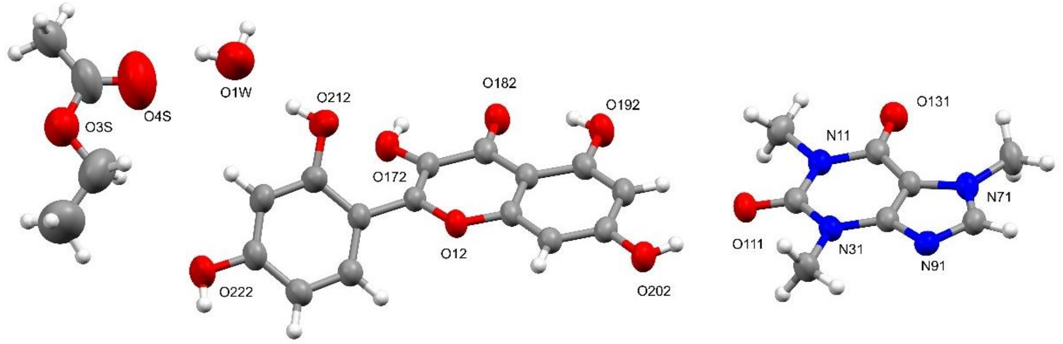

FIGURE S19. *Structural representation of the asymmetric unit of caffeine-morin crystallized from ethyl acetate. Thermal ellipsoid are reported at 30% probability level. C(grey), H(white), N (blue), O (red).*

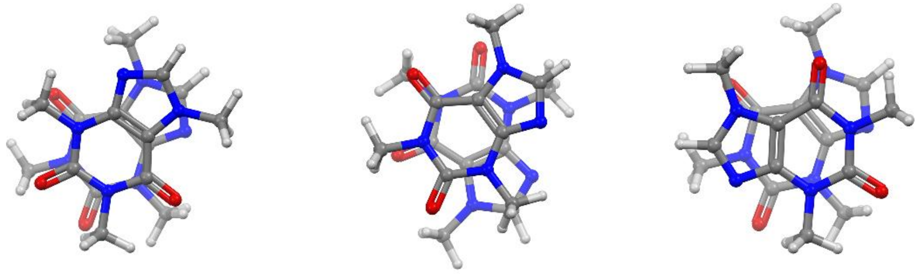

CA-CA-1
(π-π)

CA-CA-2
(π-π)

CA-CA-3
(π-π)

FIGURE S20. *DFT optimized geometries of the caffeine-caffeine (B3LYP-D3/6-31+G(d), PCM (water)). Three types of interactions were considered: CA-CA-1 and CA-CA-2 derived by geometry optimization of the three adducts found in the SC-XRD structure of CA (CCDC 610381).*

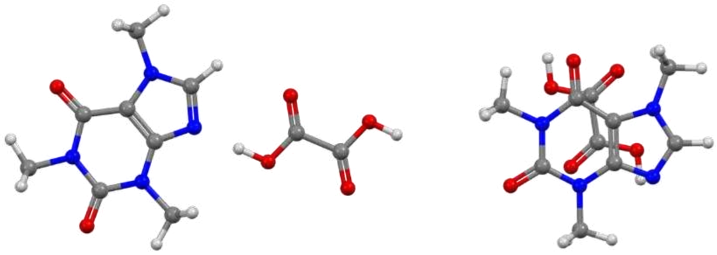

CA-OX-1
(HB)

CA-OX-2
(π-π)

FIGURE S21. *DFT optimized geometries of the caffeine-oxalic acid adducts (B3LYP-D3/6-31+G(d), PCM (water)). Two types of interactions were considered: CA-OX-1 derived by geometry optimization of the adducts found in the SC-XRD structure of CA-OX (CCDC 272620); the starting geometry of CA-OX-2 was instead generated by placing the oxalic acid molecule under the caffeine plane at a distance of 3.4 Å.*

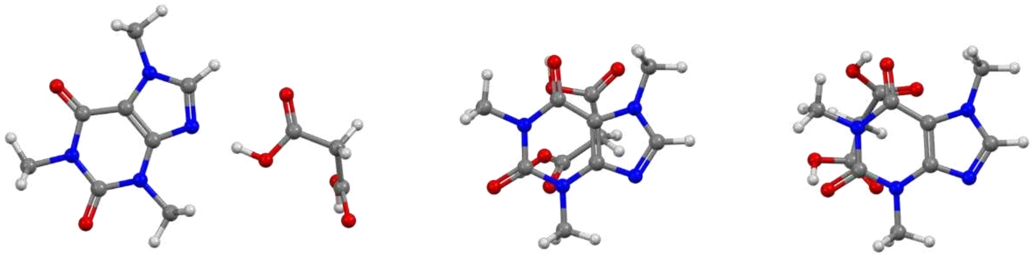

CA-MA-1
(HB)

CA-MA-2
(π-π)

CA-MA-3
(HB)

FIGURE S22. *DFT optimized geometries of the caffeine-malonic acid adducts (B3LYP-D3/6-31+G(d), PCM (water)). Three types of interactions were considered: CA-MA-1 and CA-MA-2 derived by geometry optimization of the adducts found in the SC-XRD structure of CA-MA (CCDC 272621); the starting geometry of CA-MA-3 was instead obtained using a different theory level for the optimization (B3LYP-D3/def2-TZVP, PCM (water)).*

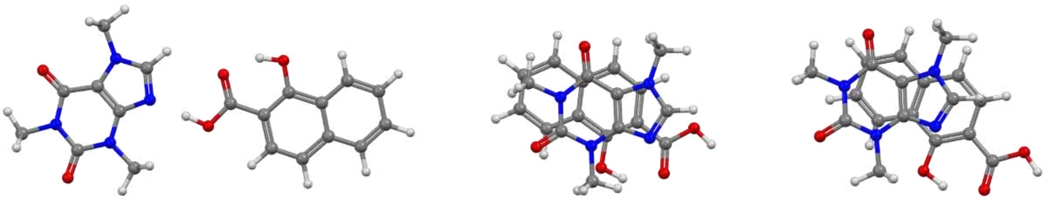

CA-XA-1
(HB)

CA-XA-2
(π-π)

CA-XA-3
(π-π)

FIGURE S23. *DFT optimized geometries of the caffeine-xinafoic acid adducts (B3LYP-D3/6-31+G(d), PCM (water)). CA-XA-1, CA-XA-2 and CA-XA-3 derived by geometry optimization of the adducts found in the SC-XRD structure of CA-XA-P1 (CCDC 1583505) and CA-XA-P2 (CCDC 655956).*

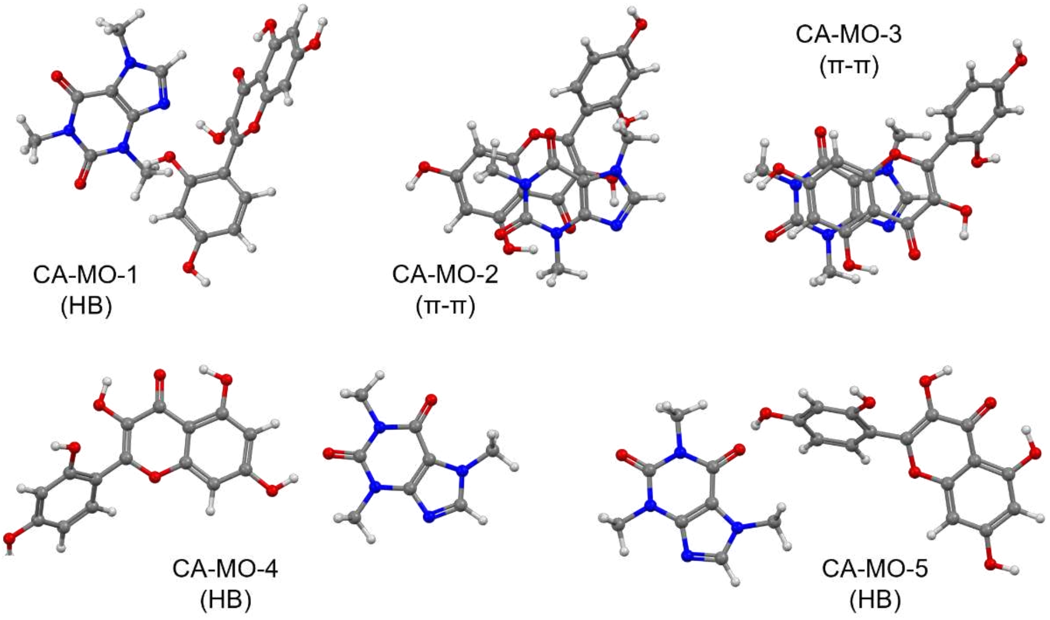

FIGURE S24. *DFT optimized geometries of the caffeine-morin acid adducts (B3LYP-D3/6-31+G(d), PCM (water)). All of the starting geometries were found in the SC-XRD structure of CA-MO.*

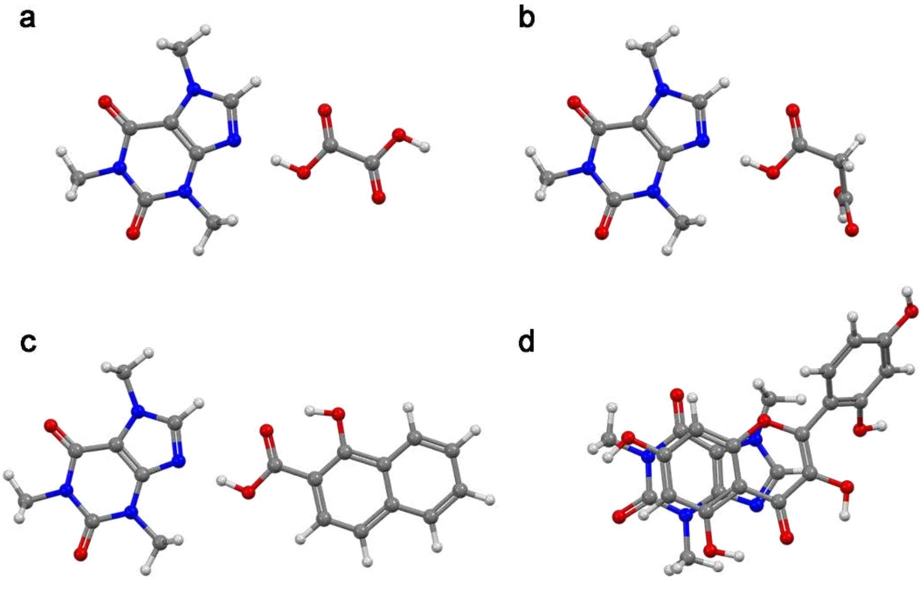

FIGURE S25. *Optimized molecular structures of the caffeine adducts with oxalic acid (CA-OX-1), malonic acid (CA-MA-1), xinafoic acid (CA-XA-1) and morin (CA-MO-3) corresponding to the most stable adducts in the solution phase (B3LYP-D3/6-31+G(d), PCM (water)) according to the calculated* $\Delta G^{\circ}_{int.}$.

TABLE S1. *Calculated interaction energies and free energy of formation of the adducts (B3LYP-D3 using 6-31+G(d) or def2-TZVP as basis set, PCM (water)).*

	$E_{int.}$ (kJ mol^{-1})		**$\Delta G^{\circ}_{int.}$ (kJ mol^{-1})**	
	6-31+G(d)	def2TZVP	6-31+G(d)	def2TZVP
CA-CA-1	-56.70	-56.26	**-0.81**	-2.36
CA-CA-2	-57.12	-56.89	2.34	0.36
CA-CA-3	-57.01	-56.17	3.09	1.17
CA-OX-1	-53.37	-53.01	**-7.14**	-8.48
CA-OX-2	-31.01	-29.67	16.80	18.13
CA-MA-1	-48.92	-48.73	**-7.02**	-6.95
CA-MA-2	-32.57	-	17.09	-
CA-MA-3	-47.00	-46.33	11.24	12.78
CA-XA-1	-48.52	-48.60	**-3.96**	-4.58
CA-XA-2	-47.13	-45.47	3.55	3.87
CA-XA-3	-53.76	-51.95	-1.69	0.23
CA-MO-1	-42.33	-41.68	8.28	8.61
CA-MO-2	-58.61	-57.89	0.14	-4.04
CA-MO-3	-62.42	-59.62	**-6.88**	-4.35
CA-MO-4	-41.55	-42.12	3.79	7.74
CA-MO-5	-39.10	-37.51	5.14	7.91

Chapter 4

4. Enhancing benzocaine psysio-chemical properties with salification, cocrystallization and liposome encapsulation

4.1. Novel salts and cocrystal of benzocaine with increased dissolution rate and permeability open new avenues for enhancing the duration of action.

4.1.1. Introduction

Benzocaine serves as a widely employed local anesthetic compound within the pharmaceutical realm. Its primary function is to induce temporary pain relief and alleviate discomfort due to its numbing properties.[124] Benzocaine achieves this by blocking nerve signal transmission in the targeted area, effectively desensitizing it.[125] However, its short-lived anesthetic effect results from rapid metabolism and elimination from the body, particularly challenging when sustained pain relief is required.[126] Additionally, benzocaine's limited solubility,[127] belonging to class II of the Biopharmaceutical Classification System,[128] further complicates matters. Moreover, absorption rates can vary due to factors such as dermal absorption inter-individual variability,[129] or the presence of other substances, leading to inconsistent clinical outcomes.[130]

To combat these pharmacokinetic challenges, researchers have explored various strategies. These include developing novel formulations, such as nanoencapsulation[131] or utilizing permeation enhancers to enhance drug delivery and absorption.[126] Sustained-release formulations have also been investigated to prolong benzocaine's anesthetic effect, improving patient compliance.[132] However, these formulations face challenges related to selecting appropriate excipients that are compatible with benzocaine to maintain stability and desired release characteristics. Drug-excipient interactions, including physical and chemical incompatibilities, require careful evaluation during formulation development.[96] Polymorphism, the ability of benzocaine to exist in different crystal forms, adds complexity to its pharmacokinetic behavior.[97,98,133]

In this study, crystal engineering principles were employed,[134] focusing on the formation of salts and cocrystals to address benzocaine's pharmacokinetic challenges. Converting benzocaine into a salt or a cocrystal by pairing it with suitable counterions or coformers showed potential for improving *in vivo* absorption. Careful selection of molecular counterparts could enhance dissolution and permeability, ultimately enhancing bioavailability and therapeutic outcomes.[100,135]

While only two structures of benzocaine salts (benzocaine hydrochloride[136] and benzocaine picrate[137]) have been reported in the literature, their pharmacokinetic profiles remain unexplored. In this research, nine new salts and one new cocrystal were synthesized and characterized. To investigate the influence of the counterpart on the active compound's physicochemical properties, two categories of acids were chosen, resulting in two groups of salts. The first category comprised salts derived from sulfonic acids, including benzocaine naphthalenesulfonate (BN), benzocaine camphorsulfonate (BC), benzocaine mesylate (BME), benzocaine benzenesulfonate (BB), benzocaine p-toluenesulfonate (BTS), and benzocaine esylate (BE). The second category included salts containing carboxylic acids like benzocaine oxalate (BO), benzocaine maleate (BMA), and benzocaine tartrate (BT). Additionally, a cocrystal, benzocaine-ligustrazine (BL), was synthesized. Each system underwent comprehensive solid-state characterization, dissolution studies, and permeability studies. Indeed, an amelioration of the *in vitro* properties has been showcased for every system. In particular, all salts as well as the cocrystal exhibit an increased dissolution rate in the first two hours leading to a two-fold increase of dissolved benzocaine after 4 hours. At the same time, all adduct show a significant .enhancement in permeability. The increased dissolution and permeability of the adducts, when compared to benzocaine alone, would potentially lead to a better *in vivo* performance.

4.1.2. Materials and Method

Various chemicals and materials were used in their original form, as obtained from MERCK-Sigma Aldrich in Taufkirchen, Germany, within the European Union. Commercially available solvents were employed without further purification. The Permeapad® barrier, utilized for permeability studies, was procured from innoME GmbH in Espelkamp, Germany.

4.1.2.1. Preparation of salts and cocrystals

Benzocaine oxalate (BO), benzocaine naphtalensulfonate (BN), and benzocaine camphorsulfonate (BC) were synthesized through a classic slurry crystallization method. This involved suspending benzocaine and the respective counterion in a 1:1 molar ratio in 4 mL of ethanol (EtOH) at room temperature (10 mg/mL). Solid precipitates formed overnight via slurry.

Benzocaine maleate (BMA), benzocaine mesylate (BME), and benzocaine tartrate (BT) were obtained through a slow evaporation crystallization method. Benzocaine and the counterion were suspended in a 1:1 molar ratio in 4 mL of EtOH at room temperature (10 mg/mL), and solid precipitates formed overnight through evaporation.

Benzocaine benzenesulfonate (BB), benzocaine p-toluensulfonate (BTS), and benzocaine esylate (BE) were synthesized using the classic slurry crystallization method. Here, benzocaine and the respective counterion were suspended in a 1:1 molar ratio in 4 mL of acetone at room temperature (10 mg/mL). Additionally, benzocaine p-toluensulfonate was recrystallized from acetonitrile (ACN) to enhance crystallinity.

Benzocaine-ligustrazine (BL) cocrystal was synthesized through a slow evaporation crystallization method, where both components were dissolved in a 1:1 molar ratio in 4 mL of acetone at room temperature (10 mg/mL).

All obtained solids underwent comprehensive characterization, including X-ray Powder Diffraction (XRPD), Chapter 4.3 - FIGURE S8; Differential Scanning Calorimetry (DSC), Chapter 4.3 - FIGURE S9-12; Thermogravimetric Analysis (TGA), Chapter 4.3 - FIGURE S9-12; and Nuclear Magnetic Resonance (^{1}H-NMR) analysis, Chapter 4.3 - FIGURE S12-16. Single-Crystal X-ray Diffraction (SC-XRD) structures were determined for BO, BMA, BME, BB, BTS, BL, and BT. Each system exhibited a 1:1 stoichiometry, except for benzocaine oxalate and benzocaine-ligustrazine, which had a 1:0.5 stoichiometry, as confirmed by SC-XRD structures and ^{1}H NMR spectra.

4.1.2.2. Single-Crystal X-Ray Diffracton (SC-XRD)

A summary of data collection and structure refinement for the reported structures is reported in Chapter 4.3 - TABLE S1-3. Single crystal data were collected at 220 K with a Bruker (US) D8 Venture diffractometer equipped with a Photon II detector (Mo Kα: λ = 0.71073 Å; Cu Kα: λ = 1.54184 Å). The intensity data were integrated from several series of exposure frames covering the sphere of reciprocal space. Data reductions were performed with APEX3. Absorption corrections were applied using the program SADABS.[78] The structures were solved by intrinsic phasing with the program SHELXT.[79] Fourier analysis and refinement were performed by the full-matrix least-squares methods based on F^2 using SHELXL-2017[80,138]implemented in Olex2 software (version 1.3).[81] Non-hydrogen atoms were refined with anisotropic thermal parameters for all crystal structures. The hydrogen atoms of the anions of BO, BMA, BT and of the protonated nitrogen atom of benzocaine were located from the difference Fourier map and they were refined with bond distance restraints. The hydrogen atoms of the amino group of benzocaine of BL were found and refined with bond distance restraints. All of the other hydrogen atoms were placed in their calculated positions. Crystals of BMA were non-merohedral twins and the absorption correction was applied with the TWINABS[139] program. Graphical material was prepared with the Mercury 2021[140] program. Cambridge Structural Database (CSD) search was accomplished on version 5.43 using ConQuest tool.[114]

4.1.2.3. X-ray Powder Diffraction (XRPD)

X-ray powder diffraction (XRPD) analyses of the crystalline samples were conducted with a Panalytical Emyrean V 2.0 instrument equipped with a Cu radiation source. The measurements were performed in reflection mode with 2Theta scans ranging from 1.5 to 45°, utilizing a step size of 0.02°, soller slit of 0.02 rad, divergence slit of 1/8°, and antiscatter slit of 1/4°.

4.1.2.4. Thermal Methods

Differential Scanning Calorimetry (DSC) assessments were conducted using a regularly calibrated differential scanning calorimeter Discovery from TA Instruments, which was fitted with a computerized analysis system called TRIOS. For temperature and enthalpy calibration, an Indium standard was employed, while a sapphire disk was utilized for heat capacity calibration. The apparatus was enhanced with a refrigerated cooling system (RCS90) attachment, operated under the protection of a dry nitrogen flow (at a rate of 50 mL/min). Each sample, ranging from 1 to 5 mg, was positioned within a hermetically sealed Tzero Aluminum DSC pan, capped securely. The sample enclosure was stabilized at 0 °C, subsequently heated while exposed to a nitrogen flow (50 mL/min). To ensure uniform thermal treatment, all specimens underwent analogous heating conditions: a linear ascent to 300 °C at a rate of 10 °C/min.

Thermogravimetric Analysis (TGA) was executed employing a TA Instruments Discovery instrument, furnished with the TRIOS V4.3 computer analysis system. Roughly 2 mg of each specimen were inserted into a Platinum pan of 100 µL capacity. The elevation in temperature followed a trajectory of 10 °C/min, terminating at 300 °C.

4.1.2.5. ^{1}H-NMR

All the NMR experiments were acquired at the ^{1}H proton resonance frequency of 600 MHz, at a temperature of 298 K, using a Bruker AVANCE III HD 600 instrument equipped with a triple resonance TCI INVERSE H-C/N-D-0.5-Z ATMA 5 mm cryoprobe.

4.1.2.6. Dissolution Rate Studies

Dissolution studies of benzocaine salts and cocrystal were carried out using PBS buffer (pH 7.4) at room temperature. 7 suspensions at a concentration of 1 mg/mL were prepared for every system. Each suspension corresponds to a different time point (0, 5 min, 15 min, 30 min, 1 h, 2 h, and 4 h). From each sample, 200 µL were taken at the corresponding time point and filtered. 20 µL from each taken solution were then diluted (1:10) with ACN:H2O 60:40 and injected into LC/UV/MS system. Each compound was tested in triplicate, in order to monitor the benzocaine concentration in solution at each time point and plot the dissolution rate curve. Ultra-high-performance liquid chromatography with ultraviolet detection (UHPLC-UV) was used for quantitative analysis of the dissolved drug which absorbs UV-light in the range of 200–290 nm with an absorbance maximum at 273 nm. UHPLC-UV analysis was conducted on a Waters Acquity UPLC system (Milford, MA, USA) that was connected to a diode array detector and equipped with a reversed phase Kinetex® EVO C8 LC column (100 × 2.1 mm; particle size 1.7 µm; pore size 100 Å, Phenomenex®). The mobile phase consisted of 25 mM of ammonium formiate buffer (pH 3) and 0.1% formic acid in acetonitrile, the flow rate was 0.5 mL/min and the column oven was set to 50 °C. The injection volume was 2 µL.

4.1.2.7. Permeability Studies

Permeability was assessed using the Permeapad® tool, a 96-well plate with donor and acceptor compartments separated by a phosphatidylcholine artificial membrane.[17] For each sample, a lag time was implemented (in line with the dissolution rate assay) prior to filling the donor compartment (200 µL) with the cocrystal solution (1 mg/mL). The acceptor compartment was filled with pure PBS (400 µL). Experiments were carried out at room temperature, with the plate covered throughout to preserve membrane integrity. At specified time intervals (0, 0.25, 0.5, 1, 2, 4, 6, 8 hours), 10 µL of sample was withdrawn, diluted (1:10) using ACN:H2O (60:40), and then injected into the LC/UV/MS system. UHPLC-UV analysis was once again employed for quantifying the dissolved drug, utilizing the same equipment setup and chromatographic conditions as previously described for dissolution and solubility studies. Apparent Permeability (Papp) is calculated as reported by Tzanova et al.[115]

4.1.3. Results

4.1.3.1. Analysis of solid-state properties for salts and cocrystal

We determined the single crystal structures of BO, BB, BME, BMA, BT, BTS, and BL, offering insights into the interactions between benzocaine and its protonated form alongside their respective counterparts. To investigate these intermolecular interactions, we employed the CrystalExplorer[141] program to generate 2D fingerprint plots.

The 2D fingerprint plots revealed that benzocaine engaged in various interactions, with hydrogen bonds being the shortest in all cases. However, BMA, BB, and BTS exhibited a notable presence of CH···H interactions in shaping their 3D structures. These structures showcased multiple π-π interactions involving the aromatic ring of benzocaine (Chapter 4.3 - FIGURE S1-3).

More detailed information regarding the single crystal X-ray structures can be found in the subsequent section. They are divided into three categories: salts containing carboxylic acids, salts with derivatives of sulfonic acids, and the cocrystal (FIGURE 4.1).

Each novel system exhibits a 1:1 stoichiometry, except for benzocaine oxalate and benzocaine-ligustrazine, which exhibited a 1:0.5 stoichiometry as indicated by the SC-XRD structures and the ^{1}H-NMR spectra. In the case of benzocaine-ligustrazine (BL), the ligustrazine molecule serves as a hydrogen bond acceptor, interacting with two separate benzocaine molecules through both of its nitrogen sites. In contrast, benzocaine oxalate (BO) stands out among the salts containing dicarboxylic acids because it maintains the acid in a bis-deprotonated state. Among the dicarboxylic acids discussed in this study, oxalic acid is the most acidic (oxalic acid: pKa1 = 1.25, pKa2 = 4.14; maleic acid pKa1 = 1.94, pKa2 = 6.22; tartaric acid: pKa1 = 2.89, pKa2 = 4.40; PubChem®). The high acidity of oxalic acid, combined with the complex network of hydrogen bonds surrounding the symmetrical structure of the oxalate anion, may contribute to its existence in a doubly deprotonated form (Chapter 4.3 - FIGURE S4).

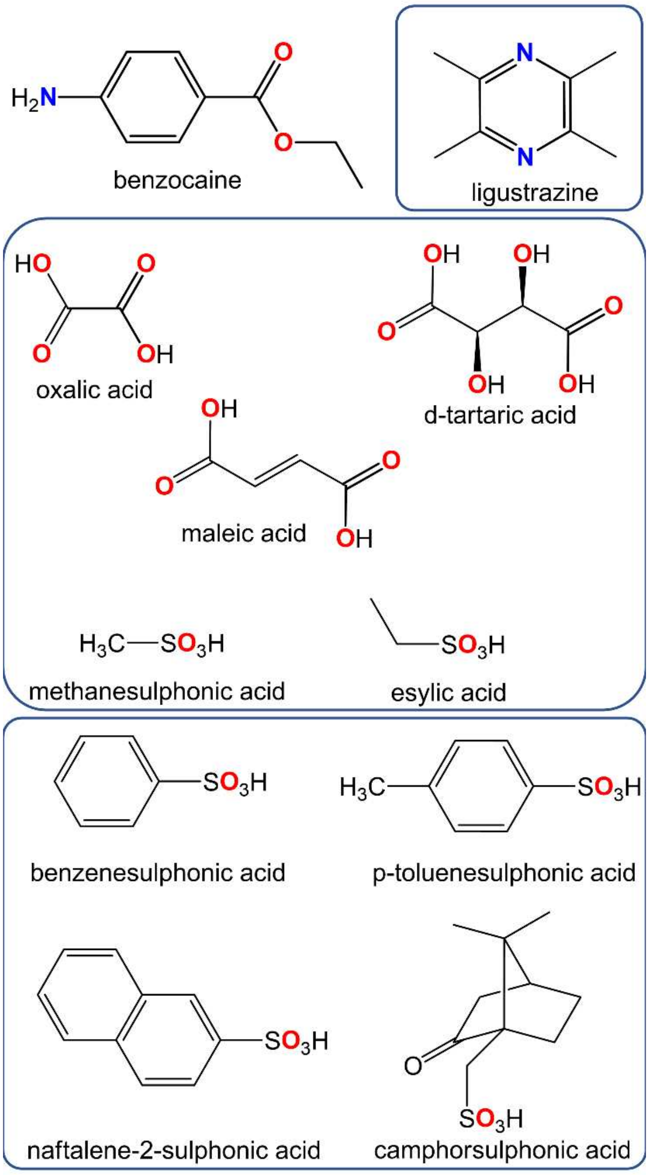

FIGURE 4. 1 *Molecular structures of the benzocaine (API), ligustrazine (coformer), and the various carboxylic and sulphonic acids used as salification agents.*

Benzocaine and carboxylic acids

The BO salt's asymmetric unit consists of a single benzocaine molecule and half of an oxalic acid molecule, which is positioned along a binary crystallographic axis. As depicted in Chapter 4.3 - FIGURE S4, the di-deprotonated oxalic acid forms direct hydrogen bond interactions with six benzocaine molecules. Notably, the closest interaction involves O4 and the protonated benzocaine nitrogen atom at a distance of 2.76 Å. It's worth noting the π-π stacking phenomenon that arises from the three-dimensional arrangement of benzocaine molecules around the anion, with the shortest distance occurring between C6 and C5 (3.51 Å).

Conversely, the BMA and BT salts contain two benzocaine molecules, two counterion molecules, and either one (BMA) or two (BT) water molecules, as illustrated in FIGURE 4.2. Specifically, as shown in Chapter 4.3 - FIGURE S5 (panel a), in BT, the first benzocaine molecule in the asymmetric unit interacts with three deprotonated tartaric acid molecules, which serve as hydrogen bond acceptors. The shortest of these interactions is found between N11 and O13, measuring 2.72 Å. The second benzocaine molecule displays a similar arrangement with several strong and oriented hydrogen bonds, the closest being N12···O33 at 2.73 Å.

Meanwhile, within the BMA structure (Chapter 4.3 - FIGURE S5, panel b), benzocaine molecules are encircled by a network of interactions involving three anions each, along with water molecules. Notably, N11 forms a hydrogen bond with O1W at a distance of 2.94 Å, while N12 interacts with

O1W at a distance of 2.82 Å. TABLE 4.1 provides a summary of the hydrogen bonds observed in the crystal packing.

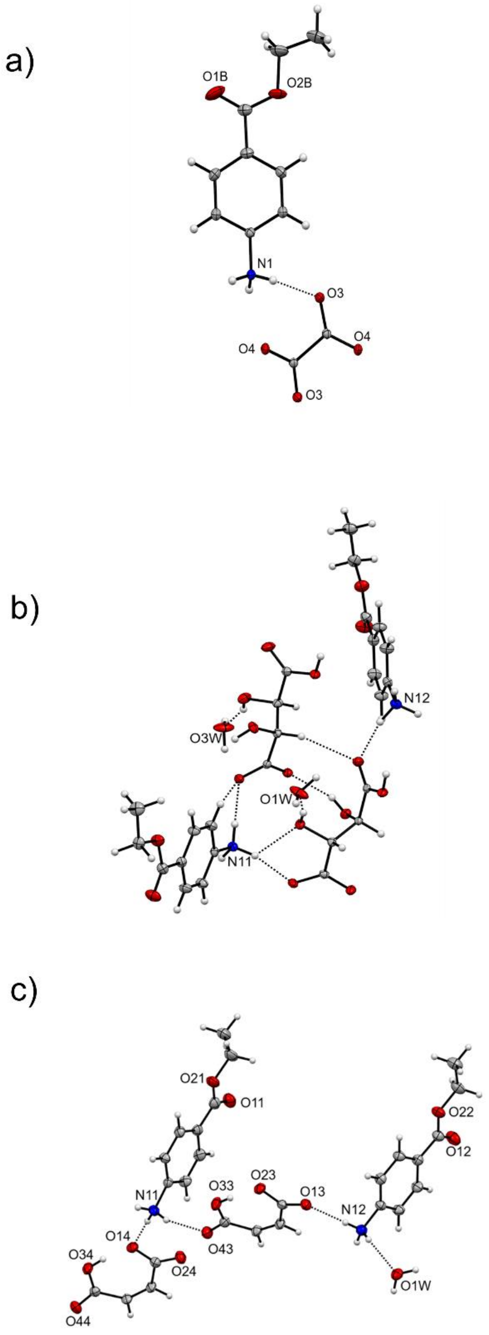

***FIGURE 4. 2** Molecular structure of a) BO, b) BT, c) BMA. Thermal ellipsoids are depicted at the 30% probability level.*

The crystallographic analysis unveils that the structures of benzocaine tartrate (BT), benzocaine maleate (BMA), and benzocaine oxalate (BO) display stratified arrangements, wherein benzocaine molecules adopt alternating head-to-tail orientations. Within these structures, the anions form layers, creating distinct regions occupied by the protonated benzocaine cations and the anions. It's worth noting that in BMA, the benzocaine molecules are closely packed together through π-π stacking interactions (specifically, C41···C42 at a distance of 3.68 Å), while in the case of BO, relatively weak hydrophobic interactions facilitated by the peripheral ester groups drive the interaction between benzocaine molecules (FIGURE 4.3).

Label	HB	HB length (Å)
BO	N11···O4	2.79
	N11···O4	2.76
	N11···O3	2.78
BT	N11···O13	2.72
	N11···O14	2.75
	N11···O54	2.79
	N11···O53	2.92
	N12···O33	2.73
	N12···O34	2.94
	N12···O64	2.78
	N12···O63	2.77

BMA	N11···O14	2.90
	N11···O24	2.91
	N11···O43	2.84
	N11···O1W	2.94
	N12···O13	2.79
	N12···O23	2.89
	N12···O1W	2.82
	N12···O44	3.03

TABLE 4. 1 *HBs between protonated benzocaine and the surrounding anions/water molecules for carboxylate salts with the relative distances (Å).*

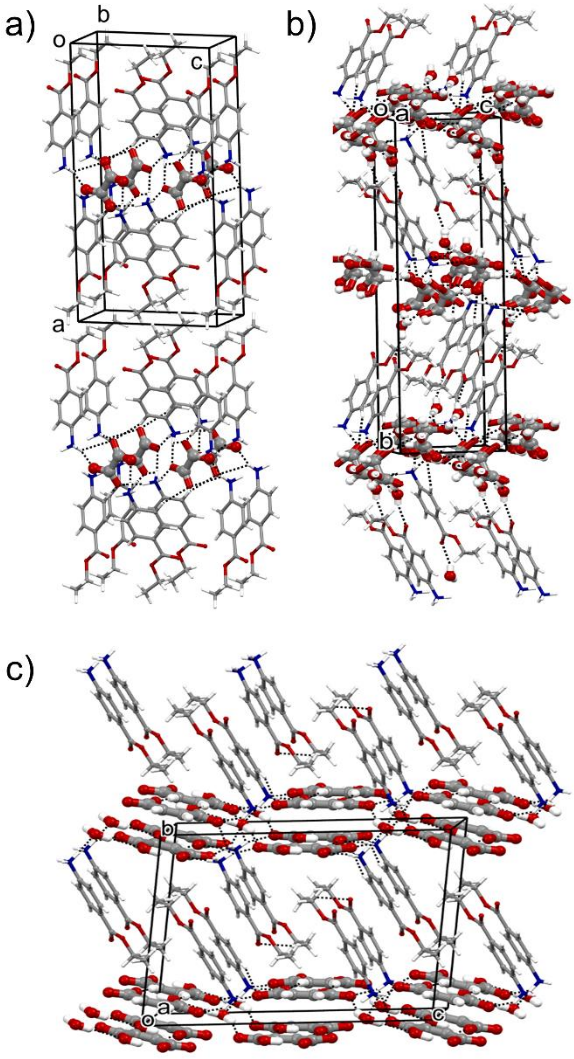

FIGURE 4. 3 *Crystal packing of a) BO, b) BT, c) BMA, highlighting the interaction between anions and cations.*

Benzocaine and sulfonic acids

The BME and BB salts consist of two benzocaine molecules and two counterion molecules that are independent in terms of symmetry. In contrast, BTS contains two benzocaine molecules, two counterion molecules, and one crystallization water molecule, as shown in FIGURE 4.4.

Within the structural arrangements of BME and BB, benzocaine molecules interact with four anion molecules each. The anions play a fundamental role as bridges between the protonated benzocaine molecules in the crystal packing. In BME, for instance, O24 and O14 form hydrogen bonds (HB) with N12 and N11, respectively. Additionally, O34 is engaged in two HBs with symmetry-related N11 (at a distance of 2.90 Å) and N12 (2.83 Å). Similarly, the second anion forms HBs with N11 (2.88 Å) and N12 (2.78 Å) through O33 and O23, respectively, while the third oxygen atom, O13, participates in two HBs with N12 (2.92 Å) and N11 (2.82 Å).

The hydrogen bond network in BB closely resembles that of BME, with the anions serving as intermediaries between cations through an HB network (refer to Chapter 4.3 - FIGURE S6, panels a and b). The BTS network is slightly more complex due to the involvement of an additional water molecule. In this case, an anion interacts with three protonated benzocaine molecules via their O13, O23, and O33 atoms. O13 also accepts an HB from the crystallization water molecule. A similar arrangement is observed for the second anion. The two independent protonated benzocaine molecules are oriented in an almost perpendicular fashion, as depicted in FIGURE 4.5 and Chapter 4.3 - FIGURE S6, panel c. The atoms participating in the hydrogen bonds and their respective distances are summarized in TABLE 4.2.

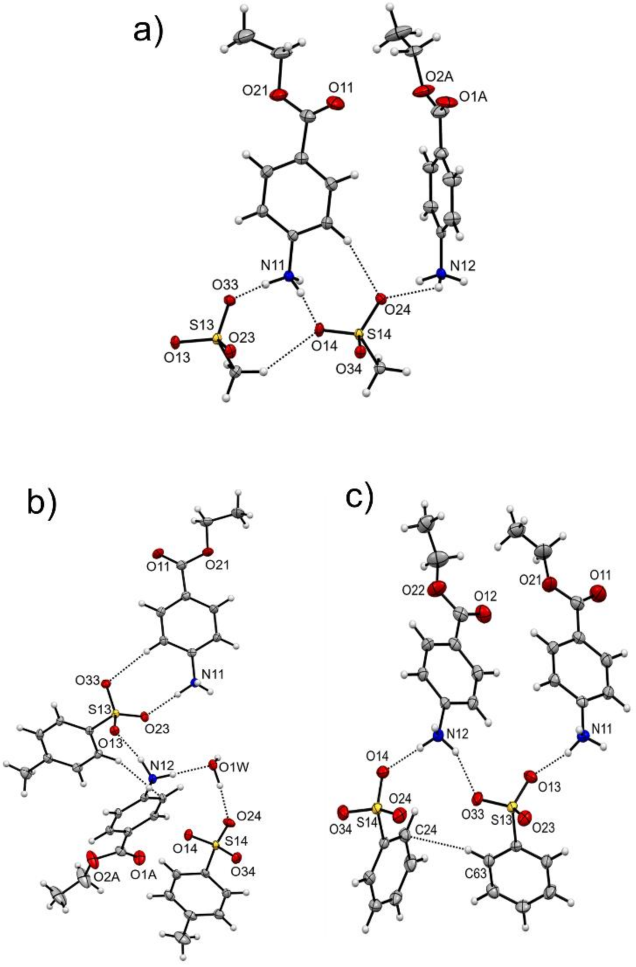

***FIGURE 4. 4** Molecular structure of a) BME, b) BTS, c) BB. Thermal ellipsoids are depicted at the 30% probability level.*

The packing arrangement in BME mirrors a layered structure similar to that of BO. Here, interactions occur between the terminal ethyl ester group of protonated benzocaine molecules related by symmetry, as depicted in FIGURE 4.5a. In contrast to BO, BME's protonated benzocaine molecules do not engage in π···π stacking, but instead, they are aligned in an edgeto-face fashion, facilitated by CH···π interactions (ranging from 4.03 to 4.33 Å) between their aromatic rings.

Similarly, BB also exhibits a layered structure, closely resembling the configurations of BT and BMA. In this case, the protonated benzocaine molecules are arranged head-to-tail, and the aromatic ring of the benzenesulfonic acid induces CH···π interactions among adjacent molecules. Additionally, a network of hydrogen bonds forms between two protonated benzocaine molecules and two counterions. This arrangement is observed in the more intricate BTS crystal, which involves four benzocaine molecules, four p-toluensulfonic acid molecules, and two water molecules, as illustrated in FIGURE 4.5.

Label	HB	HB length (Å)
BB	N11···O34	2.85
	N11···O13	2.74
	N11···O14	2.91
	N11···O23	2.87
	N11···O34	3.01
	N12···O14	2.80
	N12···O33	2.76
	N12···O33	2.81
	N12···O24	3.01
BTS	N11···O33	2.82
	N11···O34	2.99
	N11···O14	2.86
	N11···O23	2.78
	N12···O24	2.89
	N12···O1W	2.90
	N12···O13	2.79
	N12···O1W	2.78
BME	N11···O13	2.82

	N11···O14	2.75
	N11···O34	2.90
	N11···O33	2.88
	N12···O23	2.78
	N12···O34	2.83
	N12···O13	2.92
	N12···O24	2.89

***TABLE 4. 2** HBs between protonated benzocaine and the surrounding anions/water molecules for sulfonate salts with the relative distances (Å).*

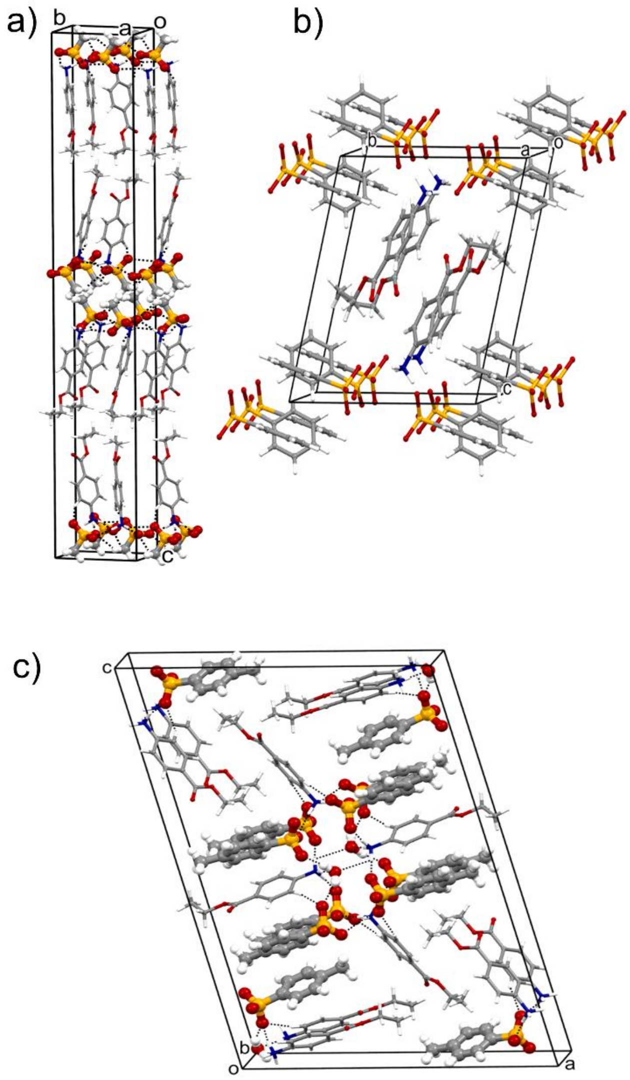

FIGURE 4. 5 *Crystal packing of a) BME, b) BB, c) BTS, highlighting the interaction between anions and cations.*

Benzocaine-ligustrazine cocrystal

In the BL cocrystal, there are two benzocaine molecules that are independent in terms of symmetry, along with one ligustrazine molecule. These molecules interact through two hydrogen bonds. The asymmetric unit and the crystal packing are illustrated in FIGURE 4.6 and Chapter 4.3 - FIGURE S7.

One type of benzocaine (depicted in orange) engages in π-stacking interactions with ligustrazine molecules, in addition to forming hydrogen bonds with ligustrazine N12⋯N23 at a distance of 3.13 Å. It also forms a hydrogen bond with a symmetry-related benzocaine molecule, N12⋯O12, which measures 3.14 Å.

The second benzocaine (depicted in green) participates in two hydrogen bonds. It forms one hydrogen bond with ligustrazine, N11⋯N13, with a bond length of 3.05 Å. Additionally, it forms another hydrogen bond with an adjacent benzocaine molecule, N11⋯O11, at a distance of 2.88 Å (see Chapter 4.3 - FIGURE S7). This second benzocaine molecule is arranged in a head-to-tail fashion, similar to the configuration found in the structures of the salts.

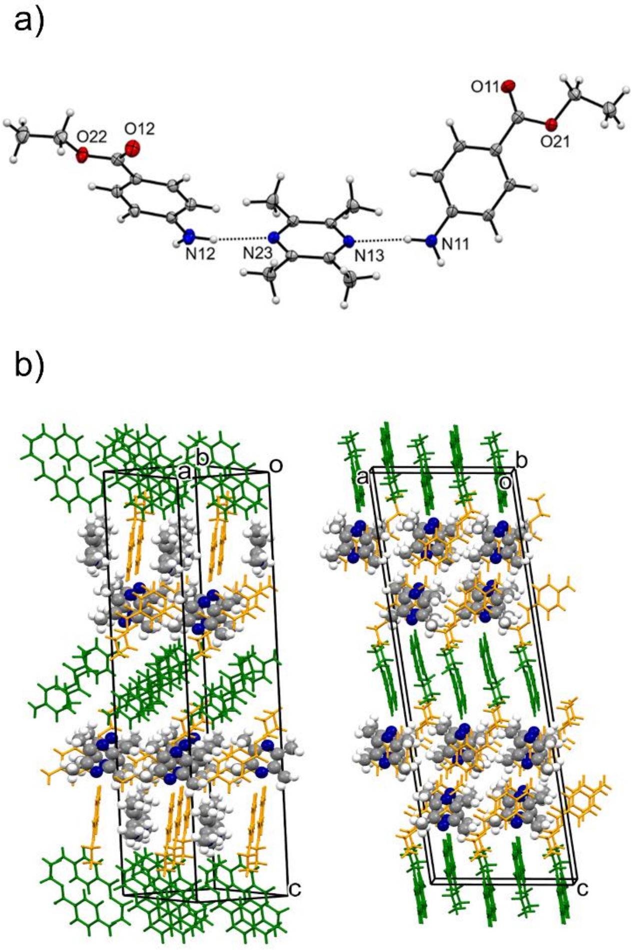

FIGURE 4. 6 *a) Molecular structure of BL with thermal ellipsoids depicted at the 30% probability level. b) Crystal packing of BL, highlighting the interaction between benzocaine and the coformer.*

To comprehensively characterize the bulk materials resulting from salification or cocrystallization, we conducted a comparison between the X-ray powder diffraction patterns (Chapter 4.3 - FIGURE S8) of benzocaine and those of the adducts. The formation of cocrystals or salts was evident from an increase in the unit cell parameters, causing a shift of the diffraction peaks to lower angular values. Most notably, there was no trace of the native benzocaine profile in these patterns. Additionally, the thermal behavior, as investigated through DSC and TGA (Chapter 4.3 - FIGURES S9-12), exhibited distinctive features associated with the formation of the adducts.

These included variations in melting temperature when compared to benzocaine in isolation (refer to TABLE 4.3).

Label	Melting Temperature (°C)
Benzocaine	89
Benzocaine maleate (BMA)	96
Benzocaine mesylate (BME)	211
Benzocaine oxalate (BO)	135
Benzocaine esylate (BE)	157
Benzocaine tartrate (BT)	149
Benzocaine naphtalensulfonate (BN)	217
Benzocaine benzensulfonate (BB)	200
Benzocaine p-toluensulfonate (BTS)	185
Benzocaine camphorsulfonate (BC)	Complex thermal behavior
Benzocaine ligustrazine (BL)	84

TABLE 4. 3 *Melting temperature of benzocaine alone and of every system: BC, BO, BB, BE, BL, BN, BTS, BT, BME and BMA.*

4.1.3.2. Dissolution studies

Comprehending the dissolution rate of a specific substance holds paramount significance as it dictates the speed at which the drug is liberated and becomes accessible for absorption within the body. This fundamental process directly impacts the drug's bioavailability and consequently influences its pharmacological efficacy. A heightened dissolution rate can significantly augment the availability of drug molecules for absorption, a critical consideration for drugs characterized by limited solubility, such as benzocaine.

Our dissolution measurements entailed continuous monitoring of the concentration of benzocaine in each system over time within a biomimetic solution at pH 7.4 phosphate-buffered saline (PBS). This assessment particularly examined the rate at which benzocaine accumulated in the solution, with a specific focus on its concentration during the unsaturation phase. In contrast, solubility denotes the quantity of benzocaine at equilibrium, reached after an extended period within the saturation phase.

The duration of the dissolution experiment extended for 4 hours (FIGURE 4.7). Beyond this point, no significant alteration in the concentration of benzocaine salts and cocrystals was observed, as they reached maximum concentration (1 mg/mL) in all systems. Notably, each newly formed system exhibited an enhanced dissolution rate compared to benzocaine in isolation. This accelerated dissolution rate of the adducts, including salts and cocrystals, amplified the presence of benzocaine in the medium, thereby facilitating potential absorption. This is particularly critical during the initial hours of topical administration.

For instance, at the 15-minute mark, every system had already achieved a higher percentage of dissolved drug compared to benzocaine alone. Specifically, BME, BE, BTS, BC, BN, and BB had already reached the 1 mg/mL threshold, whereas BO, BL, BT, and BMA exhibited a slightly slower dissolution rate, hovering around 0.8 mg/mL. However, even after 1 hour, the drug itself maintained a concentration of 0.54 mg/mL, while all the other systems had fully dissolved, reaching 1 mg/mL.

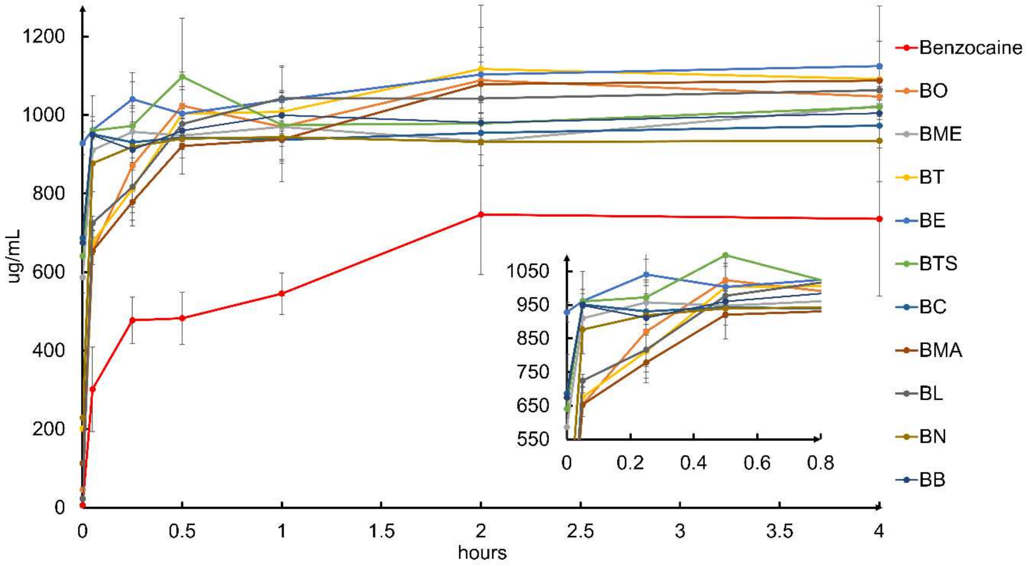

FIGURE 4. 7 *Dissolution profiles of BC, BO, BB, BE, BL, BN, BTS, BT, BME and BMA in PBS up to 4 hours.*

4.1.3.3. Permeability studies

Permeability studies were conducted to shed light on how salification and cocrystallization affect the diffusion of benzocaine across membranes. A high permeability coefficient is vital as it facilitates efficient absorption, allowing benzocaine to swiftly traverse biological membranes. This is particularly crucial in endeavors to enhance the bioavailability of benzocaine.

The experiment involved tracking the accumulation of benzocaine in the acceptor compartment over time. After measuring its concentration and calculating the diffusion rate, the apparent permeability (P_{app}) could be determined by dividing the steady-state flux by the initial concentration in the donor chamber.[142] It's worth noting that, for this experiment, the samples were fully dissolved prior to introduction into the donor compartment, ensuring that the sample preparation step did not affect permeability and remained independent of the dissolution rate.

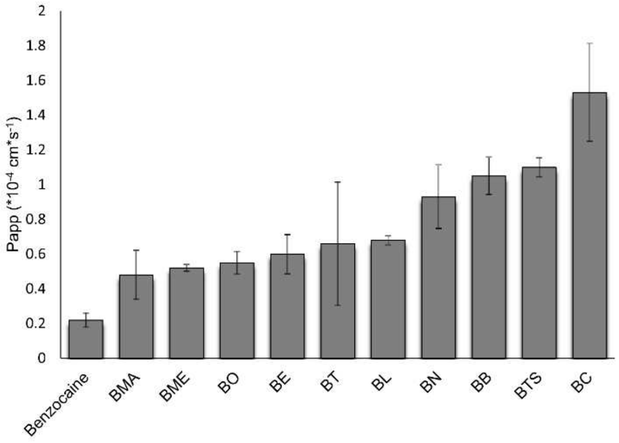

FIGURE 4. 8 *Apparent Permeability of Benzocaine, BC, BO, BB, BE, BL, BN, BTS, BT, BME, and BMA.*

While excipient molecules called chemical permeation enhancers (CPEs) like Transcutol® are employed to increase the P_{app} as they interact with the constituents of the skin,[126,143] crystal engineering has proven equally effective *in vitro*. Notably, as depicted in FIGURE 4.8, all the systems demonstrated distinct and heightened P_{app} values in the tested medium (Chapter 4.3 - TABLE S4 provides detailed results for each repetition). Consequently, the complex formed between benzocaine and its counterpart in solution contributes to the modulation of benzocaine's permeability.

For BB, BTS, and BC, it appears that the lipophilicity of the neutral counterpart is particularly favorable within the series (FIGURE 4.9, logP in TABLE 4.4). This enhanced lipophilicity seems to facilitate membrane diffusion compared to benzocaine alone. Indeed, an increase in the counterpart's lipophilicity within the system corresponds to an increase in P_{app} until reaching a point where it starts to decrease (as observed with BN). Therefore, achieving a delicate and intricate balance in terms of the overall system's lipophilicity appears crucial.

It's important to note that the lipophilic nature of benzocaine and its derivatives significantly influences membrane diffusion rates, impacting the drug's solubility and partitioning within the lipid membrane.

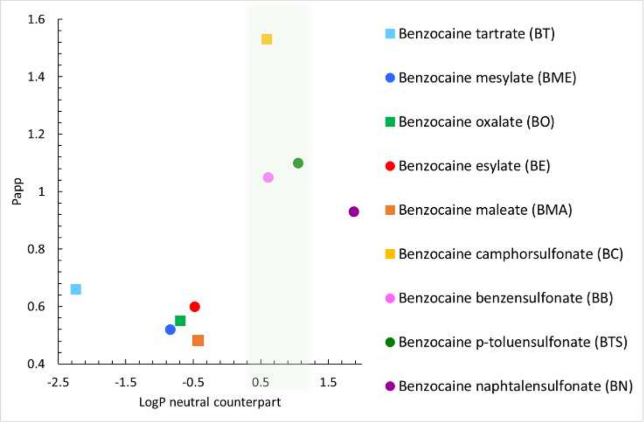

FIGURE 4. 9 *P_{app} and LogP of the neutral counterpart are plotted in the graph, highlighting the range were the LogP is most favorable (0.59-1.05) in increasing the permeability of the final adduct.*

Interestingly, despite ligustrazine exhibiting a favorable lipophilicity, the cocrystal BL shows only a modest P_{app}. The fairly low permeability of BL may be enlightened by the different interactions exchanged by benzocaine and the neutral ligustrazine on the one hand and on the other hand the anionic forms of the acids. Indeed, it is reasonable to assume that the HB in BL is weaker than the HB found in the ionic pairs. Therefore, a weaker intermolecular interaction in solution in BL would reduce the percentage of adduct in solution having the ability to modulate the P_{app} of benzocaine.

Label	**LogP of the neutral counterpart**	**P_{app} (*10^{-4} cm*s^{-1})**
Benzocaine	**-**	**0.22**
Benzocaine tartrate (BT)	-2.24	0.66
Benzocaine mesylate (BME)	-0.84	0.52
Benzocaine oxalate (BO)	-0.69	0.55
Benzocaine esylate (BE)	-0.48	0.60
Benzocaine maleate (BMA)	-0.42	0.48

Benzocaine camphorsulfonate (BC)	0.59	1.53
Benzocaine benzensulfonate (BB)	0.61	1.05
Benzocaine p-toluensulfonate (BTS)	1.05	1.10
Benzocaine naphtalensulfonate (BN)	1.88	0.93
Benzocaine ligustrazine (BL)	*0.78*	*0.68*

TABLE 4. 4 *Apparent permeability P_{app} ($*10^{-4}$ cm$*s^{-1}$) of BC, BO, BB, BE, BL, BN, BTS, BT, BME, and BMA; LogP of the counterions maleic acid, methanesulfonic acid, oxalic acid, ethanesulfonic acid, L-tartaric acid, 2-naphtalensulfonic acid, benzenesulfonic acid, p-toluensulfonic acid, camphorsulfonic acid and the conformer ligustrazine.*

4.1.4. Conclusion

Crystal engineering strategies have demonstrated their potential in addressing the pharmacokinetic challenges inherent to benzocaine like its low bioavailability leading to a short duration of action. Through the synthesis and characterization of nine novel salts and one cocrystal of benzocaine, a deeper understanding of their solid-state properties has been achieved, shedding light on their potential to enhance in vitro properties.

Dissolution and permeability studies have unveiled improved dissolution rates and permeability for these newly synthesized compounds, suggesting their capacity to enhance bioavailability. Notably, within the critical initial 15-30 minutes, all newly synthesized systems were completely dissolved (1 mg/mL), while benzocaine alone remained suspended at a concentration of 0.54 mg/mL.

Furthermore, optimal lipophilicity conditions have been identified for carboxylic and sulfonic acids. Among these, Benzocaine camphorsulfonate (BC) demonstrated the most substantial enhancement in permeability within the series, exhibiting a remarkable 7-fold increase, closely followed by Benzocaine benzenesulfonate (BB) and Benzocaine p-toluensulfonate (BTS), both demonstrating a notable 5-fold increase.

These findings underscore the effectiveness of crystal engineering techniques in tailoring the dissolution rate and permeability of active pharmaceutical ingredients, which can ultimately influence their *in vivo* performance. The exploration of crystal engineering approaches holds promise for optimizing the therapeutic outcomes and patient experiences associated with benzocaine and related compounds.

4.2. Small-Angle X-Ray Scattering and “beating-waves” phenomenon: structural analysis of liposomes loaded with benzocaine salts.

This project was made in collaboration with the Adolphe Merkle Institute, Fribourg, Switzerland.

4.2.1. Introduction

The COVID-19 pandemic has imparted numerous lessons, and the potential for the emergence of swiftly spreading contagious illnesses in the future is undeniable.[144–146] This risk stems from factors such as the growing global population, increased international trade, extensive travel, sedentary lifestyles, heightened meat consumption, the presence of microplastics in the environment, and the proliferation of new diseases due to global warming. As a consequence, it is imperative that pharmaceutical research and development (R&D) become more agile in responding to unforeseen challenges. In the present era, there are approximately 600 liposomal formulations undergoing clinical trials (https://clinicaltrials.gov/) yet achieving quality in production scalability[147] and precise characterization[148] remains a significant obstacle. To put it differently, the successful development of a formulation necessitates both exceptional synthetic skills and efficient processes for characterization and purification.[149]

Liposomes represent the earliest generation of lipid nanoparticles (LNPs). Since their discovery in 1965,[150] these lipid vesicles primarily composed of phosphatidylcholine have been employed for drug delivery, encompassing small molecules and nucleic acids, as biocompatible carriers.[151,152] They consist of an aqueous core enclosed by one or more hydrophobic layers formed from a phospholipid bilayer.[153] This unique structure enables the encapsulation of both hydrophilic and lipophilic drugs, including those residing at the interface between the aqueous core and the bilayer. Liposomes' popularity arises from their ability to shield drugs from degradation and precisely deliver them to their target, thereby minimizing adverse effects.[154] Progress in liposomal formulation development has enabled the targeting of various pathologies, such as cancer, pain, and infections, by optimizing the structure and functionalization of liposome surfaces.[155] Indeed, ionizable cationic lipids can be utilized to interact with systems like mRNA, facilitating their controlled release within cells.[156] This formulation approach proved vital during the COVID-19 pandemic when lipid-based colloidal particles were used to encapsulate mRNA coding for the coronavirus spike protein to produce vaccines.[157]

Similar to many colloidal soft materials, liposomes are dynamic systems[157,158] that respond to outside stimuli.[158] Consequently, liposomes must be studied under noninvasive conditions. While particles' dimension can be determined using techniques such as dynamic and static light scattering,[159] characterizing the deep-level features of the lipid bilayer requires higher resolution and substantial statistical capability,[160] making small-angle X-ray scattering (SAXS) the gold technique.[161]

4.2.2. New SAXS model to interpret data: "beating waves"

SAXS is conceptually straightforward: it involves irradiating a dispersion of lipid particles with a focused beam of quasi-monochromatic soft X-rays, where the photon wavelength falls within the range of approximately 0.1-10 nm.[162] In this process, the X-rays engage in quasi-elastic interactions with the dispersed substance. A position-sensitive area detector is employed to capture the X-rays that have scattered. The scattering pattern, which depicts the intensity of scattering as a function of the scattering angle, offers insights into the three-dimensional distribution of electrons, known as electron density. This distribution is characteristic of the atomic and molecular components that make up the lipid formulation. Consequently, the scattering pattern holds critical information regarding the nanoscale arrangement, orientation, shape, and size of domains within the sample. Mathematically, the recorded scattering pattern is directly related to the square of the three-dimensional Fourier transform of the electron density distribution, denoted as $\rho(\bar{r})$, i.e., $I(q) \propto |\mathrm{FT}\ \rho(\bar{r})|^2$. Thus, by analyzing the SAXS profile, one can quantitatively assess the nanoscale structure and morphology of the studied sample. In the case of liposomes, $|\mathrm{FT}\ \rho(\bar{r})|^2$ is often referred to as the form factor, represented as S(q).[163] The angular dependence is defined by the scattering vector, with its amplitude denoted as $q = 4\pi/\lambda \sin(\theta/2)$, where θ signifies the scattering angle, and λ represents the wavelength. In essence, SAXS furnishes valuable insights into the nanoscale structure and morphology of the sample under examination, typically within the length scale of 1 nm to 100 nm.

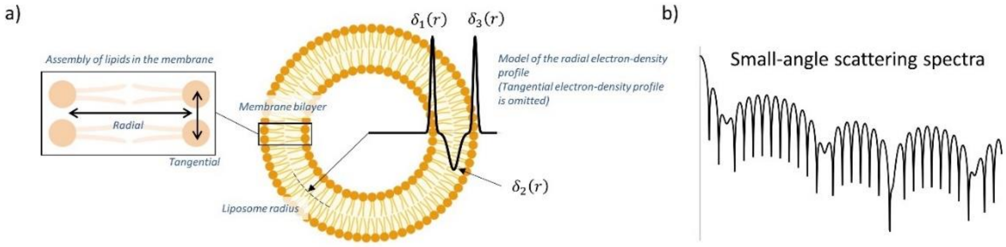

FIGURE 4. 10 *a) Depiction of the cross-sectional configuration of spherical and symmetrical lipid membranes. This spherical and single-layer assembly showcases two primary forms of symmetry: one along the radial direction and another along the tangential direction, as denoted by the arrows. Much like many other studies, this investigation focuses on the radial profile. The solid line (in black) represents a plausible mathematical model for the radial profile of the bilayer's electron density. b) Scattering Pattern: The square of the Fourier transformation of the radial profile (δ(r), Equation 1) provides quantitative insights into the structure of the membrane and can be directly quantified through Small-Angle X-ray Scattering (SAXS).*

Using spherical coordinates, where electron density is a function of radial distance (r), azimuthal angle (dθ), and polar angle (dφ), the Fourier transform can be written as:

1) $$\mathrm{FT}\ \rho(\bar{r}) = \int_0^{2\pi}\int_0^{\pi}\int_0^{\infty} \rho(r,\theta,\varphi)\cdot r^2\cdot \sin\theta \cdot e^{i\cdot q\cdot r\cdot \cos\theta}\,dr\,d\theta\,d\varphi.$$

FIGURE 4.10 provides a simplified representation of a lipid membrane composed of phospholipids with polar head groups, nonpolar tails, and a glycerol backbone. The head groups are hydrophilic, while the tails are hydrophobic, connected by the backbone. As these components exhibit varying electron densities, SAXS allows the study of lipid assembly. In an aqueous environment, liposomes typically exhibit a well-defined membrane-like shell, with head groups facing inward and outward, while tails point inward. Given the primary interest in characterizing the radial bilayer profile, it is often assumed that the systematic variation in the tangential profile, related to head-to-head arrangement, is negligible and can be approximated as isotropic (i.e., $\rho(r, \theta, \varphi)$ is not a function of θ and φ: $(\bar{r}) = \rho(r, \theta, \varphi) = \rho(r)$). This simplification greatly facilitates Equation 1's evaluation, reducing the φ and θ integrals becomes 2π and $2\,\mathrm{sinc}(q \cdot r)$, respectively.

In cases of spherical symmetry (isotropy), the three-dimensional Fourier transform can be expressed as a single integral:

2) $\mathrm{FT}\,\rho(\bar{r}) = 4\pi \int \rho(r) \cdot \mathrm{sinc}(q \cdot r)\, r^2 dr,$

where $\rho(r)$ represents an isotropic radial function embedding the electron density profile of the bilayer structure.

Seminal studies conducted in the early 1970s using X-rays revealed that lipid membranes possess a bilayer structure that can interact with proteins.[164–168] The radial structure at the nano-scale level displayed a consistent profile in the electron density. It originated from the disparity between the electron density of the phospholipids forming the bilayer and that of the surrounding water buffer. This profile featured two distinct peaks separated by a wide fall. The outer peaks represented the head groups with high electron density (composed of P/O/N atoms, surpassing those of the buffer), while the dip indicated the fatty chains with low electron density (comprising C/H atoms, lower than those of the buffer).

This structural perspective remains a prevalent approach in SAXS spectrum analysis,[163,169] with $\rho(r)$ often modeled as the sum of at least three Gaussian functions (FIGURE 4.10a): two for the polar heads and one for the tails and backbone.

3) $\rho(r) = \sum_{i=1}^{3} \rho_i(r)$,

where $\rho_i(r)$ is a Gaussian function with parameters including mean μ_i, variance σ_i^2, and amplitude a_i.

4) $\rho_i(r) = a_i \frac{e^{-\frac{(r-\mu_i)^2}{2\sigma_i^2}}}{\sqrt{2\pi}\sigma_i}$.

Integration in Equation 2 is a linear operation, therefore Equation 3 may be evaluated as:

5) $\mathrm{FT} \sum_{i=1}^{3} \rho_i(r) = \sum_{i=1}^{3} \mathrm{FT}\, \rho_i(r)$.

The Fourier transform of a Gaussian function can be expressed as a closed-form equation:

6) $\mathrm{FT}\, \rho_i(r) = A_i\,(f_i + g_i)$

where $A_i = 4\pi \cdot a_i \cdot e^{-\frac{1}{2}q^2\sigma_i^2}$, $f_i = \sin(\mu_i \cdot q)\frac{\mu_i}{q}$, $g_i = \cos(\mu_i \cdot q) \cdot \sigma_i^2$. One can express now the structure factor

7) $\mathrm{FT}\, \delta(r) = \sum_{i=1}^{3} \mathrm{FT}\, \delta_i(r) = \sum_{i=1}^{3} A_i\,(f_i + g_i)$

and

8) $S(q) = \left|\sum_{i=1}^{3} A_i\,(f_i + g_i)\right|^2$.

Equation 8 operates only on real-valued numbers, and by using the properties of the absolute value function ($|x| = \sqrt{x^2}$, and $|x|^2 = \left(\sqrt{x^2}\right)^2 = ((x^2)^{1/2})^2 = x^{2\cdot 1/2\cdot 2} = x^2$), one may rewrite Equation 8

9) $S(q) = (\sum_{i=1}^{3} A_i\,(f_i + g_i))^2$.

Taking into account the polydispersity in liposome size, Equation 10 involves an integration over the distribution of liposome radius:

10) $S(q) = \int p(r)\, S(q,r) dr$.

While Equation 10 lacks a readily solvable analytical expression, it can be effectively assessed through numerical methods. The introduction of the size distribution p(r) brings forth additional parameters, encompassing the mean radius and standard deviation of the radius, which results in a total of 11 parameters if the bilayer is asymmetric. However, this parametric model presents an elegant solution to the "forward problem," allowing us to predict the Small-Angle X-ray Scattering (SAXS) spectrum using Equations 1 to 10, based on a known electron density radial function of liposomes.

FIGURE 4.11 illustrates some representative simulated scattering spectra for two symmetric bilayers with different radii. These spectra display two prominent characteristics: swift oscillations modulated by a gradually changing envelope function. The fast oscillations are associated with particle size and reduce as the size distribution broadens, converging towards the envelope determined by the structure factor.

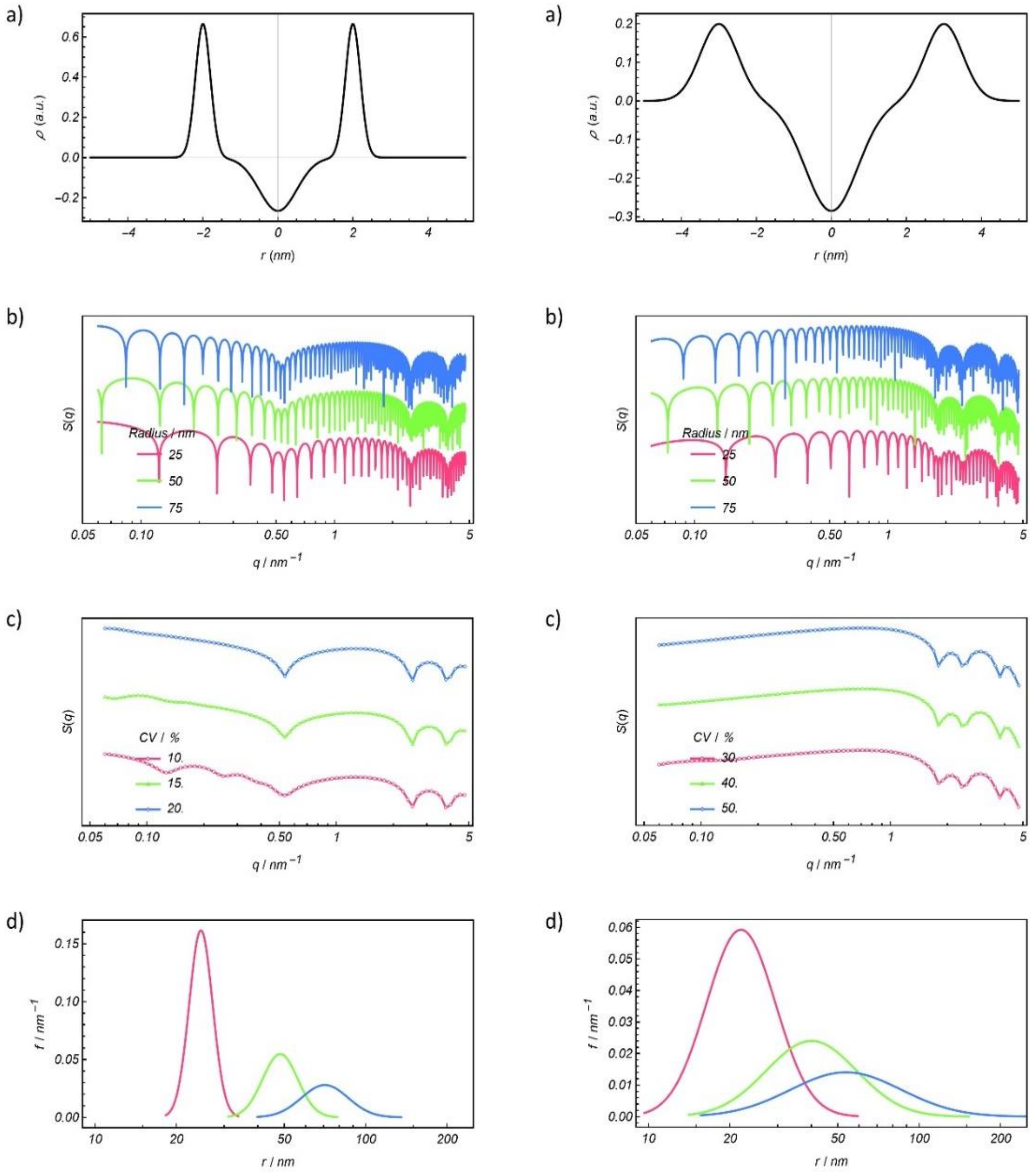

FIGURE 4. 11 *Scattering patterns were calculated using Equations 1 to 10. a) We conducted simulations to create two arbitrary, symmetric radial profiles of liposomes. b) Subsequently, we generated corresponding scattering spectra for these profiles, each with varying radii. Despite their apparent complexity, these spectra exhibit two prominent characteristics: a rapid, oscillating component influenced by particle size and a slowly evolving envelope function. c) The fast oscillations, which are linked to the particle's radius, diminish as the degree of polydispersity in the radius increases. Consequently, the scattering spectra tend to converge towards the envelope defined by the structure factor. The Coefficient of Variation (CV), defined as the ratio of the standard deviation to the mean, quantifies this polydispersity. d) We also generated lognormal distributions of the radius to model the polydispersity observed in these simulations.*

Reversing this transformation, which is termed the "inverse problem," proves to be considerably more challenging, often requiring deep domain-specific expertise. Given that the model can be amenable to parametric examination, ρ(r) is often explicitly defined, and the model is subsequently assessed and regressed against the actual Small-Angle X-ray Scattering (SAXS) spectra. This approach facilitates the deduction of the model's characteristics, which, in turn, provides insights into the structure of the examined bilayer. However, even the most basic Gaussian model entails nine parameters: comprising three amplitudes, three central values, and three width values. In the case of symmetric membranes, this count decreases to six parameters. When accounting for size variability, the number of parameters used for regression expands in accordance with the intricacy of the size distribution.

Numerous freely available computational tools dedicated to the evaluation of small-angle scattering spectra are accessible.[170–174] Nonetheless, the mathematical machinery, may be well beyond the expertise of many scientists working on novel lipid formulations. Our own experience has shown that obtaining a meaningful and converging solution to the problem can be highly tricky. Indeed, we encountered difficulties analyzing simple synthetic data.

In this pursuit, our goal is to create a simple yet valuable alternative method for analyzing lipid bilayer membranes using Small-Angle X-ray Scattering (SAXS). We have two primary objectives in mind: streamlining the complexity of the analysis process and achieving a statistically robust estimation of the mathematical model that describes the profile of the membrane. To attain these goals, our primary focus lies in developing and utilizing the envelope function. While not an exact solution, the envelope function serves as an excellent approximation, taking into account limitations such as noise and resolution typically encountered in SAXS data recorded on laboratory-scale instruments. The observation that Small-Angle X-ray Scattering (SAXS) spectra are relatively unresponsive to the dimensions and size variability of liposomes, with the primary structural insights about the bilayer profile derived from the spectra's envelope (as illustrated in FIGURE 4.11b and c), was initially made in 1975.

Yet, as far as our awareness goes, the significance of this aspect in the analysis of liposomes using Small-Angle X-ray Scattering (SAXS) has not been acknowledged or put into practice previously. We aim to illustrate that this approach is not only uncomplicated but also highly advantageous.

Equation 4 describes the gaussian models of the radial profile, and Equation 9 describes the structure factor. The radius and the thickness of the membrane of the liposomes are such that $\mu_i/q \gg \sigma_i^2$, over the q-range of the SAXS spectra.[167] As a consequence, $f_i \gg g_i$, and thus one can shorten the expression: $f_i + g_i \cong f_i$. Thus, Equation 6 and 9 simplify: $\mathrm{FT}\,\delta_i(r) \cong A_i\, f_i$ and

11) $S(q) \cong \left(\sum_{i=1}^{3} A_i\, f_i\right)^2$.

A straightforward computational series, similar to FIGURE 4.11, can demonstrate that excluding the g_i term has a negligible impact on the observable spectra, as the difference resulting from its inclusion or exclusion in the structure factor is well below the noise level of experimental spectra.

Equation 11 prompts us to consider the structure factor from a different perspective, viewing it as the amplitude of the linear superposition of three harmonic waves. In essence, SAXS fundamentally relies on a well-established wave phenomenon: the interference of coherent waves. It is crucial to state that the membrane’s thickness of these liposomes is small, meaning that the difference $\left|\mu_i - \mu_j\right| \ll \mu_i$, indicating that the frequencies of the waves are very similar. The superposition of harmonic waves with comparable frequencies results in a specific wave phenomenon known as "beating waves" (as illustrated in FIGURE 4.12).

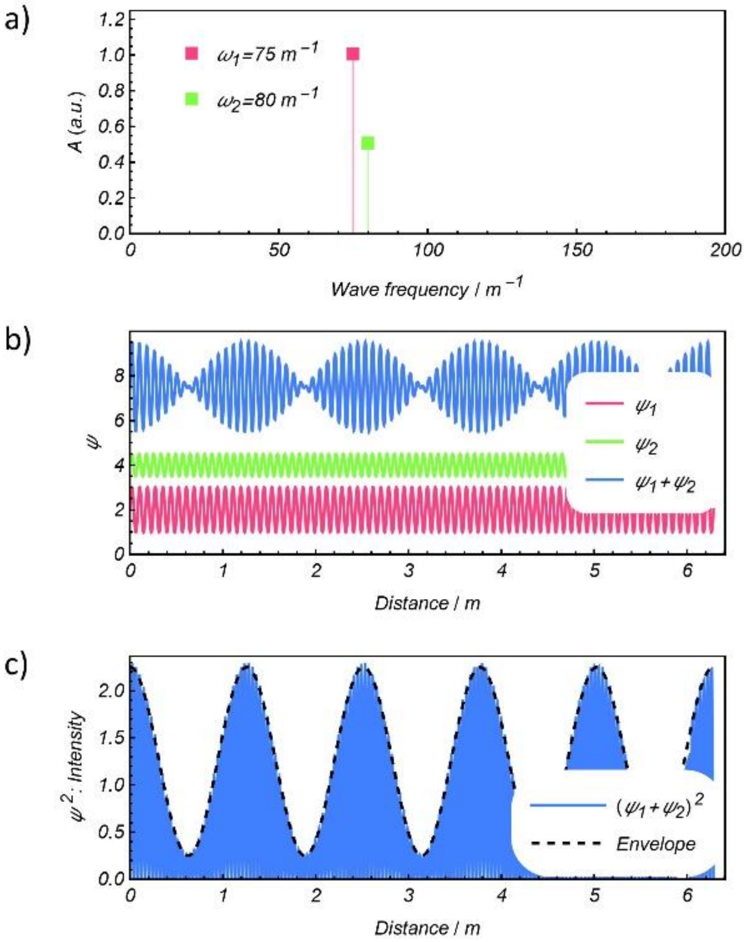

FIGURE 4. 12 *a) The frequency and amplitudes of two harmonic waves, and b) their waveform. The linear superposition of the waves with similar frequencies generates beats, which appear as a slow harmonic modulation of the amplitude of the fast oscillations.*

In fact, what we can reckon in FIGURE 4.12b is the same wave phenomena resultant from the superposition of three waves: $\sum_{i=1}^{3} A_i\, f_i$, and the envelope function is the intensity beats of the three superposing waves. It is easy to demonstration that for N harmonic waves with amplitudes A_i and frequency ω_i, the envelope function is given by:

$$12)\ f_E(x) = \sum_{i=1}^{N} A_i{}^2 + 2\sum_{i=1}^{N-1}\sum_{j>i}^{N} A_i A_j \cdot \cos\left(\omega_{ij} \cdot x\right)$$

where the respective beat frequencies are $\omega_{ij} = \left|\omega_i - \omega_j\right|$. In our case, we can apply Equation 12 to describe SAXS spectra of liposome membranes, where each wave is composed of an amplitude and a harmonic term with frequency μ_i:

$$13)\ 4\pi \cdot a_i \cdot e^{-\frac{1}{2}q^2\sigma_i^2}\ \mu_i/q \times \sin(\mu_i \cdot q)$$

Using Equation 13 and 14, Equation 12 can be easily evaluated and offers simple but lengthy closed-form for the analysis of SAXS spectra on liposomes:

$$14)\ \frac{1}{q^2}\sum_{i=1}^{3} a_i^2 \cdot \mu_i^2 \cdot e^{-q^2\sigma_i^2} + \frac{1}{q^2}\Big(2a_1a_2\mu_1\mu_2 e^{-\frac{1}{2}q^2(\sigma_1^2+\sigma_2^2)} \cos(q(\mu_2-\mu_1)) +$$
$$2a_1a_3\mu_1\mu_3 e^{-\frac{1}{2}q^2(\sigma_1^2+\sigma_3^2)} \cos(q(\mu_3-\mu_1)) +$$
$$2a_2a_3\mu_3\mu_3 e^{-\frac{1}{2}q^2(\sigma_2^2+\sigma_3^2)} \cos(q(\mu_3-\mu_3))\Big).$$

In order to demonstrate how accurate, hands-on, straightforward and robust is this new method to analyze liposome SAXS data in order to structurally characterize the lipid arrangement within the bilayer, 4 samples have been prepared and fully characterized: one placebo liposomal formulation and three loaded liposomes preparations (benzocaine, benzocaine maleate and benzocaine camphorsulfonate).

4.2.3. Materials and Methods

1,2-distearoyl-sn-glycero-3-phosphoethanolamine-N-[succinyl(polyethylene glycol)-2000] (DSPE-PEG2000), 1,2-dipalmitoyl-sn-glycero-3-phosphocholine (DPPC) were purchased from Avanti Polar Lipid (Alabaster, AL, USA). Benzocaine, maleic acid, camphorsulfonic acid cholesterol, phosphate buffer solution (PBS) tablets and chloroform were used as received from MERCK-Sigma Aldrich (Taufkirchen, Germany, EU). Vivaspin® 2 Centrifugal Concentrator Hydrosart® were purchased from Sartorius (Göttingen, Germany). All reagents and solvents were used without further purification.

4.2.3.1. Liposome preparation

Liposomes were prepared by thin-layer evaporation (TLE). Briefly, DPPC, cholesterol, DSPE-PEG200 (6:2:1) (total amount: 60 mg) were dissolved in 2 mL chloroform in a round-bottomed flask. For every sample 4 mg of active compound (whether the drug alone or the salt) were added along with the lipids. After the evaporation of the organic solvent at 60◦ under reduced pressure using the Rotavapor® R-100 from Büchi (Flawil, Switzerland), the lipid film was left under the hood overnight to remove any traces of residual solvent. The lipid film was hydrated with 2 mL of PBS buffer (pH = 7.4) and then subjected to three alternate cycles (3 min each) of warming at 60 ◦C (thermostatic water bath) and vortexing at 700 rpm.

The liposomes were formed by extruding the lipid solution with Avanti Mini extruder (Avanti Catalog #610000-1EA) through a 100 nm (DPPC_Placebo and DPPC_Benzocaine) or 800 nm (DPPC_Benzocaine_Camporsulfonate and DPPC_Benzocaine_Maleate) polycarbonate membrane (Whatman® Nuclepore™ Track-Etched Membranes) 10 times at 60°C.

The washing step was conducted by ultracentrifugation with Avanti J-26XP High Performance Centrifuge from Beckman Coulter (1 h, 40,000 rpm). Briefly the sample were ultracentrifuged inside Vivaspin® 2 Centrifugal Concentrator Hydrosart® and the filtered solution was used to indirectly measure the encapsulation efficacy for the Benzoaine loaded samples and replaced with fresh PBS for every samples to resuspend the liposomes from the pellet on the filter. All formulations obtained were freshly used or stored at 4 ◦C.

Concentration of Benzocaine in the in the washed medium was monitored using a JASCO V-670 UV-Vis-NIR spectrophotometer to measure the encapsulation efficacy (EE%).

4.2.3.2. Dynamic Light Scattering (DLS)

The mean hydrodynamic diameter, polydispersity index and zeta-potential of liposomes were measured at 25°C, through dynamic light scattering, using a Litesizer 500, Anton Paar Instrument (Graz, Austria).

4.2.3.3. Small Angle X-ray Scattering (SAXS)

SAXS measurements were performed at ETH Zurich, Switzerland. We used a Bruker AXS Micro instrument with a microfocused X-ray source, operating at 50 kV and 1000 μA. The Cu Kα radiation (λCu Kα = 1.5418 Å) was collimated by a 2D Kratkycolimator, and the data were collected by a 2D Pilatus 100 K detector. The scattering vector q = (4 π/λ) sinΘ, with 2Θ being the scattering angle, was calibrated using silver behenate. Data were collected and azimuthally averaged using the Saxsgui software to produce unidimensional intensity versus scattering vector q, with a q interval of 0.004 to 0.4 Å-1. The measurements were performed at 25°C. The scattering intensity was collected for 2 h.

4.2.4. Liposome formulations loaded with benzocaine and benzocaine salts

As a proof of concept for the beating wave SAXS model approach, we synthesized four liposome formulations. The excipient components and the preparation process were identical for every sample, with the only difference being the loaded drug. Specifically, one liposome formulation was empty (DPPC_Placebo), one was loaded with benzocaine (DPPC_Benzocaine), and the other two contained two different benzocaine salts. Among the newly synthesized benzocaine systems (Section 4.1), benzocaine maleate and benzocaine camphorsulfonate were encapsulated within liposome formulations (DPPC_Benzocaine_Camporsulfonate and

DPPC_Benzocaine_Maleate), which were then compared to the placebo and the liposome loaded with benzocaine alone.

4.2.4.1. Liposome size and Z-potential

In this section, we present the comprehensive results obtained through Dynamic Light Scattering (DLS) of size and zeta potential analysis of liposomal formulations. These characterizations are pivotal for elucidating the physicochemical properties and stability of liposomes, which play a pivotal role in their efficacy as drug delivery vehicles, encapsulation systems, and nanocarriers for various biomedical applications. The combination of DLS, which provides insights into the size distribution and polydispersity of liposomes, with zeta potential measurements, offering information about their surface charge, allows us to gain a deep understanding of the colloidal stability and potential interactions of these lipid-based nanoparticles. The results discussed herein shed light on the crucial parameters that underpin the behavior and functionality of liposomes, furthering our comprehension of their suitability for specific therapeutic and diagnostic purposes.

TABLE 4.5 presents size, polydispersity, and z-potential data for each of the following samples: DPPC_Placebo, DPPC_Benzocaine_Camporsulfonate, DPPC_Benzocaine, and DPPC_Benzocaine_Maleate. The variations in size among these samples result from our deliberate exploration of different liposome population sizes, demonstrating the robustness and effectiveness of SAXS as a technique for probing deep-level features, despite particle dimension and polydispersity. It is noteworthy that the z-potential values for all samples hover around 0. This is attributed to the pegylation, which masks the negative charge typically found on the surface of such particles.

Label	Size	PDI	Z-potential
DPPC_Placebo	71.89	0.22	0
DPPC_Benzocaine	144.72	0.19	0
DPPC_Benzocaine_Maleate	546.93	0.25	0
DPPC_Benzocaine_Camphorsulfonate	342.51	0.21	0

TABLE 4. 5 *Size, PDI and Zeta-potential is reported for DPPC_Placebo, DPPC_Benzocaine_Camporsulfonate, DPPC_Benzocaine, DPPC_Benzocaine_Maleate*

4.2.4.2. Liposome encapsulation of benzocaine, benzocaine malonate and benzocaine camphorsulfonate

Utilizing the previously described model, we conducted SAXS analysis on four distinct liposome formulations.

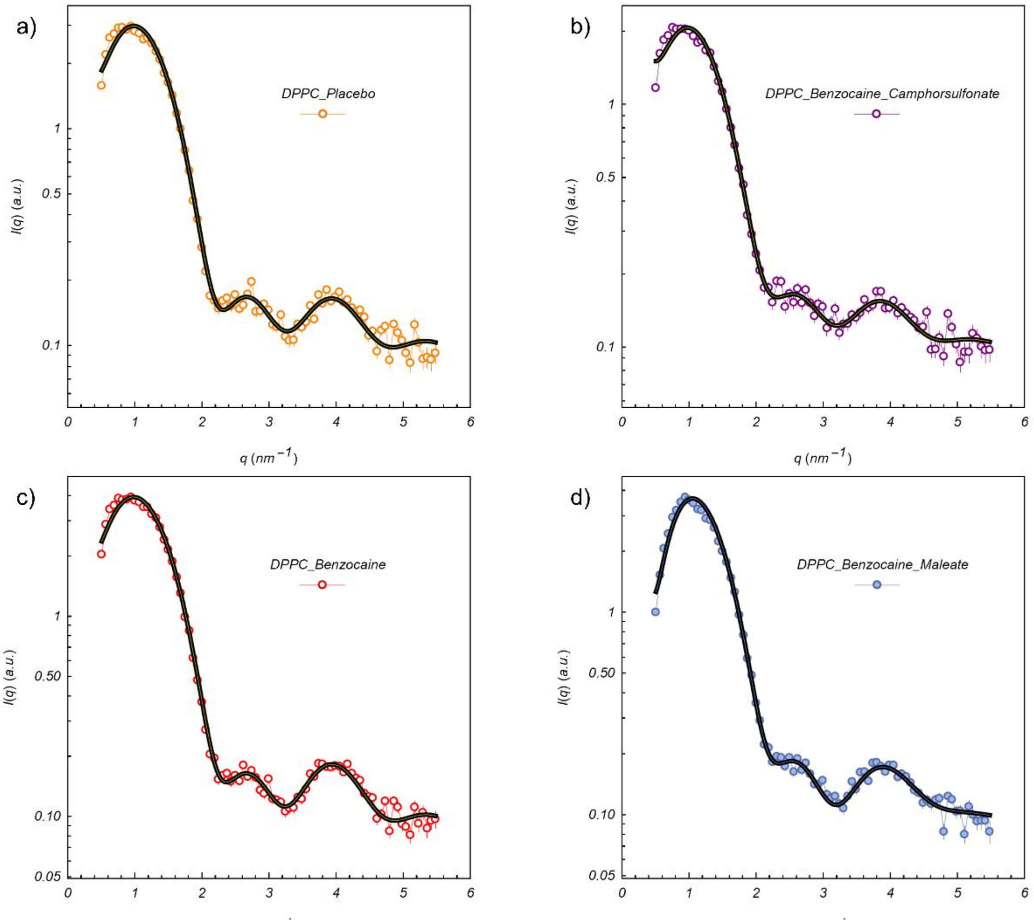

FIGURE 4. 13 *SAXS patterns of different liposomial formulatios: a) DPPC_Placebo (yellow), b) DPPC_Benzocaine_Camporsulfonate (purple), c) DPPC_Benzocaine (red), d) DPPC_Benzocaine_Maleate (blu).*

In FIGURE 4.13, we present the raw data (colored dots) along with the fitting model (black line) for various liposomal formulations, revealing subtle distinctions among the samples. Notably, the characteristic liposomal pattern is evident, characterized by the presence of three discernible peaks. Interestingly, we observe slight variations, particularly between DPPC_Benzocaine_Maleate and the other samples, with the second peak slightly shifted to the left compared to the rest.

Utilizing the previously described mathematical model implemented using Wolfram Mathematica, we conducted a comprehensive analysis of each sample, resulting in the characterization of the electron density profile of the lipid bilayer. Our primary objective was to identify any differences among the samples that might signify distinct arrangements of liposome components and, consequently, variations in the interaction between the drug and excipients.

Given that altering the physicochemical properties of the drug through salification and cocrystallization can impact properties such as dissolution rate and permeability, it is reasonable to hypothesize that these modifications could influence the molecule's partitioning within a lipid environment, such as a liposome, as well.

The bilayer's profile was expressed in terms of real distance (nm) and the electron density difference (ρ) obtained subtracting the electron density of the buffer from the one of the bilayer. Specifically, a noticeable contrast emerges in the central region (FIGURE 4.14). This suggests the localization of benzocaine between the lipid tails, as evidenced by the heightened contrast in the central Gaussian corresponding to the tail-tail segment of the bilayer. Indeed, after encapsulating a hydrophobic molecule within the lipid bilayer, a subsequent disruption of the phospholipid's arrangement might occur. Consequently, the electron density per unit volume would decrease, leading to a bigger overall contrast.

Encapsulation Efficiency (EE%) data presented in TABLE 4.6 is quite similar for every sample, consistent with the previously discussed increase in electron density profile contrast.

Label	**Encapsulation Efficacy (EE) %**
DPPC_Placebo	-
DPPC_Benzocaine	35.04
DPPC_Benzocaine_Maleate	16.16

DPPC_Benzocaine_Camphorsulfonate	23.42

TABLE 4. 6 *Encapsulation efficacy of DPPC_Placebo, DPPC_Benzocaine_Camporsulfonate, DPPC_Benzocaine, DPPC_Benzocaine_Maleate.*

Furthermore, the electron density profile analysis reveals an expansion of the bilayer in the DPPC_Benzocaine_Maleate formulation, indicated by the larger distance between the beginning of the inward head Gaussian and the end of the outward head Gaussian. This increase signifies a change in the bilayer arrangement attributable to the altered physiochemical properties of benzocaine maleate compared to benzocaine alone, guaranteeing the encapsulation of the salt. This different structural organization could potentially lead to an ameliorated *in vivo* release, providing the effective synergy of crystal engineering and formulation engineering. In contrast, Benzocaine Camphorsulfonate shows only minor differences compared to the placebo liposomes, possibly due to the lower stability of the salt throughout the liposome production process (see FIGURE 4.14).

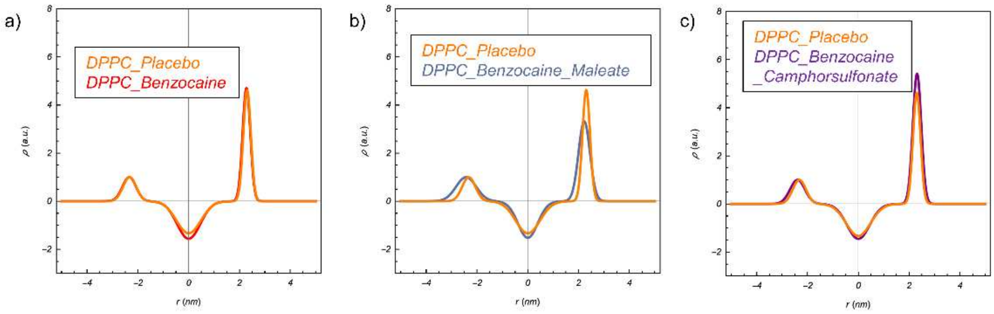

FIGURE 4. 14 *Electron density profile of the bilayer of different liposomial formulatios: a) DPPC_Placebo (yellow) and DPPC_Benzocaine (red) superimposed, b) DPPC_Placebo (yellow) and DPPC_Benzocaine_Maleate (blu) superimposed, c) DPPC_Placebo (yellow) and DPPC_Benzocaine_Camporsulfonate (purple) superimposed.*

4.2.5. Conclusions

In conclusion, the lessons learned from the COVID-19 pandemic have underscored the urgent need for more agile pharmaceutical research and development (R&D) capabilities to respond effectively to emerging contagious diseases.

Our research, as presented in this study, contributes to addressing this challenge by focusing on the development and characterization of liposomal formulations, with a specific focus on benzocaine.

Indeed, our study emphasizes the importance of characterizing liposomes under native conditions, utilizing noninvasive and non-destructive techniques. Small-angle X-ray scattering (SAXS) stands out as a preferred method due to its ability to provide sub-nanometer resolution and detailed structural information about lipid bilayer membranes.

This work highlights benzocaine's unique localization between lipid tails, as evidenced by the electron density profile. Moreover, our results demonstrate that the physiochemical properties of benzocaine maleate can induce an expansion of the bilayer, indicating a change in the liposome's arrangement compared to benzocaine alone.

While SAXS data analysis can be complex, we introduced a simplified yet valuable alternative: the “beating wave” approach. We focus on deriving and leveraging the envelope function, which offers a statistically accurate approximation of the parametric model describing the electron-density profile of the bilayer. This approach addresses the challenges often encountered in SAXS analysis, making it more accessible to a broader range of scientists working on lipid formulations.

4.3. Supporting Information

Benzocaine with sulfonates

	BB	**BME**	**BTS**
Empirical formula	$C_6H_5O_3S$, $C_9H_{12}NO_2$	CH_3O_3S, $C_9H_{12}NO_2$	$C_7H_7O_3S$, 0.5(H_2O), $C_9H_{12}NC$
Formula weight	323.35	261.29	346.39
Temperature/K	200.0	200.0	200.00
Crystal system	triclinic	monoclinic	monoclinic
Space group	P-1	P21/c	$P2_1/n$
a/Å	10.8211(5)	7.0931(2)	20.7447(14)
b/Å	11.5975(6)	7.2313(2)	5.7433(4)
c/Å	13.6976(7)	49.8976(12)	30.291(2)
α/°	74.634(2)	90	90
β/°	70.376(2)	93.8690(10)	103.760(2)
γ/°	70.311(2)	90	90
Volume/Å^3	1502.00(13)	2553.53(12)	3505.4(4)
Z	4	8	8
ρ_{calc}g/cm^3	1.430	1.359	1.313
μ/mm^{-1}	0.239	2.372	0.212
F(000)	680.0	1104.0	1464.0
Crystal size/mm^3	0.17 × 0.13 × 0.12	0.13 × 0.12 × 0.1	0.19 × 0.19 × 0.09
Radiation	MoKα (λ = 0.71073 Å)	CuKα (λ = 1.54178 Å)	MoKα (λ = 0.71073 Å)
2Θ range for data collection/°	4.154 to 51.504	7.102 to 140.414	4.042 to 51.498
Index ranges	$-13 \leq h \leq 13$, $-14 \leq k \leq 14$, $-16 \leq l \leq 16$	$-8 \leq h \leq 8$, $-8 \leq k \leq 8$, $-60 \leq l \leq 60$	$-25 \leq h \leq 25$, $-7 \leq k \leq 7$, $-36 \leq$
Reflections collected	42505	50585	78967
Independent reflections	5736 [$R_{in\,t}$= 0.0377, R_{sigma} = 0.0205]	4877 [R_{int} = 0.0888, R_{sigma} = 0.0390]	6646 [R_{int} = 0.0587, R_{sigma} = 0.0227]
Data/restraints/parameters	5736/0/401	4877/34/372	6646/44/498
Goodness-of-fit on F^2	1.045	1.041	1.073
Final R indexes [I>=2σ (I)]	R_1 = 0.0307, wR_2 = 0.0808	R_1 = 0.0455, wR_2 = 0.1068	R_1 = 0.0495, wR_2 = 0.1222
Final R indexes [all data]	R_1 = 0.0355, wR_2 = 0.0837	R_1 = 0.0688, wR_2 = 0.1188	R_1 = 0.0566, wR_2 = 0.1265
Largest diff. peak/hole / e Å^{-3}	0.36/-0.37	0.20/-0.46	0.31/-0.39

TABLE S1. *Summary of X-ray crystallographic data for BB, BME and BTS.*

Benzocaine with carboxylates

	BO	**BMA**	**BT**
Empirical formula	C_2O_4, $2(C_9H_{12}NO_2)$	$C_4H_3O_4$, $0.5(H_2O)$, $C_9H_{12}NO_2$	$C_4H_5O_6$, H_2O, $C_9H_{12}NO_2$
Formula weight	420.41	290.27	333.29
Temperature/K	200.0	200.0	200.0
Crystal system	monoclinic	triclinic	monoclinic
Space group	P2/c	P-1	$P2_1$
a/Å	21.7639(7)	5.6713(3)	7.1627(6)
b/Å	3.75900(10)	13.8506(7)	28.0108(19)
c/Å	12.3116(4)	17.9533(9)	7.9947(5)
α/°	90	83.295(4)	90
β/°	95.138(2)	85.782(4)	93.688(4)
γ/°	90	85.211(4)	90
Volume/$Å^3$	1003.17(5)	1392.81(12)	1600.7(2)
Z	2	4	4
ρ_{calc}g/cm^3	1.392	1.384	1.383
μ/mm^{-1}	0.915	0.956	1.022
F(000)	444.0	612.0	704.0
Crystal size/mm^3	0.18 × 0.14 × 0.12	0.19 × 0.07 × 0.07	0.21 × 0.17 × 0.013
Radiation	CuKα (λ = 1.54178 Å)	CuKα (λ = 1.54184 Å)	CuKα (λ = 1.54178 Å)
2Θ range for data collection/°	8.158 to 149.028	4.966 to 141.644	11.09 to 140.46
Index ranges	$-27 \leq h \leq 27$, $-4 \leq k \leq 4$, $-15 \leq l \leq 12$	$-6 \leq h \leq 6$, $-16 \leq k \leq 16$, $-21 \leq l \leq 21$	$-8 \leq h \leq 7$, $-33 \leq k \leq 34$, $-9 \leq$
Reflections collected	13072	5129	24264
Independent reflections	2051 [R_{int} = 0.0349, R_{sigma} = 0.0256]	5129 [R_{int} = 0.0739, R_{sigma} = 0.0735]	6075 [R_{int} = 0.0547, R_{sigma} = 0.0420]
Data/restraints/parameters	2051/2/175	5129/11/412	6075/13/485
Goodness-of-fit on F^2	1.043	1.064	1.032
Final R indexes [I>=2σ (I)]	R_1 = 0.0389, wR_2 = 0.1046	R_1 = 0.0728, wR_2 = 0.1712	R_1 = 0.0377, wR_2 = 0.0842
Final R indexes [all data]	R_1 = 0.0426, wR_2 = 0.1081	R_1 = 0.1149, wR_2 = 0.1899	R_1 = 0.0451, wR_2 = 0.0882
Largest diff. peak/hole / e $Å^{-3}$	0.33/-0.17	0.22/-0.29	0.29/-0.21
Flack Parameter			0.10(9)

TABLE S2. *Summary of X-ray crystallographic data for BO, BMA and BT.*

Benzocaine cocrystal

	BL
Empirical formula	$2(C_9H_{11}NO_2), C_8H_{12}N_2$
Formula weight	466.57
Temperature/K	200.0
Crystal system	monoclinic
Space group	C2/c
a/Å	14.4400(3)
b/Å	8.3412(2)
c/Å	43.4534(11)
α/°	90
β/°	98.3390(10)
γ/°	90
Volume/Å^3	5178.5(2)
Z	8
ρ_{calc}g/cm^3	1.197
μ/mm^{-1}	0.082
F(000)	2000.0
Crystal size/mm^3	0.21 × 0.16 × 0.13
Radiation	MoKα (λ = 0.71073 Å)
2Θ range for data collection/°	3.79 to 51.418
Index ranges	$-17 \le h \le 17$, $-10 \le k \le 9$, $-39 \le l \le 52$
Reflections collected	22834
Independent reflections	4929 [R_{int} = 0.0298, R_{sigma} = 0.0237]
Data/restraints/parameters	4929/4/329
Goodness-of-fit on F^2	1.082
Final R indexes [I>=2σ (I)]	R_1 = 0.0528, wR_2 = 0.1204
Final R indexes [all data]	R_1 = 0.0624, wR_2 = 0.1253
Largest diff. peak/hole / e Å^{-3}	0.14/-0.20

TABLE S3. *Summary of X-ray crystallographic data for BL.*

Fingerprint plot (CrystalExplorer)

The distinct profiles of the fingerprint plots highlighted a significantly altered interaction pattern for protonated benzocaine in the presence of organic acids compared to benzocaine in isolation. The symmetric profile of neutral benzocaine's fingerprint plots appeared to shift toward a less symmetrical interaction landscape in the presence of carboxylic or sulfonic acid derivatives. This shift likely resulted from the formation of strong and directional hydrogen bonds between anions and cations.

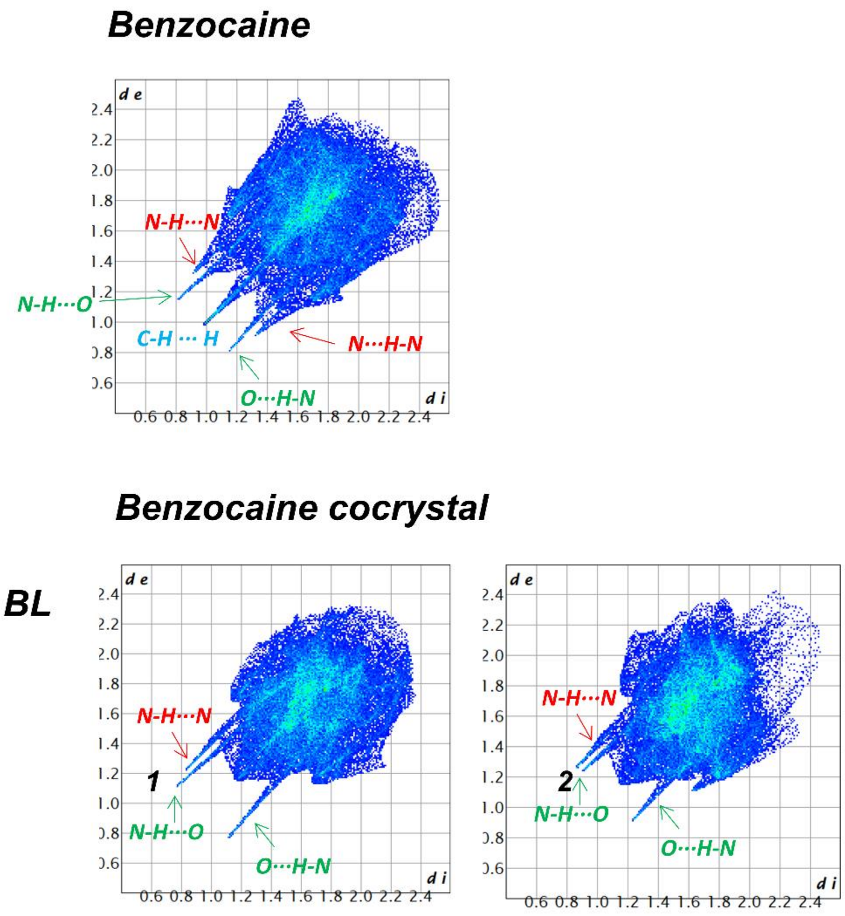

__FIGURE S1.__ 2D fingerprint plot. Drawings plotted using CrystalExplorer of benzocaine alone (QQQAXG01) and BL. Molecules 1 and 2 are the asymmetric molecules in the asymmetric unit, as reported in FIGURE 4.6. In green are reported the interactions where both nitrogen and oxygen are involved, while red are the interactions where N is both donor and acceptor of HB.

Benzocaine with carboxylates

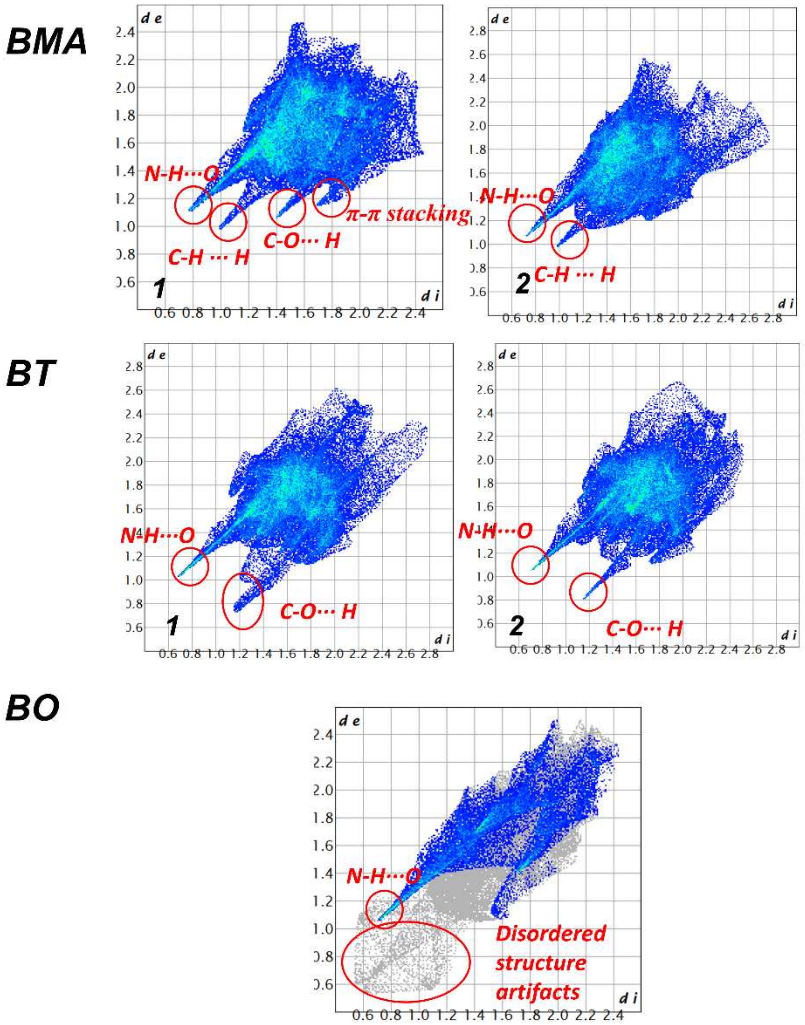

FIGURE S2. *2D fingerprint plot. Drawings plotted using CrystalExplorer of BMA, BT and BO. Molecules 1 and 2 are the asymmetric molecules in the asymmetric unit, as reported in FIGURE 4.2.*

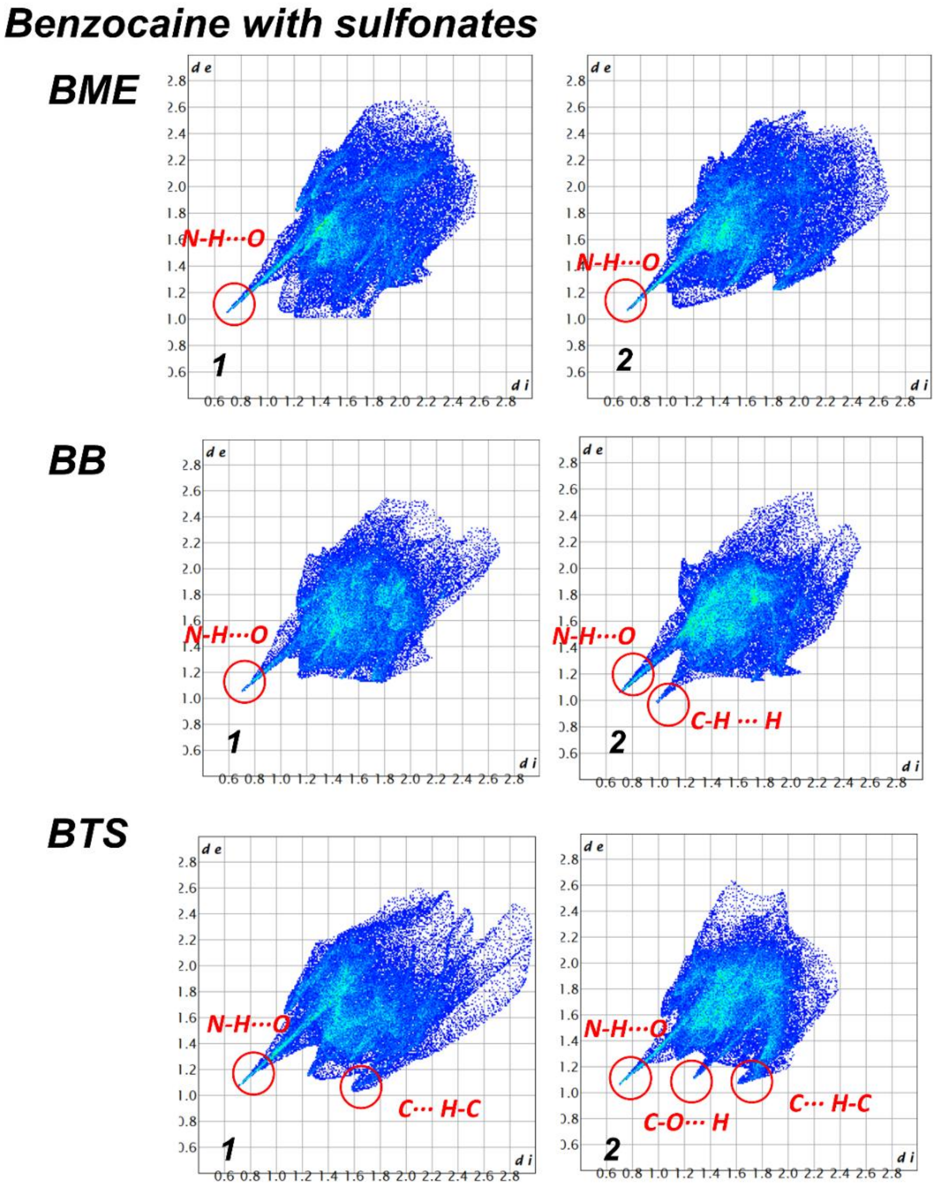

FIGURE S3. *2D fingerprint plot. Drawings plotted using CrystalExplorer of BME, BB and BTS. Molecules 1 and 2 are the asymmetric molecules in the asymmetric unit, as reported in FIGURE 4.4.*

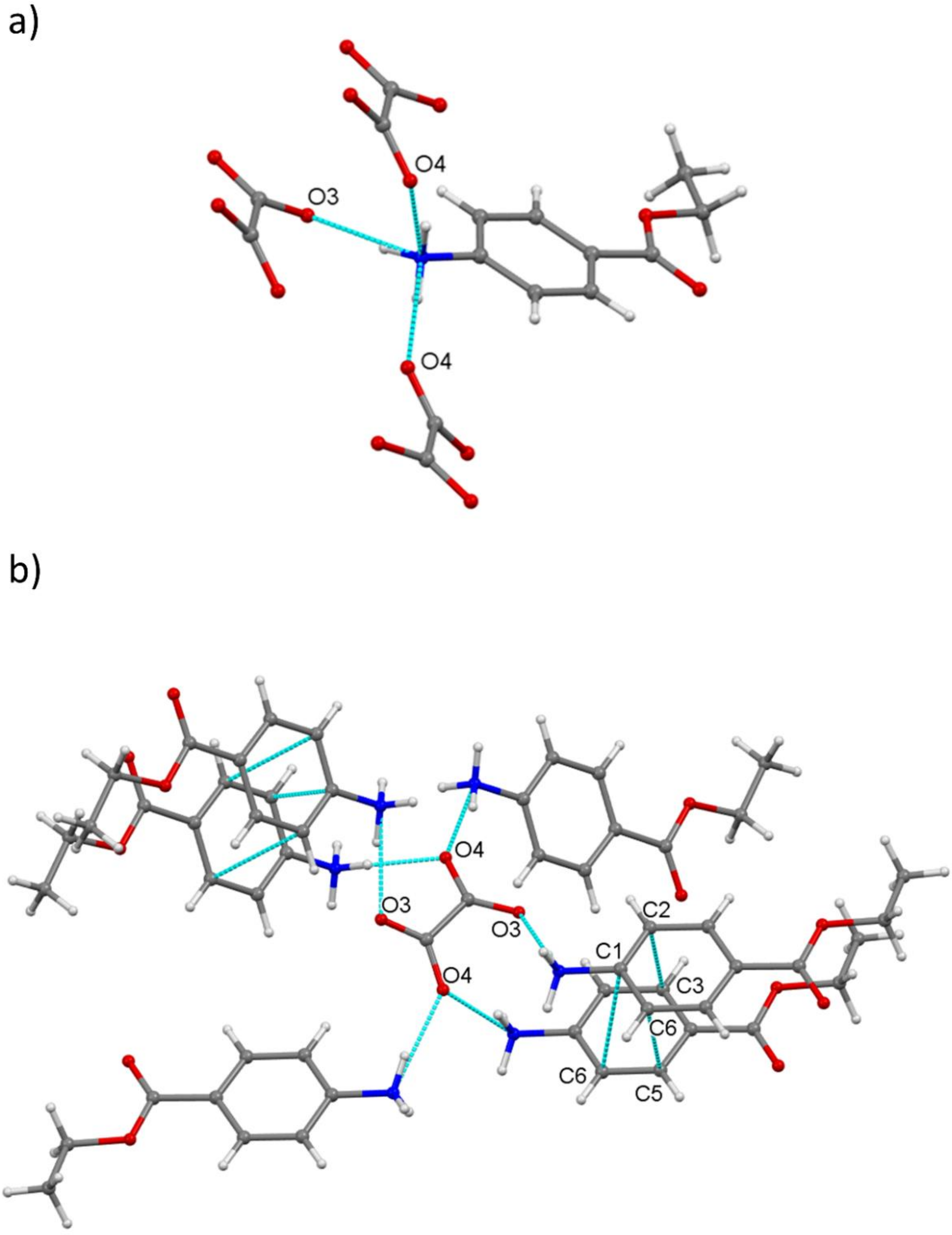

FIGURE S4. *a) BO structure highlighting the HBs between protonated benzocaine and oxalic acid. b)3D network of HBs surrounding a molecule of di-deprotonated oxalic acid.*

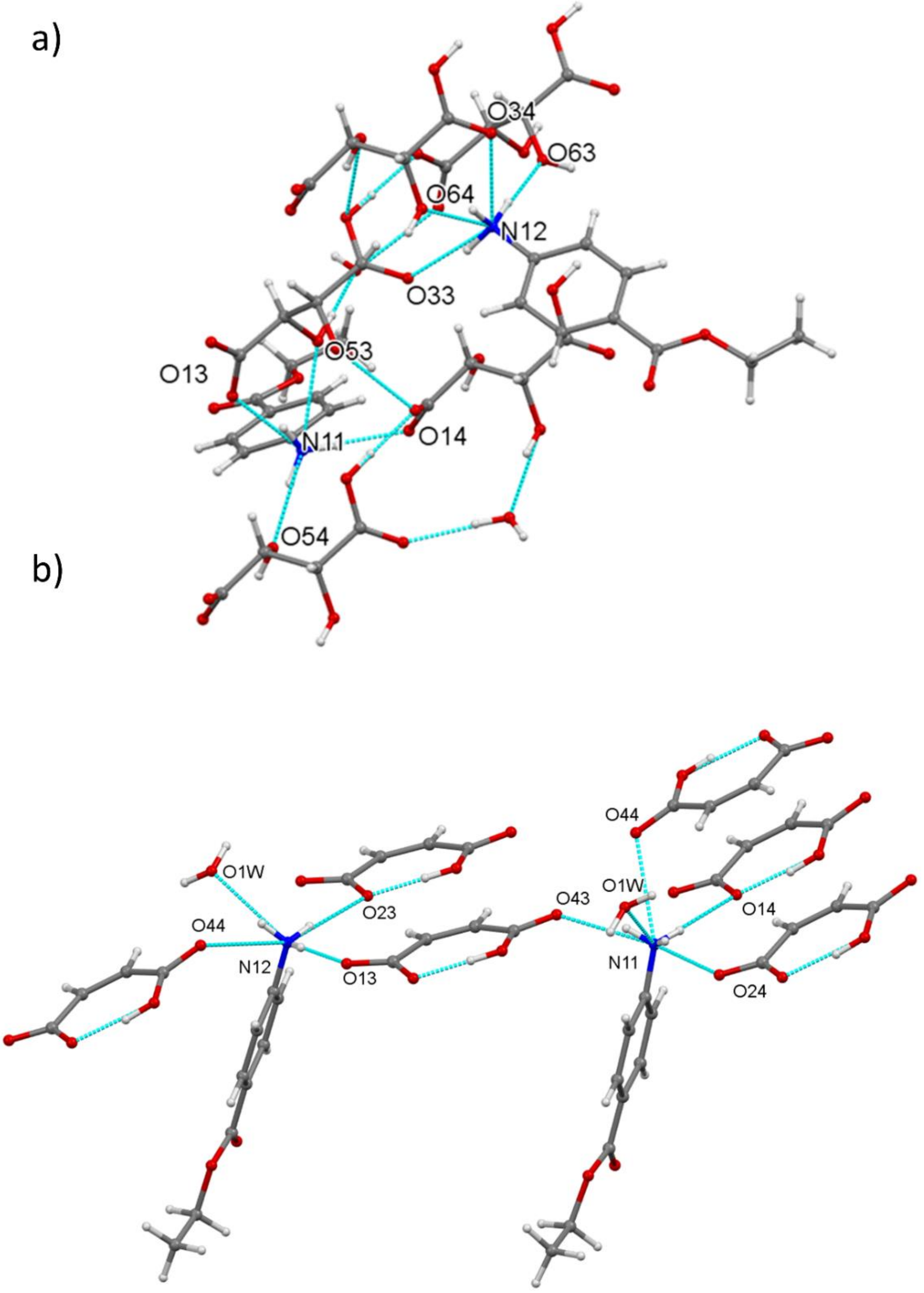

FIGURE S5. *a) BT and b) BMA structure highlighting the HBs between protonated benzocaine and the monodeprotonated acids.*

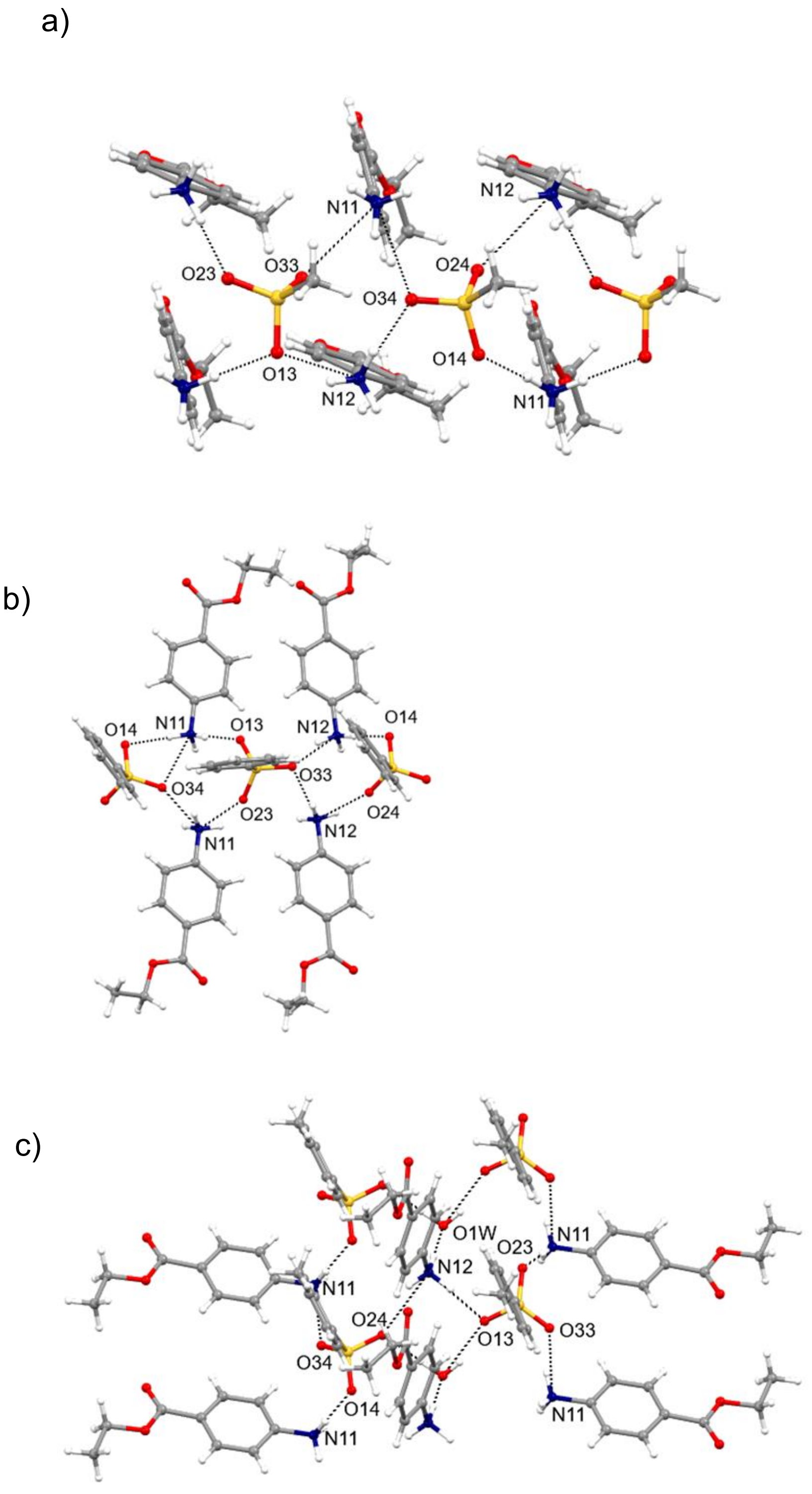

FIGURE S6. *a) BME, b) BB and c) BTS structures highlighting the HBs between protonated benzocaine and the acids..*

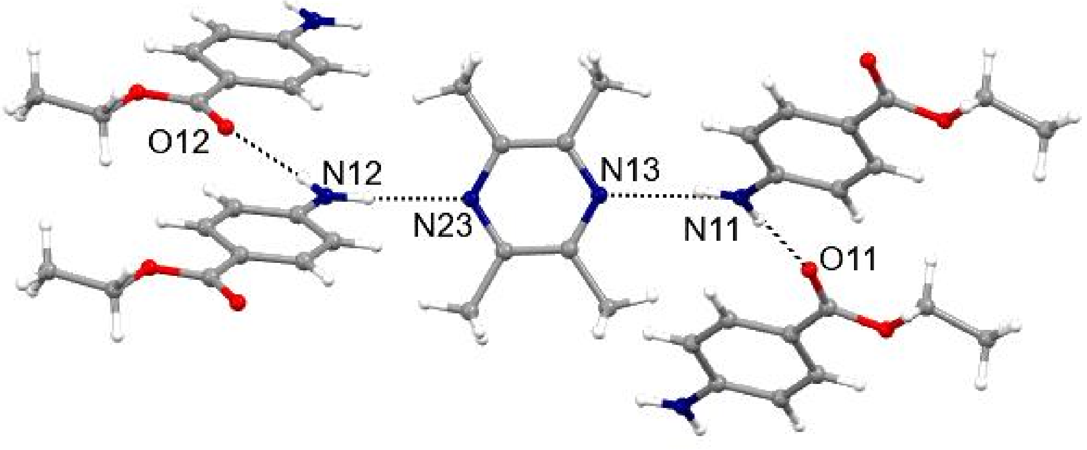

FIGURE S7. *BL structures highlighting the HBs between benzocaine and ligustrazine..*

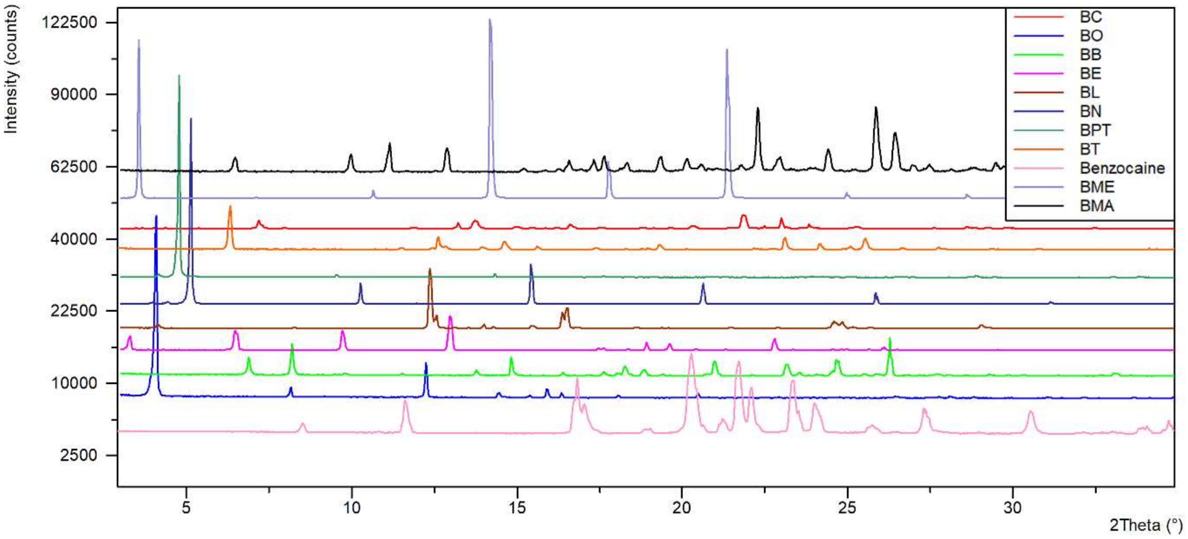

FIGURE S8. *Diffraction patterns of benzocaine and all the newly formed systems: BC, BO, BB, BE, BL, BN, BPT, BT, BME and BMA.*

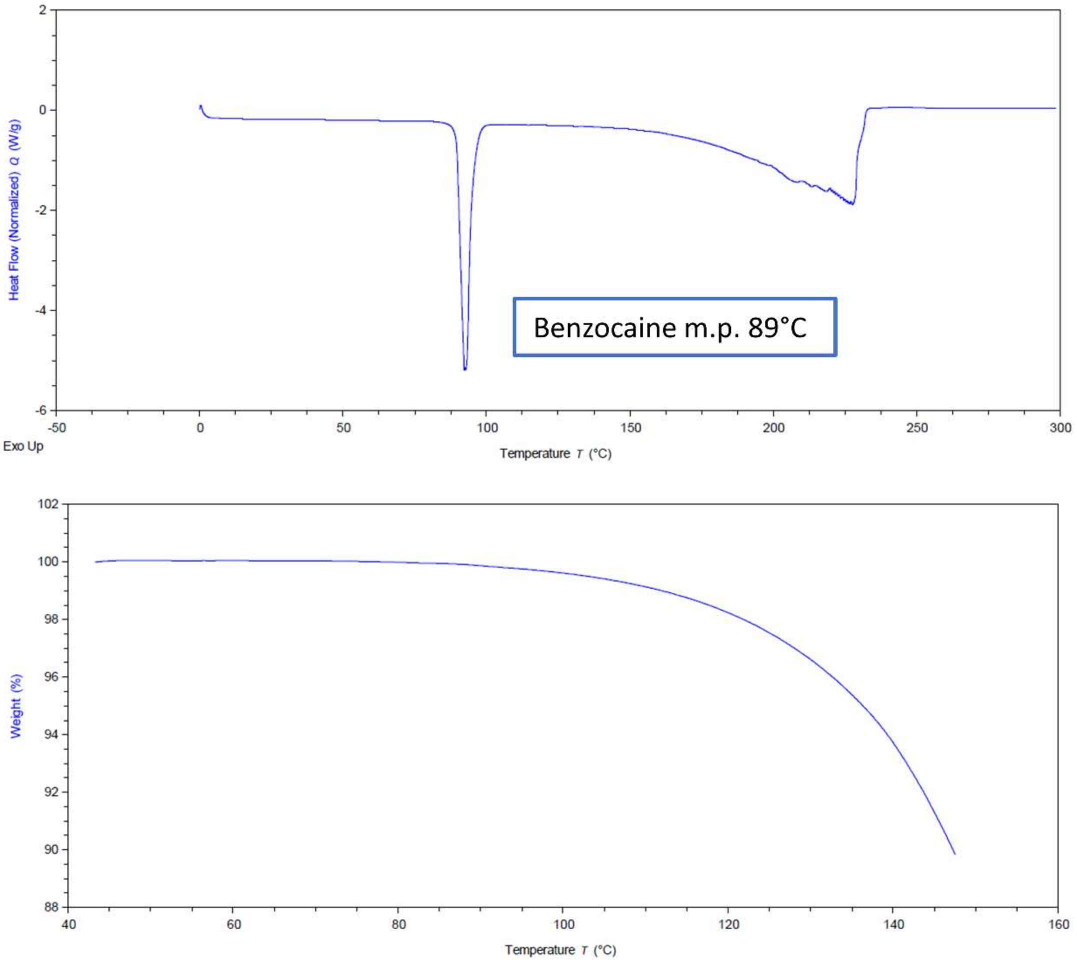

FIGURE S9. *DSC and TGA thermograms of benzocaine alone.*

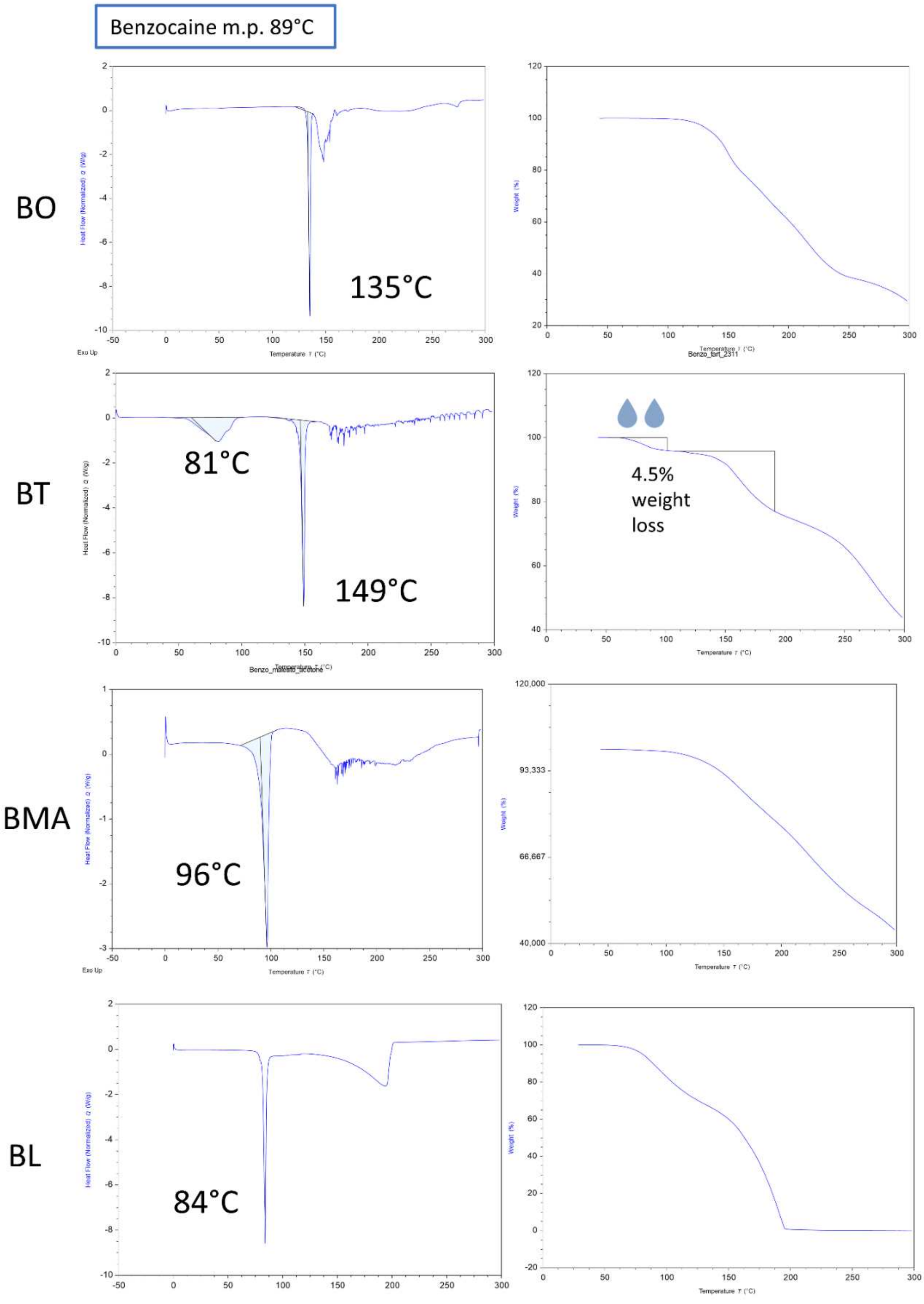

__FIGURE S10.__ DSC and TGA thermograms of BO, BT, BMA, BL.

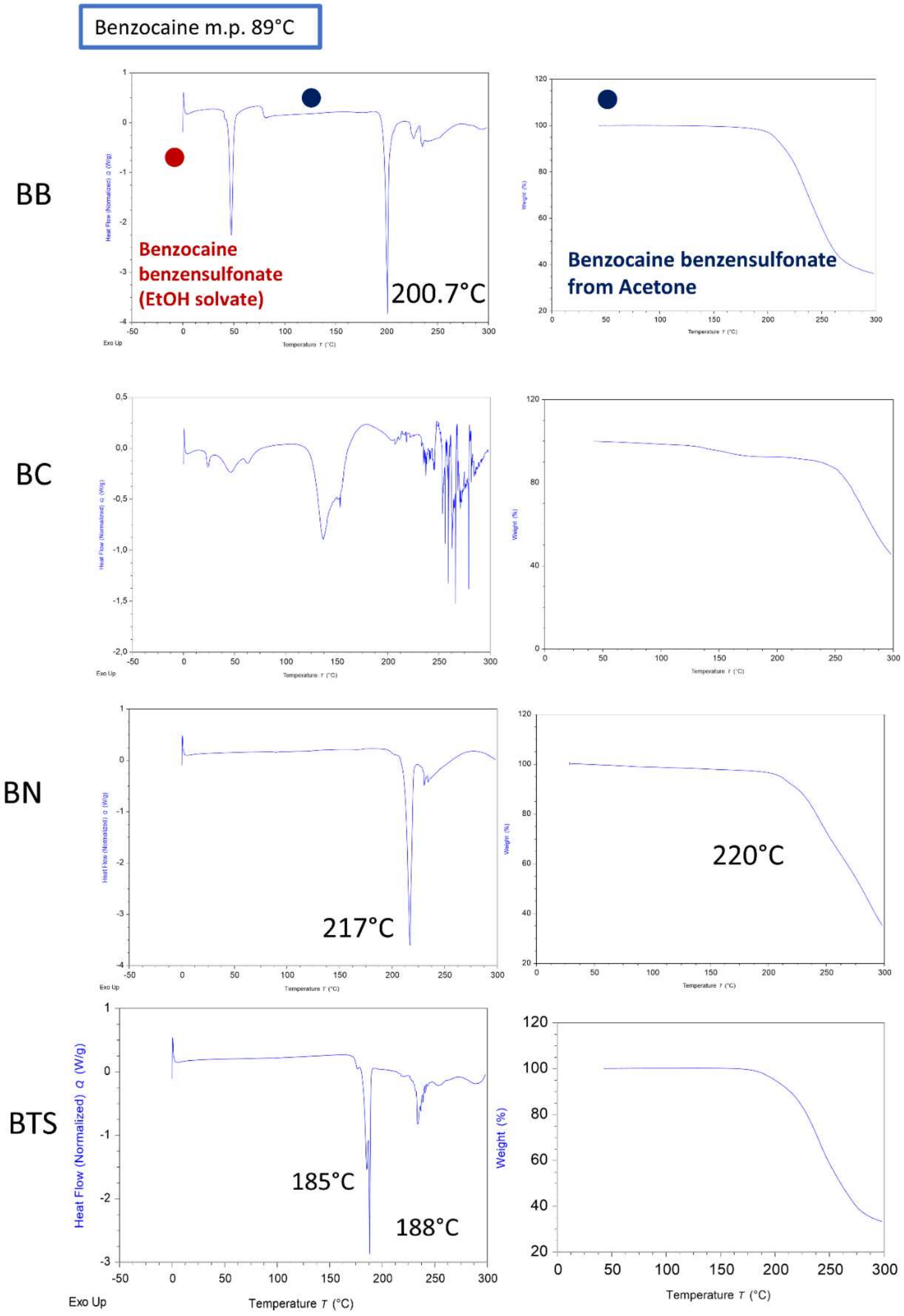

__FIGURE S11.__ DSC and TGA thermograms of BB, BC, BN, BPT.

BME

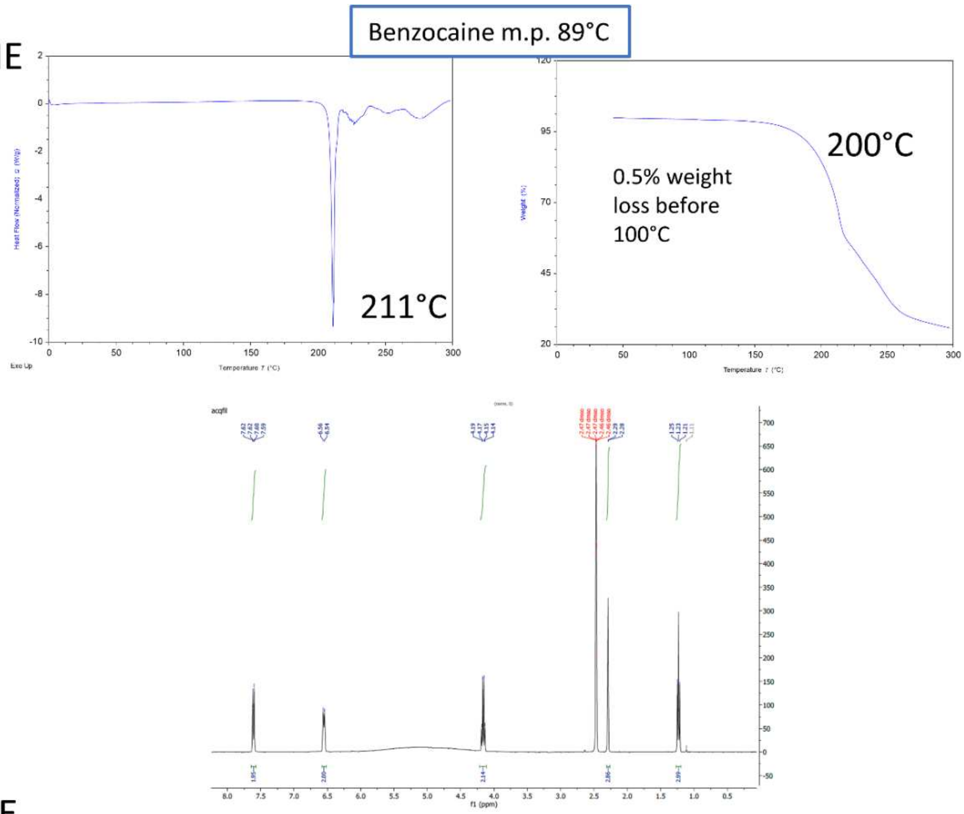

BE

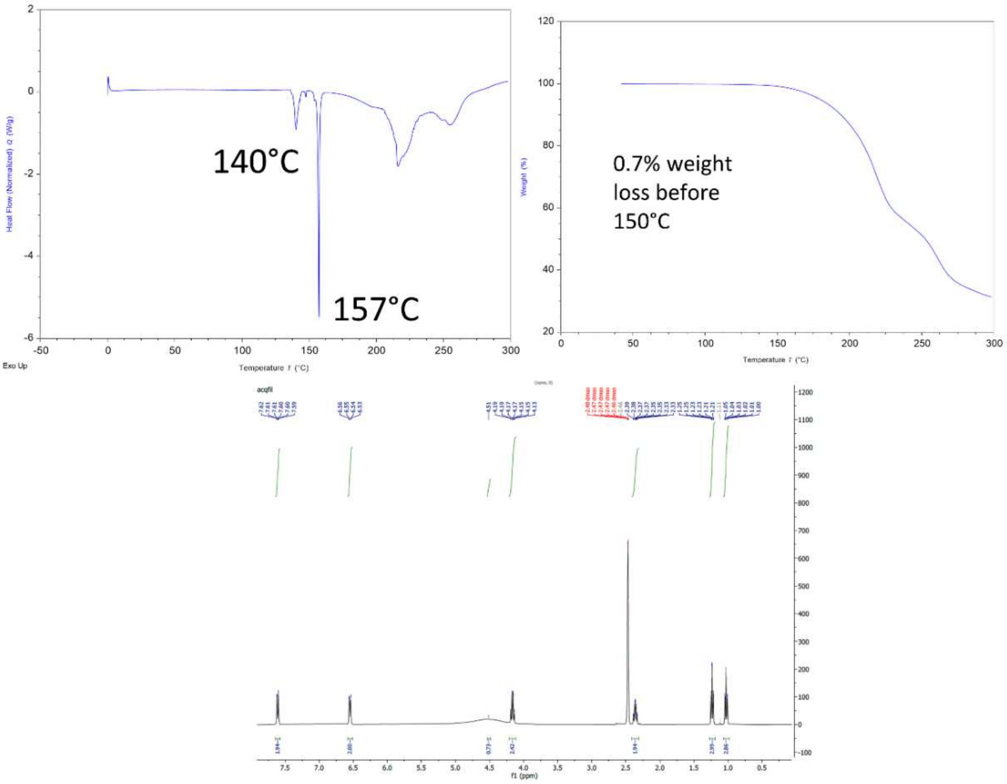

FIGURE S12. *DSC and TGA thermograms of BME and BE, paired with the NMR spectra respectively.*

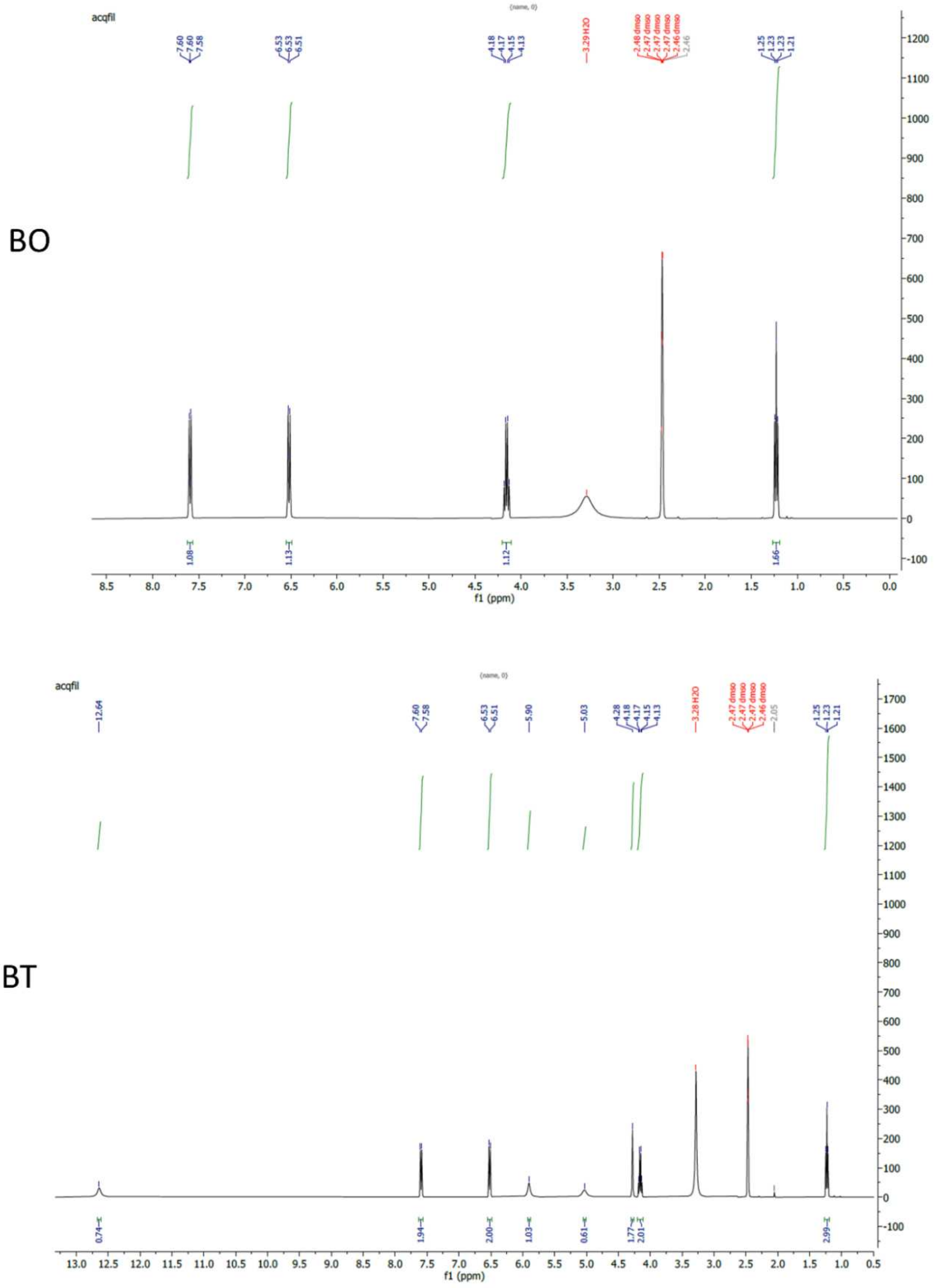

FIGURE S13. *NMR spectra of BO and BT.*

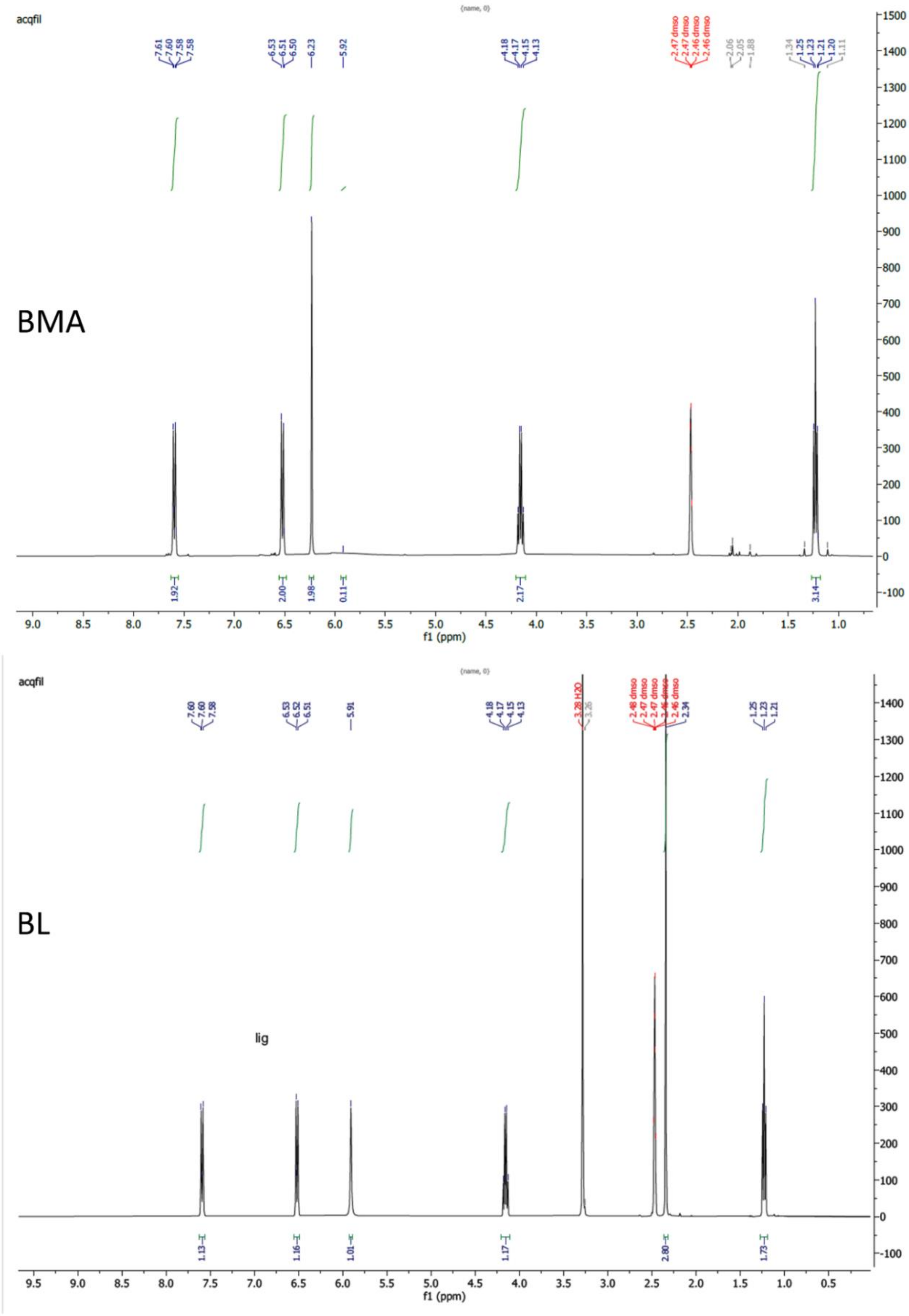

FIGURE S14. *NMR spectra of BMA and BL.*

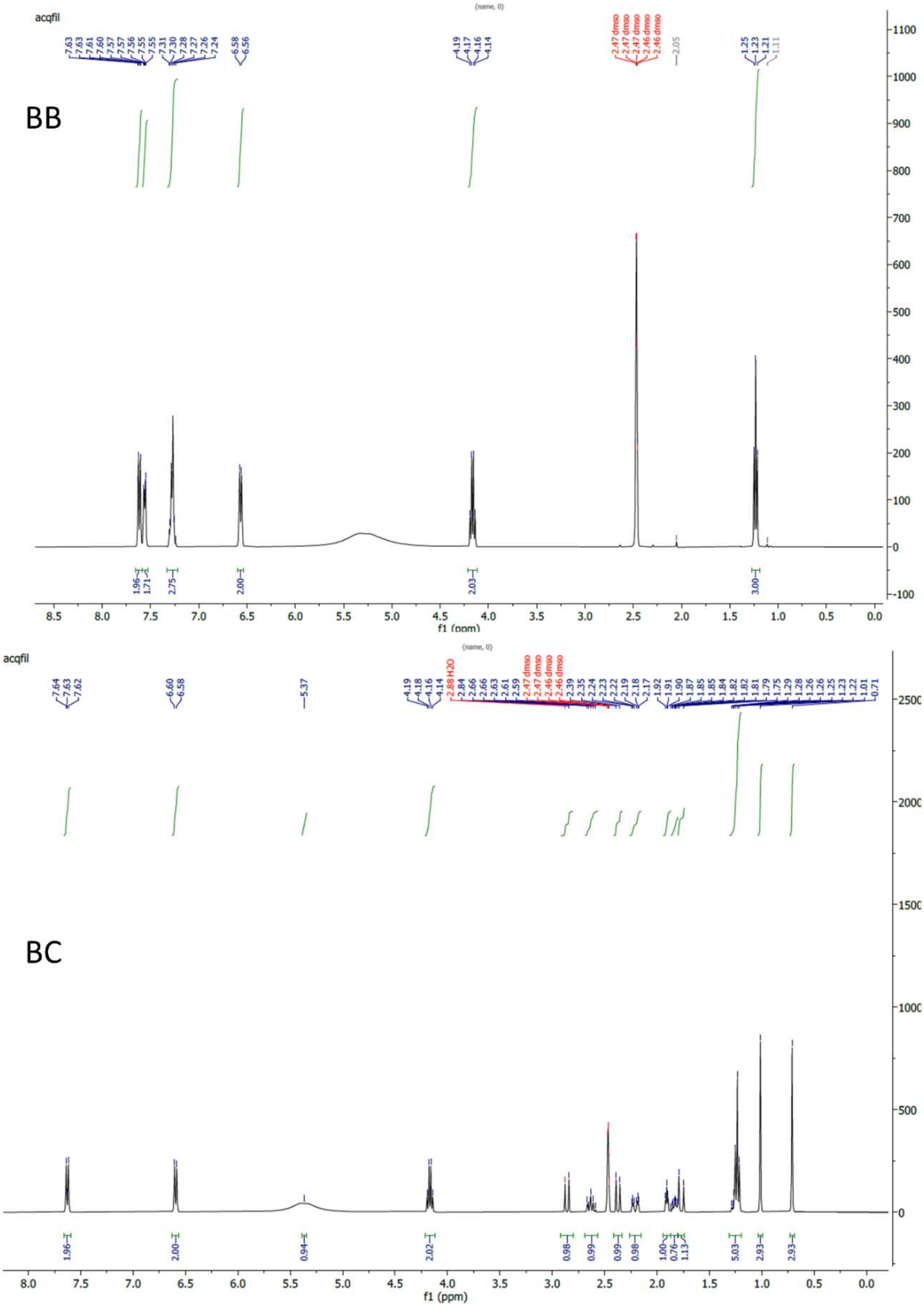

FIGURE S15. *NMR spectra of BB and BC.*

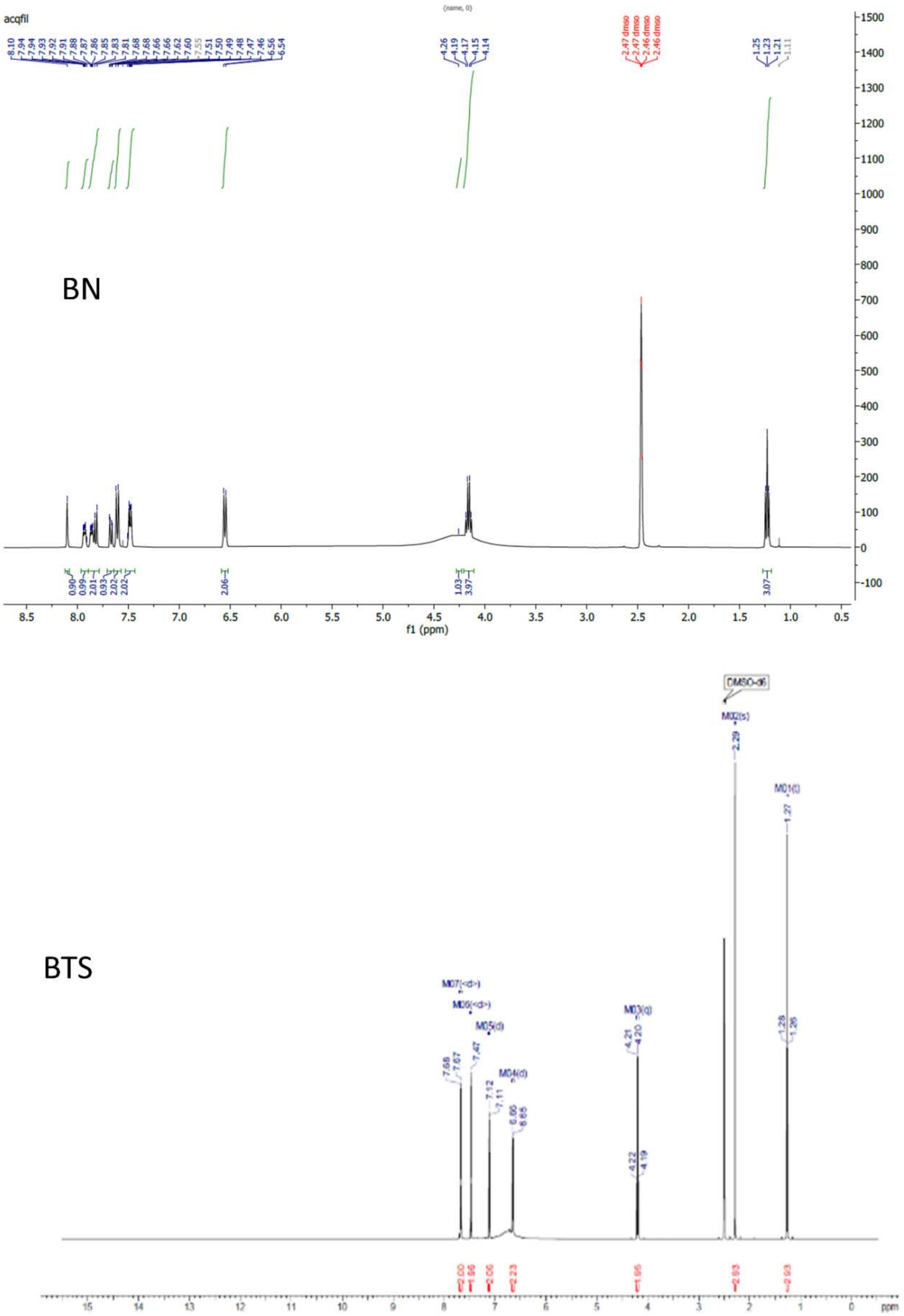

FIGURE S16. NMR spectra of BN and BTS.

	P_{app} 1 ***(*10^{-4} cm*s^{-1})***	***P_{app} 2*** ***(*10^{-4} cm*s^{-1})***	***P_{app} 3*** ***(*10^{-4} cm*s^{-1})***	*Mean* *(*10-4 cm*s-1)*	***SD%***
Benzocaine	***0.17***	***0.23***	***0.26***	***0.22***	***18.7***
Benzocaine maleate	*0.29*	*0.62*	*0.53*	*0.48*	*29.4*
Benzocaine mesylate	*0.54*	*0.50*	*0.54*	*0.52*	*3.7*
Benzocaine oxalate	*0.55*	*0.47*	*0.63*	*0.55*	*11.7*
Benzocaine esylate	*0.60*	*0.46*	*0.73*	*0.60*	*18.8*
Benzocaine tartrate	*0.30*	*0.54*	*1.14*	*0.66*	*53.5*
Benzocaine ligustrazine	*0.66*	*0.71*	*0.66*	*0.68*	*3.8*
Benzocaine naphtalensulfonate	*1.01*	*0.67*	*1.10*	*0.93*	*19.6*
Benzocaine besylate	*0.95*	*1.01*	*1.20*	*1.05*	*10.2*
Benzocaine tosylate	*1.03*	*1.17*	*1.10*	*1.10*	*5.1*
Benzocaine camphorsulfonate	*1.62*	*1.81*	*1.15*	*1.53*	*18.4*

TABLE S4. *Apparent permeability: 3 repetitions for every system, including benzocaine. SD% is reported in the last column.*

Chapter 5

5. Phasor-FLIM-guided unraveling of ATRA supramolecular organization in liposomal nanoformulations.

This project was made in collaboration with the Laboratorio NEST, Scuola Normale Superiore, Pisa, Italy and the Adolphe Merkle Institute, Fribourg, Switzerland.

5.1. Introduction

Retinoids belong to the polyisoprenol family and share structural similarities with vitamin A,[175] also known as retinol. Their involvement encompasses the regulation of cellular proliferation and differentiation, bolstering immune functionality, fostering bone tissue growth, and influencing the expression of tumor-suppressor genes.[176,177] Consequently, they are garnering escalating attention as plausible therapeutic agents for addressing diverse dermatological diseases, including skin cancers, inflammatory skin conditions, photoaging, psoriasis, and acne.[178–180] However, the utility of retinoids has encountered a hurdle due to their heightened susceptibility, particularly when subjected to oxygen, acidic settings, and light.[175] To surmount this issue, an array of methods have been devised to encapsulate retinoids. One such approach involves the intricate binding of retinoic acid (RA) with proteins, films, liposomes, micelles, as well as inorganic and polymeric nanoparticles.[181–183] The protection of retinoids from external influences has yielded promising outcomes, demonstrating efficacy in treating a spectrum of illnesses, including cancer.[183–185]

Despite the advances made in both laboratory and real-world applications, there remains a lack of information regarding the inherent characteristics of encapsulated retinoids in terms of their physical state. Considering this, a recently patented[186] and validated[187] methodology is employed herein. This technique leverages Fluorescence Lifetime Imaging Microscopy (FLIM) to delve into the supramolecular arrangement of ATRA (all-trans retinoic acid) encapsulated within nanostructures made of phosphatidylcholine (PC), cholesterol, and DSPE-PEG2000. Harnessing the intrinsic fluorescence of ATRA as a signal source, a fit-free analytical method involving phasor transformation is executed to dissect the lifetime data. Succinctly, each pixel in the image corresponds to a point on a "phasor plot." The distribution of these points, arising from FLIM measurements, manifests on a universal circle for single-exponential decays or within the circle for multi-exponential decays. The law of phasor addition, originally formulated by Gregorio Weber,[188] aids in pinpointing the origin of points within the phasor plot. To illustrate briefly: when two molecular species coexist within a pixel, the various potential weighting combinations of these species generate phasors that align along a straight line linking the distinctive phasors of the two pure species. In scenarios involving three molecular species, the conceivable configurations of the system form a triangle, with the vertices once again corresponding to the characteristic phasors of the pure species, and so forth. Therefore, when presented with an experimental phasor representing a fusion of two (or more) species, alongside the phasors of the isolated, unmixed components, a graphical solution can be derived, as previously described by others.[187,189,190]

nDSC and SAXS analyses have also been carried out to support the FLIM outcomes regarding the interactions between ATRA and the lipids in the formulations. The 'beating waves approach' reported in Chapter 4 is utilized to analyze SAXS data of ATRA liposomes. Indeed, this serves as a further proof of concept, highlighting the robustness and applicability of the method.

5.2. Materials and Methods

5.2.1. Liposome preparation

Encapsulation of all-trans retinoic acid (ATRA) was accomplished through diverse delivery systems employing distinct manufacturing techniques.

Neutral and positively charged liposomes were generated using the Thin Layer Evaporation (TLE) method. In detail, neutral liposome ATRA 1 was prepared by dissolving ATRA:PC:Cholesterol:DSPE-PEG2000 (in a molar ratio of 8:70:30:4) in 10 mL ethanol and subjecting it to vacuum rotary evaporation. Hydration with PBS at pH 7.4 ensued after lipid film formation. Similarly, liposome ATRA 2 was fashioned under the same conditions by mixing ATRA:PC:Cholesterol:DOTAP (in a molar ratio of 10:70:20:20) to yield positively charged liposomes. Both liposomal variants underwent extrusion at 800nm via a handheld extruder, ensuring attainment of desired particle size uniformity.

Across all formulations, complete encapsulation of ATRA was ensured, with no observation of crystal presence (TABLE S1).

5.2.2. Small Angle X-Ray Scattering (SAXS)

Investigations involving Small Angle X-Ray Scattering (SAXS) were conducted at Chiesi Farmaceutici S.p.A., Parma, Italy. Employing a Malvern PANalytical Empyrean X-ray diffraction/scattering instrument equipped with ScatterX78, the sealed high-resolution X-ray tube (Cu anode) operated at 40 kV and 40 mA. Cu Kα radiation (λCu Kα = 1.5418 Å) was collimated, and data were collected for 1 hour using a PIXcel3D-Medipix3 1x1 detector. Scattering vector $q = (4\ \pi/\lambda)\ \sin\Theta$, calibrated before analysis, was in play. PANalytical Data Collector software facilitated data collection, spanning a q-interval of 0.006-0.3 Å-1, and measurements were conducted at 25°C.

The acquired spectra underwent reduction and analysis through custom-made Wolfram Language (Mathematica, Version 13.0) scripts. Background subtraction (PBS buffer) and data editing were executed to refine the dataset, encompassing the q-range of 0.06-2.5 nm-1. Subsequent analysis followed the approach well described in the previous Chapter 4 to estimate the electron density profile of liposome bilayers. The bilayer's center was set as the profile center, accounting for its asymmetry. This methodology was applied to both unloaded and ATRA-loaded liposomes for comparison.

5.2.3. Nano Differential Scanning Calorimetry (nDSC)

Utilizing a Nano-Differential Scanning Calorimetry (nDSC) instrument from Ta-Instruments, heating experiments spanned 0°C to 95°C at a scan rate of 2°C/min, with 600 seconds of equilibration at the initial temperature. Buffer-filled cells facilitated blank scans before and after each sample.

Baseline scans using buffer in both sample and reference cells preceded the assessment of each sample, followed by baseline subtraction. Deconvolution of the thermograms using NanoAnalyze software, incorporating three Voigt models, yielded precise curve fitting (RMSE < 0.002). Key parameters encompassed transition temperature (T_m), enthalpy variation (ΔH), and peak half-width ($\Delta T_{m1/2}$). Cooperative number (CN) computation (following Kasian et al.'s method)[191] stemmed from these parameters.

$$CN = 4RTm2 \,/\, \Delta Tm1/2 \; \Delta H$$

5.2.4. Fluorescence Lifetime Imaging Microscopy (FLIM)

Fluorescence Lifetime Imaging Microscopy (FLIM) was executed using a Leica TCS SP5 confocal microscope. Samples encountered pulsed diode laser stimulation (400 nm excitation wavelength, 80 MHz frequency, 10-20 μW average power). Emission ranging from 470 to 570 nm was detected by a photomultiplier tube coupled to a PicoHarp 300 Time Correlated Single Photon Counting (TCSPC) card.

Custom Python 3.6 routines facilitated Phasor Analysis of FLIM data. For each pixel, time-domain fluorescence decay was transformed into the phasor plot. A phasor, denoted by real and imaginary coordinates, was formed based on Fourier Transform of fluorescence lifetime decay at the measurement's angular repetition frequency.

In frequency domain for each pixel one can exploit modulation $m_{i,j}$ and phase shift $\phi_{\mathrm{i,j}}$ of the signal to map the phasor plot as reported in eq.1 and 2.

$$1)\ g_{\{i,j\}} = m_{i,j} \cdot \cos\left(\phi_{\mathrm{i,j}}\right)$$

$$2)\ s_{\{i,j\}} = m_{i,j} \cdot \sin\left(\phi_{\mathrm{i,j}}\right)$$

Thus, pixels with similar decay curves will have similar coordinates in the phasor plot; therefore, pixels having a combination of two (or more) distinct lifetime decays will be mapped according to the weighted linear combination of these contributions. In other words, the presence of two or more molecular species generated phasors along a line connecting unique phasors of pure species. A graphical approach, as outlined by Tentori et al.,[187] facilitated the determination of contributing species from experimental phasors and isolated pure component phasors.

Mono-exponential decay employed equation 3, whereas multi-exponential decay used equation 4, with "f," "b," and "p" denoting free form, membrane-associated form, and precipitate form of the drug, respectively.

$$3)\ I_{mono}(t) = A_f e^{-t/\tau_p}$$

$$4)\ I_{multi}(t) = A_f e^{-t/\tau_f} + A_b e^{-t/\tau_b} + A_p e^{-t/\tau_p}$$

Phasors exhibited characteristics within a semi-circle – “the universal semi-circle”. Mono-exponentially decaying species mapped on the semi-circle, while species outside likely reflected delays in excited state reactions.[192]

5.2.5. Measurement Uncertainties

Final measurements' uncertainties were grounded in standard deviation of a single measurement. It's important to acknowledge that potential systematic errors could be present due to simplifying assumptions made during analysis. For instance, the assumption of uniform light interaction with the fluorophore across physical states of the drug could introduce errors.

5.3. Results

5.3.1. FLIM analysis of Lipo ATRA 1

Our investigation began by evaluating the lifetimes of the two pure species, contained in the fabricated formulation: ATRA in its precipitated state and ATRA dissolved in a DMSO solution (as depicted in FIGURE 5.1 A-B).

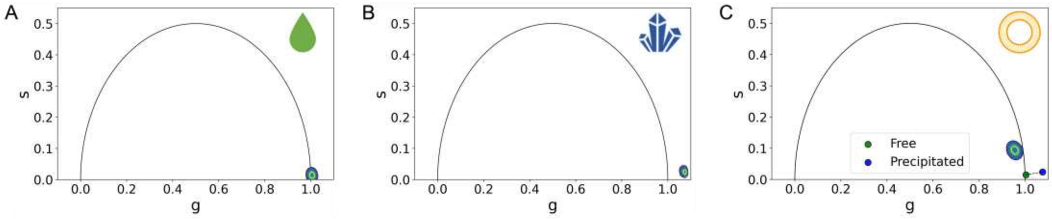

FIGURE 5. 1 *A) Lifetime phasor of free ATRA. B) Lifetime phasor of precipitated ATRA C) Lifetime phasors of liposomal nano formulations Lipo ATRA 1. (N=3).*

Evidently, both pure species exhibited short characteristic lifetime values, aligning near the lower-right quadrant of the universal semi-circle. It's noteworthy that in FIGURE 5.1C, the lifetime of precipitated ATRA extended beyond the boundaries of the universal circle, possibly attributed to the presence of excimers within the powder state. This observation raises speculation that a prolonged characteristic lifetime might arise from a supramolecular arrangement impeding the rapid relaxation of ATRA's excited state, contrasting with its behavior in solution or precipitated form. A parallel can be drawn to analogous conditions encountered with other nanoencapsulated drugs, where extended lifetimes were noted.[187,189] However, it's imperative to underscore that the FLIM-based identification of such a drug-liposome membrane interaction requires external validation.

5.3.2. SAXS Investigation of Lipo ATRA 1 and placebo

In pursuit of confirmation, Small Angle X-Ray Scattering (SAXS) emerged as a tool to semi-quantitatively probe the proximity of the drug to the lipid bilayer of Lipo ATRA. The process entailed custom-made codes to curate and dissect the acquired spectra (Chapter 4.2). Background subtraction (PBS buffer) and selective removal of the noisy q-range, restricting the scope to 0.06-2.5 nm-1, constituted data refinement. Subsequent analysis aimed to estimate the electron density profile of the liposome's bilayer. This asymmetrical bilayer, with its head-tail-tail-head center, was focal in the analysis. Both unloaded and drug-loaded liposome samples underwent this procedure.

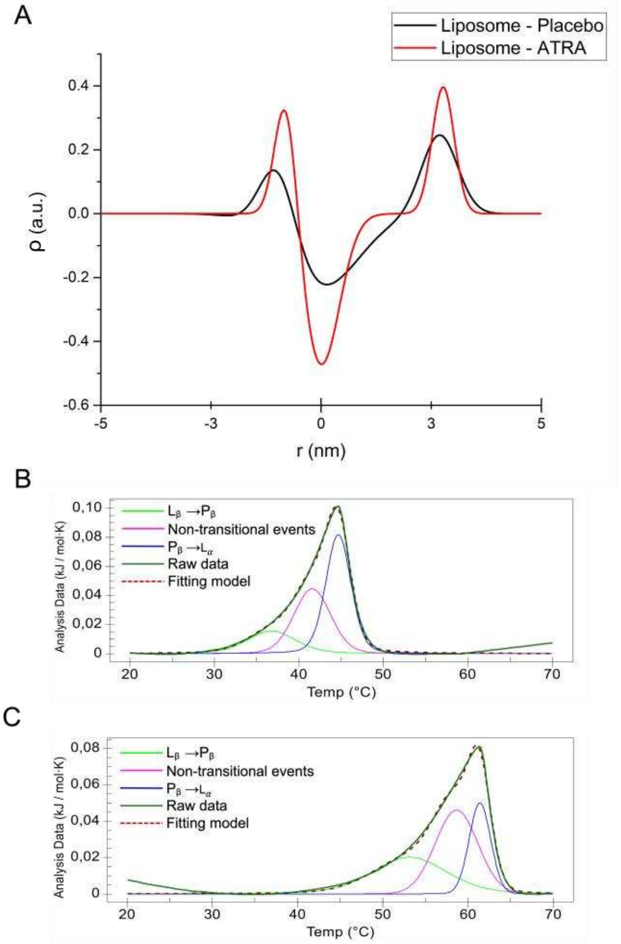

FIGURE 5. 2 *A) Electron density profile of the bilayer of placebo liposomes (black line) and Lipo ATRA 1 (red line). B) Deconvoluted thermogram of the placebo liposomes. C) Deconvoluted thermogram of ATRA-loaded liposomes (Lipo ATRA 1).*

Comparative evaluation between the two samples, as depicted in FIGURE 5.2A (Raw fit detailed in Chapter 5.3 - FIGURE S1), exposed discernible distinctions. The bilayer's electron density profile was expressed in terms of real distance (nm) and the difference obtained by subtracting the electron density of the buffer from the one of the bilayer (ρ). The bilayer's width, approximately 5 nm, was indicative of its thickness. Variations in Gaussian amplitudes illuminated the contrast between the lipid layer and the surrounding medium (PBS buffer). Phospholipid heads, notably richer compared to the water-based medium, manifested as positive Gaussian amplitudes. Conversely, electron density differences within the tails, comprising aliphatic chains, yielded a negative Gaussian amplitude upon subtracting medium electron density. Remarkably, the liposome loaded with ATRA exhibited heightened electron-density contrast in both phospholipid head and tail regions.

This compellingly suggests that upon encapsulation, a considerable portion of ATRA becomes integrated into the phospholipid bilayer. Drawing on SAXS data, we can tentatively deduce the plausible orientation of ATRA within the membrane. Given that ATRA features a hydrophilic carboxylic-acid group on one side and a hydrophobic component on the opposite side of its molecular structure, it's reasonable to postulate that ATRA aligns itself with the carboxylic residue facing the hydrophilic phospholipid heads, while the hydrophobic part interfaces with the lipid tails. This supposition aligns with the fact that the electron-rich carboxylic head likely contributes to enhanced contrast in the outer Gaussians, while the comparatively electron-sparse aliphatic moiety might underlie the increased negative contrast in the inner Gaussian, probably due to the disruption of the lipids in the bilayer after encapsulation.

5.3.3. NanoDSC analysis of Lipo ATRA and placebo

To validate this proposition, we conducted differential scanning calorimetry experiments (NanoDSC). As liposomes underwent heating, endothermic events appeared in the thermogram. These events corresponded to non-covalent processes, potentially indicating changes in alkyl chain packaging. Temperature-induced phase transitions were observed in the liposomes, highlighting their capacity to form a phospholipid bilayer akin to lyotropic liquid crystals, characterized by mesomorphic phase shifts across different liquid crystalline phases: the "gel phase" or low-temperature L_β phase contrasted with the "liquid-crystal phase" or high-temperature L_α phase (often termed "gel to liquid-crystalline transition").[191] An intermediary phase, the P_β or "rippled" phase, was identifiable by the undulating L_β-phase bilayers, coupled with a certain decline in liquid crystalline order.[193–195] The transition from P_β to L_α constituted the pre-transition, while the dominant transition marked the transition into the liquid phase.[196,197] Notably, distinct phospholipids exhibited varying transition temperatures (T_m).

Four samples were evaluated: PC, PC with ATRA, placebo formulation, and Lipo ATRA. All these preparations were established in PBS buffer. As illustrated in FIGURE 5.2B-C, three curves beneath each peak pointed toward three distinct processes during the heating of the liposomal formulation. The first and third events correlated with the liposome's pre-transition and primary transition, respectively. The second event could be attributed to a crack phase[198,199] or could be associated with the lamellarity or the varying size within the liposomal population.[200] Notably, the three events exhibited distinct Full Width at Half Maximum (FWHM), corresponding to $\Delta T_{m1/2}$ of each peak, indicating differing degrees of cooperativity. The primary transition emerged as the most cooperative.

Pairs of different formulations were compared for insights into how the behavior of PC transition changed in the presence of diverse components added to the formulation. Incorporating excipients or active agents often led to reduced intensity, broader peaks, decreased T_m, and diminished ΔH (enthalpy change), suggesting heightened membrane disorder. The broadening of DSC peaks related to disruption in membrane structure, augmented packing disorder, and significant decline in phase transition cooperativity.[201]

Comparing PC versus placebo (PC:Cholesterol:DSPE-PEG2000) evidenced a considerable T_m decrease as anticipated. Slightly higher ΔH could be attributed to larger placebo dimensions, increased cooperativity number (CN), and reduced $\Delta T_{m1/2}$. Upon comparing formulations with and without active agents, the addition of ATRA resulted in more consistent behavior across all parameters except T_m. The comparison of PC versus PC+ATRA (Chapter 5.3 - FIGURE S2), followed by placebo versus LipoATRA, revealed lower ∆H, elevated $\Delta T_{m1/2}$, and reduced CN, as highlighted in Chapter 5.3 - TABLE S2. Notably, T_m exhibited an increase. This observation led to our hypothesis that due to ATRA's lipophilic nature, a robust hydrophobic interaction occurs between the active principle and the lipophilic components (alkyl chains) of the phospholipid bilayer. This interaction, while reducing cooperativity, enhances formulation stability and elevates T_m. Moreover, the T_m increment is more pronounced when ATRA is introduced to the placebo, suggesting that the presence of other components like cholesterol and DSPE-PEG favors the interaction between ATRA and PC within the formulation.

5.3.4. FLIM analysis of Lipo ATRA and Lipo ATRA 2

Reinforced by the corroborating validations from SAXS and NanoDSC, we revisited FLIM and expanded the screening to another liposomal ATRA formulation, namely Lipo ATRA 2, where DSPE-PEG2000 was substituted with DOTAP. FIGURE 5.3A highlights the wide spectrum of lifetimes encompassing the potential location of the ATRA-lipid interaction phasor on the phasor plot (illustrated in red). We delineated the semicircle's boundaries, a representation of potential phasor positions, encompassing free, precipitated, and membrane-bound ATRA's three distinct physical states.

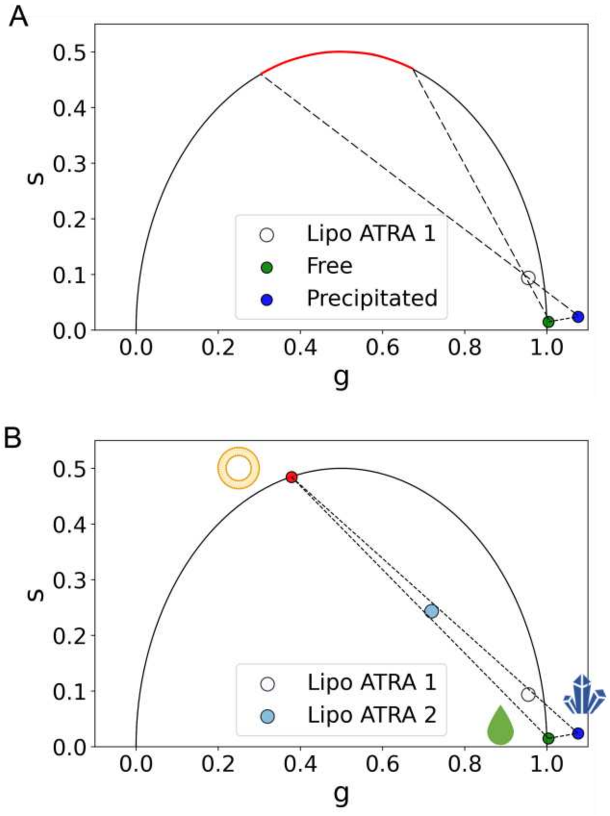

FIGURE 5. 3 *A) The red semicircle in the phasor plot highlights the area where the putative third species is expected to lie B) FLIM screening of liposomal formulations within ATRA reference phasor plot accounting for free-, precipitated-, and membrane-bound ATRA. (N=3)*

A noteworthy development emerged as we introduced Lipo ATRA 2 into our examination, effectively identifying the sole viable position for the phasor. This elucidation allowed us to precisely ascertain the fractional-intensity contribution of the membrane-bound physical state within Lipo ATRA (~10%) when interacting with Phosphatidylcholine (PC), revealing a truly remarkable interaction. As depicted in FIGURE 5.3B, the binding to PC is further intensified in the presence of both cholesterol (~28.3%) and DOTAP (~28.5%). The encapsulation of ATRA alongside DOTAP and Cholesterol, characteristic of Lipo ATRA 2, maximizes the fractional intensity of ATRA bound to membranes (~52.2%).

5.4. Conclusions

In summary, FLIM proved itself invaluable in shedding light on the presence of a supramolecular arrangement involving encapsulated ATRA interacting with lipids. This was achieved in a label-free mode, capitalizing on ATRA's intrinsic fluorescence. The validation of this outcome by SAXS and NanoDSC analyses underscores the effectiveness of FLIM analysis in elucidating the supramolecular structure of encapsulated fluorescent drugs.

Certainly, ATRA exhibited a notable affinity for the lipids present in the liposome's bilayer, displaying a distinctive alignment where its more hydrophobic segment oriented itself towards the hydrophobic tails of the phospholipids. Moreover, the application of FLIM demonstrated the significant influence of distinct lipids within the formulations in accentuating this interaction. Specifically, in Lipo ATRA 2, there was a heightened propensity for interaction between ATRA and PC thanks to DOTAP compared to the scenario in Lipo ATRA, where the interaction between ATRA and PC was comparatively less pronounced.

This study emphasizes the significance of harnessing advanced imaging techniques to deepen our comprehension of drug formulations and optimize their efficacy in various delivery applications.

5.5. Supporting Information

Nanoformulation	ATRA concentration [mg/mL]	Type	Excipients
Lipo ATRA	1	Liposome	PC Cholesterol DSPE-PEG2000
Lipo ATRA 2	4	Liposome	Pc Cholesterol DOTAP

TABLE S 1. *Investigated nanoformulations. Liposomal ATRA 1 is investigated in the whole paper and simply referred to as liposomal ATRA, while Liposomal ATRA 2 is included to evaluate the impact of distinct excipient formulation.*

Formulations	Tm [°C]	ΔH [kJ/mol]	CN	ΔTm ½
PC	51,23 ± 0,130	0,7089	616	8
PC + ATRA	56,6 ± 0,126	0,6796	529	10
Placebo	44,65 ± 0,038	0,7200	773	6
Lipo ATRA	61,39 ± 0,03	0,6763	731	7,5

TABLE S 2. *NanoDSC extrapolated data from DSC thermograms of various nanoformulations. in terms of melting temperature (Tm), enthalpy change (ΔH), cooperative number (CN) and Full Width Half Maximum ΔTm ½).*

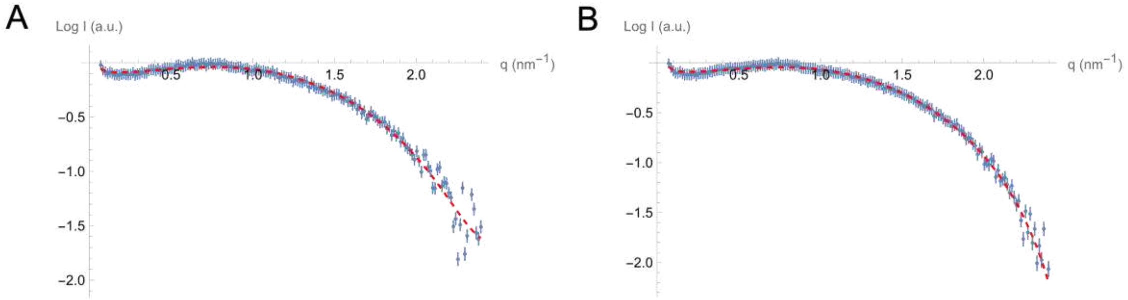

FIGURE S 1. *Raw fitting of the SAXS model A) Fitting of the liposome placebo SAXS pattern B) Fitting of the liposome loaded with ATRA SAXS pattern.*

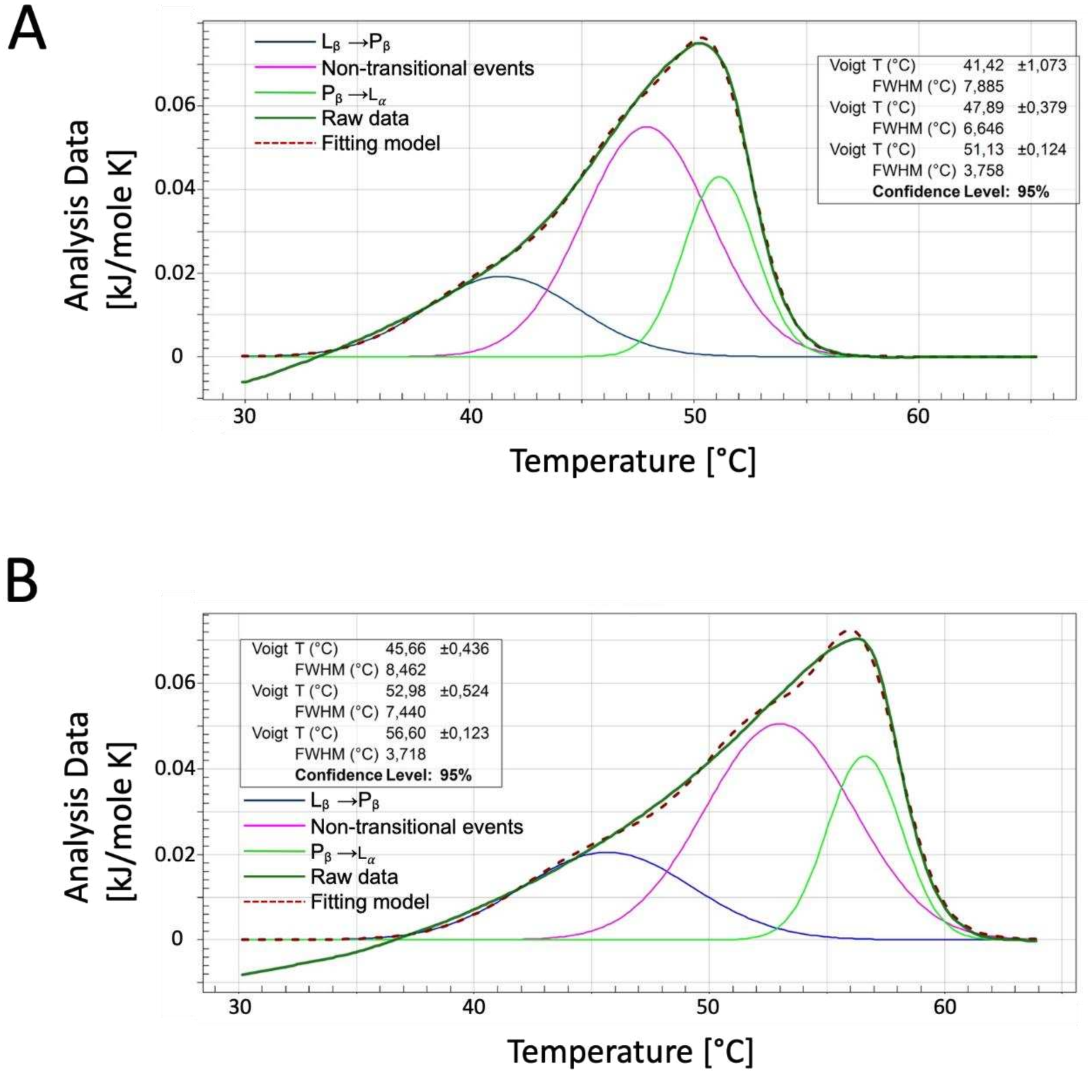

FIGURE S 2. *A) PC thermogram with voigt parameters of B) PC+ATRA thermograms with Voigt fitting parameters shows a clear shift towards higher melting temperature.*

Chapter 6

6. Conclusions and Outlooks.

In conclusion, this comprehensive thesis has traversed a diverse landscape of pharmaceutical research, each chapter contributing to the overarching goal of enhancing drug delivery properties. The studies presented herein encompass a range of innovative strategies, from chemical modifications to advanced characterization techniques, all aimed at optimizing drug formulations for better therapeutic outcomes.

The journey began with the salification of theophylline, demonstrating the power of crystal engineering modification in addressing the pharmacokinetic issue associated with the infamous narrow therapeutic window of this drug. By forming stable salt forms with squaric acid, we showcased how this approach can fine-tune drug properties like dissolution rate (reduced of around 50% in the first 10 minutes), laying the foundation for controlled drug release-like behavior — a theme that would resurface in subsequent chapters.

The third chapter dived into the world of cocrystallization, strategically altering the solubility, dissolution rates, and permeability of caffeine. In an effort to mitigate the “caffeine crash” phenomenon, we aimed to achieve a simulated sustained drug release to potentially maintain a stable blood concentration of caffeine, thereby avoiding a quick drop in vigilance soon after the administration. The cocrystals we developed offered a means of controlling drug release, providing a reduced solubility and dissolution rate, while guaranteeing an effective permeability (three-fold increase). Cocrystallization could indeed have a major role in the control of the blood concentration parameters without compromising any efficacy.

In the fourth chapter, we explored the potential of crystal engineering to enhance the properties of benzocaine. This step further solidified the link between crystal engineering and drug delivery, as we uncovered ways to improve the drug's dissolution rates and permeability, key factors in bioavailability, which is benzocaine’s soft spot.

Furthermore, inspired by the urgency of the COVID-19 pandemic, led us into the realm of liposomal formulations, where we specifically focused on benzocaine-loaded liposomes. We successfully encapsulated two newly synthetized salts within a lipid-based formulation and used Small Angle X-ray Scattering to assess the influence of the drug's physiochemical properties within a lipid environment. Indeed, benzocaine maleate salt could increase the liposome bilayer thickness compared to benzocaine alone. In order to address this, we introduced a novel approach for SAXS data analysis, simplifying a complex technique and making it accessible to a broader audience. This was a pivotal moment when crystal engineering and formulation engineering converged, underscoring the importance of precise characterization in liposomal drug delivery.

In the fifth chapter, the comparison among different techniques to assess the deep understanding of the relation between the drug and the lipid excipients is presented. SAXS as presented in the fourth chapter is tested along with Fluorescence Lifetime Imaging Microscopy (FLIM) and nanoDSC. Those techniques allowed us to fully understand the supramolecular arrangements of encapsulated drugs within liposomal formulations, adding a new layer of understanding to drug-lipid interactions and emphasizing the significance of advanced characterization techniques in optimizing drug delivery.

In essence, this thesis is a journey through the multidisciplinary landscape of pharmaceutical research. It underscores the interplay between chemical modification, crystal engineering, formulation engineering, and advanced characterization techniques in the pursuit of enhancing drug delivery properties. As we navigate the ever-evolving field of pharmaceutical science, the insights gained from these studies will undoubtedly shape the future of drug design and delivery, benefiting patients and advancing healthcare on a global scale.

In the context of future research and developments, several promising avenues emerge from the themes and connections highlighted in this thesis.

The integration of crystal engineering with formulation design stands out as a promising direction. The success demonstrated in enhancing drug properties through crystal engineering can be extended to explore a wider range of drug candidates. By leveraging cocrystals, researchers can exert precise control over drug release and bioavailability. This synergistic combination of crystal engineering and formulation design holds the potential to tailor drug delivery systems to meet specific therapeutic needs effectively.

Another critical aspect lies in the progress of advanced characterization techniques, a notable feature of this thesis. Simplified yet robust approaches introduced for techniques such as SAXS and FLIM open doors for broader adoption in pharmaceutical research. Future work can focus on refining and expanding the application of these methods to a wider array of drug formulations. Enhanced characterization techniques will empower researchers to gain deeper insights into drug-lipid interactions and optimize drug delivery systems with a higher degree of precision.

7. Bibliography

(1) Jain, K. K. An Overview of Drug Delivery Systems. In *Drug delivery systems*; 2020.

(2) Alqahtani, M. S.; Kazi, M.; Alsenaidy, M. A.; Ahmad, M. Z. Advances in Oral Drug Delivery. *Front Pharmacol* **2021**, *12* (February). https://doi.org/10.3389/fphar.2021.618411.

(3) Gulati, N.; Gupta, H. Parenteral Drug Delivery: A Review. *Recent Pat Drug Deliv Formul* **2011**, *5* (2), 133–145. https://doi.org/10.2174/187221111795471391.

(4) Prausnitz, M. R.; Langer, R. Transdermal Drug Delivery. *Nat Biotechnol* **2008**, *26* (11), 1261–1268. https://doi.org/10.1038/nbt.1504.

(5) Thakur, A. K.; Chellappan, D. K.; Dua, K.; Mehta, M.; Satija, S.; Singh, I. Patented Therapeutic Drug Delivery Strategies for Targeting Pulmonary Diseases. *Expert Opin Ther Pat* **2020**, *30* (5), 375–387. https://doi.org/10.1080/13543776.2020.1741547.

(6) Lipinski, C. A.; Lombardo, F.; Dominy, B. W.; Feeney, P. J. Experimental and Computational Approaches to Estimate Solubility and Permeability in Drug Discovery and Development Settings. *Adv Drug Deliv Rev* **2012**, *64* (SUPPL.), 4–17. https://doi.org/10.1016/j.addr.2012.09.019.

(7) Tyagi, M.; Begnini, F.; Poongavanam, V.; Doak, B. C.; Kihlberg, J. Drug Syntheses Beyond the Rule of 5. *Chemistry - A European Journal* **2020**, *26* (1), 49–88. https://doi.org/10.1002/chem.201902716.

(8) Rossi Sebastiano, M.; Doak, B. C.; Backlund, M.; Poongavanam, V.; Over, B.; Ermondi, G.; Caron, G.; Matsson, P.; Kihlberg, J. Impact of Dynamically Exposed Polarity on Permeability and Solubility of Chameleonic Drugs beyond the

Rule of 5. *J Med Chem* **2018**, *61* (9), 4189–4202. https://doi.org/10.1021/acs.jmedchem.8b00347.

(9) Fagerberg, J. H.; Tsinman, O.; Sun, N.; Tsinman, K.; Avdeef, A.; Bergström, C. A. S. Dissolution Rate and Apparent Solubility of Poorly Soluble Drugs in Biorelevant Dissolution Media. *Mol Pharm* **2010**, *7* (5), 1419–1430. https://doi.org/10.1021/mp100049m.

(10) Wang, J.; Skolnik, S. Permeability Diagnosis Model in Drug Discovery: A Diagnostic Tool to Identify the Most Influencing Properties for Gastrointestinal Permeability. *Curr Top Med Chem* **2013**, *13* (11), 1308–1316. https://doi.org/10.2174/15680266113139990035.

(11) Teksin, Z. S.; Seo, P. R.; Polli, J. E. Comparison of Drug Permeabilities and BCS Classification: Three Lipid-Component PAMPA System Method versus Caco-2 Monolayers. *AAPS Journal* **2010**, *12* (2), 238–241. https://doi.org/10.1208/s12248-010-9176-2.

(12) Li, L.; Yin, X. H.; Diao, K. S. Improving the Solubility and Bioavailability of Anti-Hepatitis B Drug PEC: Via PEC-Fumaric Acid Cocrystal. *RSC Adv* **2020**, *10* (59), 36125–36134. https://doi.org/10.1039/d0ra06608g.

(13) Savjani, K. T.; Gajjar, A. K.; Savjani, J. K. Drug Solubility: Importance and Enhancement Techniques. *ISRN Pharm* **2012**, *2012* (100 mL), 1–10. https://doi.org/10.5402/2012/195727.

(14) Wong, S. M.; Kellaway, I. W.; Murdan, S. Enhancement of the Dissolution Rate and Oral Absorption of a Poorly Water Soluble Drug by Formation of Surfactant-Containing Microparticles. *Int J Pharm* **2006**, *317* (1), 61–68. https://doi.org/10.1016/j.ijpharm.2006.03.001.

(15) Sathisaran, I.; Dalvi, S. V. Engineering Cocrystals of Poorlywater-Soluble Drugs to Enhance Dissolution in Aqueous Medium. *Pharmaceutics* **2018**, *10* (3). https://doi.org/10.3390/pharmaceutics10030108.

(16) Bennion, B. J.; Be, N. A.; McNerney, M. W.; Lao, V.; Carlson, E. M.; Valdez, C. A.; Malfatti, M. A.; Enright, H. A.; Nguyen, T. H.; Lightstone, F. C.; Carpenter, T. S. Predicting a Drug's Membrane Permeability: A Computational Model Validated with in Vitro Permeability Assay Data. *Journal of Physical Chemistry B* **2017**, *121* (20), 5228–5237. https://doi.org/10.1021/acs.jpcb.7b02914.

(17) Jacobsen, A. C.; Nielsen, S.; Brandl, M.; Bauer-Brandl, A. Drug Permeability Profiling Using the Novel Permeapad® 96-Well Plate. *Pharm Res* **2020**, *37* (6), 93. https://doi.org/10.1007/s11095-020-02807-x.

(18) Abet, V.; Filace, F.; Recio, J.; Alvarez-Builla, J.; Burgos, C. Prodrug Approach: An Overview of Recent Cases. *Eur J Med Chem* **2017**, *127*, 810–827. https://doi.org/10.1016/j.ejmech.2016.10.061.

(19) Desiraju, G. R. Crystal Engineering: The Design of Organic Solids. *Elsevier Science* **1989**, 312.

(20) Dunitz, J. D. Phase Transitions in Molecular Crystals from a Chemical Viewpoint. *Pure and Applied Chemistry* **1991**, *63* (2), 177–185. https://doi.org/10.1351/pac199163020177.

(21) Desiraju, G. R. Supramolecular Synthons in Crystal Engineering—A New Organic Synthesis. *Angewandte Chemie International Edition in English* **1995**, *34* (21), 2311–2327. https://doi.org/10.1002/anie.199523111.

(22) Braga, D.; Grepioni, F. Making Crystals by Design: Methods, Techniques and Applications. *Wiley* **2007**, 1–346. https://doi.org/10.1002/9783527610112.

(23) J.-M. Lehn. Supramolecular Chemistry-Scope and Perspectives Molecules, Supermolecules, and Molecular Devices (Nobel Lecture). *Angewandte Chemie International Edition in English* **1988**, *27* (1), 89–112.

(24) Zhang, Z.; Zaworotko, M. J. Template-Directed Synthesis of Metal-Organic Materials. *Chem Soc Rev* **2014**, *43* (16), 5444–5455. https://doi.org/10.1039/c4cs00075g.

(25) Corey, E. J. General Methods for the Construction of Complex Molecules. *Pure and Applied Chemistry* **1967**, *14* (1), 19–38. https://doi.org/10.1351/pac196714010019.

(26) Anslyn, Eric V.; Dougherty, D. A. *Modern Physical Organic Chemistry*; University Science Book, 2006.

(27) Steed, J. W. First- and Second-Sphere Coordination Chemistry of Alkali Metal Crown Ether Complexes. *Coord Chem Rev* **2001**, *215* (1), 171–221. https://doi.org/10.1016/S0010-8545(01)00317-4.

(28) Jeffrey, G. A. An Introduction to Hydrogen Bonding. *Oxford University Press* **1997**.

(29) Cavallo, G.; Metrangolo, P.; Milani, R.; Pilati, T.; Priimagi, A.; Resnati, G.; Terraneo, G. The Halogen Bond. *Chem Rev* **2016**, *116* (4), 2478–2601. https://doi.org/10.1021/acs.chemrev.5b00484.

(30) Desiraju, G. R.; Ho, P. S.; Kloo, L.; Legon, A. C.; Marquardt, R.; Metrangolo, P.; Politzer, P. A.; Resnati, G.; Rissanen, K.; State, S.; Unit, S. C.; State, C.; Collins, F.; Chimie, L. De. Definition of

the Halogen Bond. *IUPAC Provisional Recommendation* **2009**, 2–5.

(31) Martinez, C. R.; Iverson, B. L. Rethinking the Term “Pi-Stacking.” *Chem Sci* **2012**, *3* (7), 2191–2201. https://doi.org/10.1039/c2sc20045g.

(32) Hunter, Christopher A.; Lawson, Kevin R.; Perkins, Julie; Urch, C. J. Aromatic Interactions. *Journal of the Chemical Society, Perkin Transactions 2* **2001**.

(33) Grimme, S. Do Special Noncovalent π-π Stacking Interactions Really Exist? *Angewandte Chemie - International Edition* **2008**, *47* (18), 3430–3434. https://doi.org/10.1002/anie.200705157.

(34) Kitaigorodskii, A. I. Interpretative Study: Organic Chemical Crystallography. *Consultants Bureau, New York* **1961**.

(35) Duggirala, N. K.; Perry, M. L.; Almarsson, Ö.; Zaworotko, M. J. Pharmaceutical Cocrystals: Along the Path to Improved Medicines. *Chemical Communications* **2016**, *52* (4), 640–655. https://doi.org/10.1039/c5cc08216a.

(36) Golob, S.; Perry, M.; Lusi, M.; Chierotti, M. R.; Grabnar, I.; Lassiani, L.; Voinovich, D.; Zaworotko, M. J. Improving Biopharmaceutical Properties of Vinpocetine Through Cocrystallization. *J Pharm Sci* **2016**, *105* (12), 3626–3633. https://doi.org/10.1016/j.xphs.2016.09.017.

(37) Gupta, D.; Bhatia, D.; Dave, V.; Sutariya, V.; Gupta, S. V. Salts of Therapeutic Agents: Chemical, Physicochemical, and Biological Considerations. *Molecules* **2018**, *23* (7), 1–15. https://doi.org/10.3390/molecules23071719.

(38) Berry, D. J.; Steed, J. W. Pharmaceutical Cocrystals, Salts and Multicomponent Systems; Intermolecular Interactions and

Property Based Design. *Adv Drug Deliv Rev* **2017**, *117*, 3–24. https://doi.org/10.1016/j.addr.2017.03.003.

(39) Stahl, P. H. Chapter 7. A Procedure for Salt Selection and Optimization. In *Handbook of Pharmaceutical Salts: Properties, Selection, and Use*; 2002.

(40) Paulekuhn, G. S.; Dressman, J. B.; Saal, C. Trends in Active Pharmaceutical Ingredient Salt Selection Based on Analysis of the Orange Book Database. *J Med Chem* **2007**, *50* (26), 6665–6672. https://doi.org/10.1021/jm701032y.

(41) Prohotsky, D. L.; Zhao, F. A Survey of Top 200 Drugs-Inconsistent Practice of Drug Strength Expression for Drugs Containing Salt Forms. *J Pharm Sci* **2012**, *101* (1), 1–6. https://doi.org/10.1002/jps.22735.

(42) Brennan, Z. FDA to Reclassify Pharmaceutical Co-Crystals. *Regulatroy Affairs Professionals Society* **2016**.

(43) Gadade, D. D.; Pekamwar, S. S. Pharmaceutical Cocrystals: Regulatory and Strategic Aspects, Design and Development. *Adv Pharm Bull* **2016**, *6* (4), 479–494. https://doi.org/10.15171/apb.2016.062.

(44) Center of Drug Evaluation and Research. Guidance for Industry. Regulatory Classification of Pharmaceutical Co-Crystals. *Food and Drug Administration, U.S. Department of Health and Human Services* **2013**, 1–5.

(45) EMA. Reflection Paper on the Use of Cocrystals and Other Solid State Forms of Active Substances in Medicinal Products. *European Medical Agency* **2015**, *44* (May), 1–10.

(46) Stoler, E.; Warner, J. C. Non-Covalent Derivatives: Cocrystals and Eutectics. *Molecules* **2015**, *20* (8), 14833–14848. https://doi.org/10.3390/molecules200814833.

(47) Wöhler, F. Untersuchungen Über Das Chinon. *Justus Liebigs Ann Chem* **1844**, *51* (2), 145–163. https://doi.org/10.1002/jlac.18440510202.

(48) Version 5.34, ConQuest 1.11. *Cambridge Crystallographic Data Centre: Cambridge, UK*.

(49) Etter, M. C. Hydrogen Bonds as Design Elements in Organic Chemistry. *Journal of Physical Chemistry* **1991**, *95* (12), 4601–4610. https://doi.org/10.1021/j100165a007.

(50) Cherukuvada, S.; Guru Row, T. N. Comprehending the Formation of Eutectics and Cocrystals in Terms of Design and Their Structural Interrelationships. *Cryst Growth Des* **2014**, *14* (8), 4187–4198. https://doi.org/10.1021/cg500790q.

(51) Bevill, M. J.; Vlahova, P. I.; Smit, J. P. Polymorphic Cocrystals of Nutraceutical Compound p -Coumaric Acid with Nicotinamide: Characterization, Relative Solid-State Stability, and Conversion to Alternate Stoichiometries. *Cryst Growth Des* **2014**, *14* (3), 1438–1448. https://doi.org/10.1021/cg4019037.

(52) Barnes, P. J. Theophylline. *Am J Respir Crit Care Med* **2013**, *188* (8), 901–906. https://doi.org/10.1164/rccm.201302-0388PP.

(53) Focaroli, S.; Jiang, G.; O'connell, P.; Fahy, J. V.; Healy, A. M. The Use of a Three-Fluid Atomising Nozzle in the Production of Spray-Dried Theophylline/Salbutamol Sulphate Powders Intended for Pulmonary Delivery. *Pharmaceutics* **2020**, *12* (11), 1–18. https://doi.org/10.3390/pharmaceutics12111116.

(54) Barnes, P. J. Theophylline: New Perspectives for an Old Drug. *Am J Respir Crit Care Med* **2003**, *167* (6), 813–818. https://doi.org/10.1164/rccm.200210-1142PP.

(55) Wang, Y.; Wang, C. Z.; Lin, K. X.; Qian, G. S.; Zhuo, W. L.; Li, S. P.; Zhao, Z. Q.; Liao, X. Q.; Song, Y. X. Comparison of Inhaled Corticosteroid Combined with Theophylline and Double-Dose Inhaled Corticosteroid in Moderate to Severe Asthma. *Respirology* **2005**, *10* (2), 189–195. https://doi.org/10.1111/j.1440-1843.2005.00697.x.

(56) Svedmyr, K. Effects of Oral Theophylline Combined with Oral and Inhaled B2-Adrenostimulants in Asthmatics. *Allergy* **1982**, *37* (2), 119–127. https://doi.org/10.1111/j.1398-9995.1982.tb01885.x.

(57) Pezoa, R.; Gai, M. N.; Gutierrez, C.; Arancibia, A. Development of a Controlled-Release Theophylline Tablet: Evaluation in Vitro and in Vivo. *Anales de la Real Academia de Farmacia Instituto de Espana* **1992**, *58* (2), 269–283.

(58) Rodrigues, M.; Peiriço, N.; Matos, H.; Gomes De Azevedo, E.; Lobato, M. R.; Almeida, A. J. Microcomposites Theophylline/Hydrogenated Palm Oil from a PGSS Process for Controlled Drug Delivery Systems. *Journal of Supercritical Fluids* **2004**, *29* (1–2), 175–184. https://doi.org/10.1016/S0896-8446(03)00034-2.

(59) Jian, H.; Zhu, L.; Zhang, W.; Sun, D.; Jiang, J. Galactomannan (from Gleditsia Sinensis Lam.) and Xanthan Gum Matrix Tablets for Controlled Delivery of Theophylline: In Vitro Drug Release and Swelling Behavior. *Carbohydr Polym* **2012**, *87* (3), 2176–2182. https://doi.org/10.1016/j.carbpol.2011.10.043.

(60) Buhecha, M. D.; Lansley, A. B.; Somavarapu, S.; Pannala, A. S. Development and Characterization of PLA Nanoparticles for Pulmonary Drug Delivery: Co-Encapsulation of Theophylline and Budesonide, a Hydrophilic and Lipophilic Drug. *J Drug*

Deliv Sci Technol **2019**, *53* (November 2018), 101128. https://doi.org/10.1016/j.jddst.2019.101128.

(61) Hayashi, T.; Kanbe, H.; Okada, M.; Suzuki, M.; Ikeda, Y.; Onuki, Y.; Kaneko, T.; Sonobe, T. Formulation Study and Drug Release Mechanism of a New Theophylline Sustained-Release Preparation. *Int J Pharm* **2005**, *304* (1–2), 91–101. https://doi.org/10.1016/j.ijpharm.2005.07.022.

(62) Vranić, E. Basic Principles of Drug--Excipients Interactions. *Bosnian journal of basic medical sciences / Udruzenje basicnih mediciniskih znanosti = Association of Basic Medical Sciences* **2004**, *4* (2), 56–58. https://doi.org/10.17305/bjbms.2004.3421.

(63) West, R. History of the Oxocarbons. *Oxocarbons* **1980**, 1–14. https://doi.org/10.1016/b978-0-12-744580-9.50005-1.

(64) Horiuchi, S.; Tokunaga, Y.; Giovannetti, G.; Picozzi, S.; Itoh, H.; Shimano, R.; Kumai, R.; Tokura, Y. Above-Room-Temperature Ferroelectricity in a Single-Component Molecular Crystal. *Nature* **2010**, *463* (7282), 789–792. https://doi.org/10.1038/nature08731.

(65) Sreejith, S.; Carol, P.; Chithra, P.; Ajayaghosh, A. Squaraine Dyes: A Mine of Molecular Materials. *J Mater Chem* **2008**, *18* (3), 264–274. https://doi.org/10.1039/b707734c.

(66) Ajayaghosh, A. Chemistry of Squaraine-Derived Materials: Near-IR Dyes, Low Band Gap Systems, and Cation Sensors. *Acc Chem Res* **2005**, *38* (6), 449–459. https://doi.org/10.1021/ar0401000.

(67) Palli, M. A.; McTavish, H.; Kimball, A.; Horn, T. D. Immunotherapy of Recurrent Herpes Labialis with Squaric Acid. *JAMA Dermatol* **2017**, *153* (8), 828–829. https://doi.org/10.1001/jamadermatol.2017.0725.

(68) Chasák, J.; Šlachtová, V.; Urban, M.; Brulíková, L. Squaric Acid Analogues in Medicinal Chemistry. *Eur J Med Chem* **2021**, *209*. https://doi.org/10.1016/j.ejmech.2020.112872.

(69) Schwartz, L. M.; Howard, L. O. Aqueous Dissociation of Squaric Acid. *Journal of Physical Chemistry* **1970**, *74* (25), 4374–4377. https://doi.org/10.1021/j100719a013.

(70) Karle, I. L.; Ranganathan, D.; Haridas, V. A Persistent Preference for Layer Motifs in Self-Assemblies of Squarates and Hydrogen Squarates by Hydrogen Bonding [X-H···O; X = N, O, or C]: A Crystallographic Study of Five Organic Salts. *J Am Chem Soc* **1996**, *118* (30), 7128–7133. https://doi.org/10.1021/ja953167e.

(71) Bertolasi, V.; Gilli, P.; Ferretti, V.; Gilli, G. General Rules for the Packing of Hydrogen-Bonded Crystals as Derived from the Analysis of Squaric Acid Anions: Aminoaromatic Nitrogen Base Co-Crystals. *Acta Crystallogr B* **2001**, *57* (4), 591–598. https://doi.org/10.1107/S010876810100814X.

(72) Jurczak, E.; Mazurek, A. H.; Szeleszczuk, Ł.; Pisklak, D. M.; Zielińska-Pisklak, M. Pharmaceutical Hydrates Analysis—Overview of Methods and Recent Advances. *Pharmaceutics* **2020**, *12* (10), 1–25. https://doi.org/10.3390/pharmaceutics12100959.

(73) Censi, R.; Di Martino, P. Polymorph Impact on the Bioavailability and Stability of Poorly Soluble Drugs. *Molecules* **2015**, *20* (10), 18759–18776. https://doi.org/10.3390/molecules201018759.

(74) Buist, A. R.; Kennedy, A. R.; Manzie, C. Four Salt Phases of Theophylline. *Acta Crystallogr C Struct Chem* **2014**, *70* (2), 220–224. https://doi.org/10.1107/S2053229614000825.

(75) Stevens, J. S.; Byard, S. J.; Schroeder, S. L. M. Salt or Co-Crystal? Determination of Protonation State by X-Ray Photoelectron Spectroscopy (XPS). *J Pharm Sci* **2010**, *99* (11), 4453–4457. https://doi.org/10.1002/jps.22164.

(76) Mary Novena, L.; Suresh Kumar, S.; Athimoolam, S. Improved Solubility and Bioactivity of Theophylline (a Bronchodilator Drug) through Its New Nitrate Salt Analysed by Experimental and Theoretical Approaches. *J Mol Struct* **2016**, *1116*, 45–55. https://doi.org/10.1016/j.molstruc.2016.03.014.

(77) Sarma, B.; Saikia, B. Hydrogen Bond Synthon Competition in the Stabilization of Theophylline Cocrystals. *CrystEngComm* **2014**, *16* (22), 4753–4765. https://doi.org/10.1039/c3ce42332h.

(78) Sheldrick, G. M. SADABS-2008/1 - Bruker AXS Area Detector Scaling and Absorption Correction. *SADABS-2008/1 - Bruker AXS Area Detector Scaling and Absorption Correction Bruker AXS: Madison, Wisconsin, USA, 2008* **2008**.

(79) Sheldrick, G. M. SHELXT - Integrated Space-Group and Crystal-Structure Determination. *Acta Crystallogr A* **2015**, *71* (1), 3–8. https://doi.org/10.1107/S2053273314026370.

(80) Sheldrick, G. M. Crystal Structure Refinement with SHELXL. *Acta Crystallogr C Struct Chem* **2015**, *71*, 3–8. https://doi.org/10.1107/S2053229614024218.

(81) Dolomanov, O. V.; Bourhis, L. J.; Gildea, R. J.; Howard, J. A. K.; Puschmann, H. OLEX2: A Complete Structure Solution, Refinement and Analysis Program. *J Appl Crystallogr* **2009**, *42* (2), 339–341. https://doi.org/10.1107/S0021889808042726.

(82) Allen, F. H.; Cruz-Cabeza, A. J.; Wood, P. A.; Bardwell, D. A. Hydrogen-Bond Landscapes, Geometry and Energetics of Squaric Acid and Its Mono- and Dianions: A Cambridge

Structural Database, IsoStar and Computational Study. *Acta Crystallogr B Struct Sci Cryst Eng Mater* **2013**, *69* (5), 514–523. https://doi.org/10.1107/S2052519213020277.

(83) Fang, C.; Yang, P.; Liu, Y.; Wang, J.; Gao, Z.; Gong, J.; Rohani, S. Ultrasound-Assisted Theophylline Polymorphic Transformation: Selective Polymorph Nucleation, Molecular Mechanism and Kinetics Analysis. *Ultrason Sonochem* **2021**, *77*. https://doi.org/10.1016/j.ultsonch.2021.105675.

(84) M Yelanchezian, Y. M.; Waldvogel, H. J.; Faull, R. L. M.; Kwakowsky, A. Neuroprotective Effect of Caffeine in Alzheimer’s Disease. *Molecules* **2022**, *27* (12), 3737. https://doi.org/10.3390/molecules27123737.

(85) Fisone, G.; Borgkvist, A.; Usiello, A. Caffeine as a Psychomotor Stimulant: Mechanism of Action. *Cellular and Molecular Life Sciences*. April 2004, pp 857–872. https://doi.org/10.1007/s00018-003-3269-3.

(86) Tsume, Y.; Mudie, D. M.; Langguth, P.; Amidon, G. E.; Amidon, G. L. The Biopharmaceutics Classification System: Subclasses for in Vivo Predictive Dissolution (IPD) Methodology and IVIVC. *European Journal of Pharmaceutical Sciences* **2014**, *57* (1), 152–163. https://doi.org/10.1016/j.ejps.2014.01.009.

(87) Wagner-Hattler, L.; Schoelkopf, J.; Huwyler, J.; Puchkov, M. Stability Investigation of FCC-Based Tablets for Oral Suspension with Caffeine and Oxantel Pamoate as Model Drugs. *Drug Dev Ind Pharm* **2019**, *45* (2), 222–230. https://doi.org/10.1080/03639045.2018.1529784.

(88) Patat, A.; Rosenzweig, P.; Enslen, M.; Trocherie, S.; Miget, N.; Bozon, M. C.; Allain, H.; Gandon, J. M. Effects of a New Slow Release Formulation of Caffeine on EEG, Psychomotor and Cognitive Functions in Sleep-Deprived Subjects. *Hum*

Psychopharmacol **2000**, *15* (3), 153–170. https://doi.org/10.1002/(SICI)1099-1077(200004)15:3<153::AID-HUP154>3.0.CO;2-C.

(89) Malinauskas, B. M.; Aeby, V. G.; Overton, R. F.; Carpenter-Aeby, T.; Barber-Heidal, K. A Survey of Energy Drink Consumption Patterns among College Students. *Nutr J* **2007**, *6*. https://doi.org/10.1186/1475-2891-6-35.

(90) Lagarde, D.; Batejat, D.; Sicard, B.; Trocherie, S.; Chassard, D.; Enslen, M.; Chauffard, F. Slow-Release Caffeine: A New Response to the Effects of a Limited Sleep Deprivation. *Sleep* **2000**, *23* (5), 651–661. https://doi.org/10.1093/sleep/23.5.1h.

(91) Beaumont, M.; Batéjat, D.; Coste, O.; Doireau, P.; Chauffard, F.; Enslen, M.; Lagarde, D.; Pierard, C. Recovery after Prolonged Sleep Deprivation: Residual Effects of Slow-Release Caffeine on Recovery Sleep, Sleepiness and Cognitive Functions. *Neuropsychobiology* **2005**, *51* (1), 16–27. https://doi.org/10.1159/000082851.

(92) K, P. D.; D, R. D.; S, B.; B. Narayanan, V. H. In-Vivo Pharmacokinetic Studies of Dolutegravir Loaded Spray Dried Chitosan Nanoparticles as Milk Admixture for Paediatrics Infected with HIV. *Sci Rep* **2022**, *12* (1), 13907. https://doi.org/10.1038/s41598-022-18009-x.

(93) Elfadil, D.; Elkhatib, W. F.; El-Sayyad, G. S. Promising Advances in Nanobiotic-Based Formulations for Drug Specific Targeting against Multidrug Resistant Microbes and Biofilm-Associated Infections. *Microb Pathog* **2022**, 105721. https://doi.org/10.1016/j.micpath.2022.105721.

(94) Correia, A. C.; Monteiro, A. R.; Silva, R.; Moreira, J. N.; Sousa Lobo, J. M.; Silva, A. C. Lipid Nanoparticles Strategies to Modify Pharmacokinetics of Central Nervous System Targeting Drugs:

Crossing or Circumventing the Blood-Brain Barrier (BBB) to Manage Neurological Disorders. *Adv Drug Deliv Rev* **2022**, 114485. https://doi.org/10.1016/j.addr.2022.114485.

(95) Sainaga Jyothi, V. G. S.; Bulusu, R.; Venkata Krishna Rao, B.; Pranothi, M.; Banda, S.; Kumar Bolla, P.; Kommineni, N. Stability Characterization for Pharmaceutical Liposome Product Development with Focus on Regulatory Considerations: An Update. *Int J Pharm* **2022**, *624*, 122022. https://doi.org/10.1016/j.ijpharm.2022.122022.

(96) Ferreira, L.; Campos, J.; Veiga, F.; Cardoso, C.; Paiva-Santos, A. C. Cyclodextrin-Based Delivery Systems in Parenteral Formulations: A Critical Update Review. *European Journal of Pharmaceutics and Biopharmaceutics* **2022**, *178*, 35–52. https://doi.org/10.1016/j.ejpb.2022.07.007.

(97) Rodríguez-Spong, B.; Price, C. P.; Jayasankar, A.; Matzger, A. J.; Rodríguez-Hornedo, N. General Principles of Pharmaceutical Solid Polymorphism: A Supramolecular Perspective. *Adv Drug Deliv Rev* **2004**, *56* (3), 241–274. https://doi.org/10.1016/j.addr.2003.10.005.

(98) Rodriguez-Caabeiro, F.; Criado-Fomelio, A.; Jimenez-Gonzalez, A.; Guzman, L.; Igual, A.; Perez, A.; Pujol, M. Experimental Chemotherapy and Toxicity in Mice of Three Mebendazole Polymorphic Forms. *Chemotherapy* **1987**, *33* (4), 266–271. https://doi.org/10.1159/000238506.

(99) Narala, S.; Nyavanandi, D.; Alzahrani, A.; Bandari, S.; Zhang, F.; Repka, M. A. Creation of Hydrochlorothiazide Pharmaceutical Cocrystals Via Hot-Melt Extrusion for Enhanced Solubility and Permeability. *AAPS PharmSciTech* **2022**, *23* (1). https://doi.org/10.1208/s12249-021-02202-8.

(100) Ji, X.; Wu, D.; Li, C.; Li, J.; Sun, Q.; Chang, D.; Yin, Q.; Zhou, L.; Xie, C.; Gong, J.; Chen, W. Enhanced Solubility, Dissolution, and Permeability of Abacavir by Salt and Cocrystal Formation. *Cryst Growth Des* **2022**, *22* (1), 428–440. https://doi.org/10.1021/acs.cgd.1c01051.

(101) Li, L.; Pang, Z.; Ma, K.; Gao, Y.; Zheng, D.; Wei, Y.; Zhang, J.; Qian, S. Effect of Coformer Selection on In Vitro and In Vivo Performance of Adefovir Dipivoxil Cocrystals. *Pharm Res* **2021**, *38* (10), 1777–1791. https://doi.org/10.1007/s11095-021-03116-7.

(102) Aher, S.; Dhumal, R.; Mahadik, K.; Ketolainen, J.; Paradkar, A. Effect of Cocrystallization Techniques on Compressional Properties of Caffeine/Oxalic Acid 2:1 Cocrystal. *Pharm Dev Technol* **2013**, *18* (1), 55–60. https://doi.org/10.3109/10837450.2011.618950.

(103) Apshingekar, P. P.; Aher, S.; Kelly, A. L.; Brown, E. C.; Paradkar, A. Synthesis of Caffeine/Maleic Acid Co-Crystal by Ultrasound-Assisted Slurry Co-Crystallization. *J Pharm Sci* **2017**, *106* (1), 66–70. https://doi.org/10.1016/j.xphs.2016.09.009.

(104) Verma, P.; Srivastava, A.; Srivastava, K.; Tandon, P.; Shimpi, M. R. Molecular Structure, Spectral Investigations, Hydrogen Bonding Interactions and Reactivity-Property Relationship of Caffeine-Citric Acid Cocrystal by Experimental and DFT Approach. *Front Chem* **2021**, *9*. https://doi.org/10.3389/fchem.2021.708538.

(105) Sowa, M.;˥epokura, K.; Matczak-Jon, E. Solid-State Characterization and Solubility of a Genistein-Caffeine Cocrystal. *J Mol Struct* **2014**, *1076*, 80–88. https://doi.org/10.1016/j.molstruc.2014.07.036.

(106) Xia, Y.; Wei, Y.; Chen, H.; Qian, S.; Zhang, J.; Gao, Y. Competitive Cocrystallization and Its Application in the Separation of Flavonoids. *IUCrJ* **2021**, *8*, 195–207. https://doi.org/10.1107/S2052252520015997.

(107) Alsirawan, M. B.; Lai, X.; Prohens, R.; Vangala, V. R.; Pagire, S. K.; Shelley, P.; Bannan, T. J.; Topping, D. O.; Paradkar, A. Solid-State Competitive Destabilization of Caffeine Malonic Acid Cocrystal: Mechanistic and Kinetic Investigations. *Cryst Growth Des* **2020**, *20* (12), 7598–7605. https://doi.org/10.1021/acs.cgd.0c01246.

(108) Bučar, D. K.; Henry, R. F.; Lou, X.; Duerst, R. W.; Borchardt, T. B.; MacGillivray, L. R.; Zhang, G. G. Z. Co-Crystals of Caffeine and Hydroxy-2-Naphthoic Acids: Unusual Formation of the Carboxylic Acid Dimer in the Presence of a Heterosynthon. *Mol Pharm* **2007**, *4* (3), 339–346. https://doi.org/10.1021/mp070004b.

(109) Diez, S. J.; Eddleston, M. D.; Arhangelskis, M.; Milbled, M.; Müller, M. J.; Bond, A. D.; Bučar, D. K.; Jones, W. Crystallization at Solvent Interfaces Enables Access to a Variety of Cocrystal Polymorphs and Hydrates. *Cryst Growth Des* **2018**, *18* (6), 3263–3268. https://doi.org/10.1021/acs.cgd.8b00114.

(110) Stabrauskiene, J.; Kopustinskiene, D. M.; Lazauskas, R.; Bernatoniene, J. Naringin and Naringenin: Their Mechanisms of Action and the Potential Anticancer Activities. *Biomedicines* **2022**, *10* (7), 1686. https://doi.org/10.3390/biomedicines10071686.

(111) Cui, J.; Zong, W.; Zhao, N.; Yuan, R. Burdock (Arctium Lappa L.) Leaf Flavonoids Rich in Morin and Quercetin 3-O-Rhamnoside Ameliorate Lipopolysaccharide-Induced

Inflammation and Oxidative Stress in RAW264.7 Cells. *Food Sci Nutr* **2022**. https://doi.org/10.1002/fsn3.2875.

(112) Iwasaki, S.; Yamamoto, S.; Sano, N.; Tohyama, K.; Kosugi, Y.; Furuta, A.; Hamada, T.; Igari, T.; Fujioka, Y.; Hirabayashi, H.; Amano, N. Direct Drug Delivery of Low-Permeable Compounds to the Central Nervous System Via Intranasal Administration in Rats and Monkeys. *Pharm Res* **2019**, *36* (5). https://doi.org/10.1007/s11095-019-2613-8.

(113) Baraldi, L.; Fornasari, L.; Bassanetti, I.; Amadei, F.; Bacchi, A.; Marchiò, L. Salification Controls the In-Vitro Release of Theophylline. *Crystals (Basel)* **2022**, *12* (2). https://doi.org/10.3390/cryst12020201.

(114) Groom, C. R.; Bruno, I. J.; Lightfoot, M. P.; Ward, S. C. The Cambridge Structural Database. *Acta Crystallogr B Struct Sci Cryst Eng Mater* **2016**, *72* (2), 171–179. https://doi.org/10.1107/S2052520616003954.

(115) Tzanova, M. M.; Randelov, E.; Stein, P. C.; Hiorth, M.; di Cagno, M. P. Towards a Better Mechanistic Comprehension of Drug Permeation and Absorption: Introducing the Diffusion-Partitioning Interplay. *Int J Pharm* **2021**, *608*. https://doi.org/10.1016/j.ijpharm.2021.121116.

(116) Frisch, M. J. Gaussian˜16 {R}evision {C}.01. 2016.

(117) Grimme, S.; Antony, J.; Ehrlich, S.; Krieg, H. A Consistent and Accurate Ab Initio Parametrization of Density Functional Dispersion Correction (DFT-D) for the 94 Elements H-Pu. *Journal of Chemical Physics* **2010**, *132* (15). https://doi.org/10.1063/1.3382344.

(118) Petersson, G. A.; Bennett, A.; Tensfeldt, T. G.; Al-Laham, M. A.; Shirley, W. A.; Mantzaris, J. A Complete Basis Set Model Chemistry. I. The Total Energies of Closed-Shell Atoms and

Hydrides of the First-Row Elements. *J Chem Phys* **1988**, *89* (4), 2193–2218. https://doi.org/10.1063/1.455064.

(119) Weigend, F.; Ahlrichs, R. Balanced Basis Sets of Split Valence, Triple Zeta Valence and Quadruple Zeta Valence Quality for H to Rn: Design and Assessment of Accuracy. *Physical Chemistry Chemical Physics* **2005**, *7* (18), 3297–3305. https://doi.org/10.1039/b508541a.

(120) Mennucci, B.; Tomasi, J. Continuum Solvation Models: A New Approach to the Problem of Solute's Charge Distribution and Cavity Boundaries. *Journal of Chemical Physics* **1997**, *106* (12), 5151–5158. https://doi.org/10.1063/1.473558.

(121) Jin, G. Z.; Fujii, S.; Tomita, K. Structure of Naringin Hexahemihydrate. *Acta Crystallogr C* **1990**, *46* (10), 1866–1869. https://doi.org/10.1107/s0108270189013983.

(122) Sanphui, P.; Devi, V. K.; Clara, D.; Malviya, N.; Ganguly, S.; Desiraju, G. R. Cocrystals of Hydrochlorothiazide: Solubility and Diffusion/Permeability Enhancements through Drug-Coformer Interactions. *Mol Pharm* **2015**, *12* (5), 1615–1622. https://doi.org/10.1021/acs.molpharmaceut.5b00020.

(123) De Groot, C.; Müller-Goymann, C. C. Saponin Interactions with Model Membrane Systems - Langmuir Monolayer Studies, Hemolysis and Formation of ISCOMs. *Planta Med* **2016**, *82* (18), 1496–1512. https://doi.org/10.1055/s-0042-118387.

(124) Khair-ul-Bariyah, S.; Arshad, M.; Ali, M.; Din, M. I.; Sharif, A.; Ahmed, E. Benzocaine: Review on a Drug with Unfold Potential. *Mini-Reviews in Medicinal Chemistry* **2019**, *20* (1), 3–11. https://doi.org/10.2174/1389557519666190913145423.

(125) Lee, H.-S. Recent Advances in Topical Anesthesia. *J Dent Anesth Pain Med* **2016**, *16* (4), 237. https://doi.org/10.17245/jdapm.2016.16.4.237.

(126) De Araujo, D. R.; Padula, C.; Cereda, C. M. S.; Tófoli, G. R.; Brito, R. B.; De Paula, E.; Nicoli, S.; Santi, P. Bioadhesive Films Containing Benzocaine: Correlation between in Vitro Permeation and in Vivo Local Anesthetic Effect. *Pharm Res* **2010**, *27* (8), 1677–1686. https://doi.org/10.1007/s11095-010-0151-5.

(127) Paczkowska, M.; Wiergowska, G.; Miklaszewski, A.; Krause, A.; Mroczkowka, M.; Zalewski, P.; Cielecka-Piontek, J. The Analysis of the Physicochemical Properties of Benzocaine Polymorphs. *Molecules* **2018**, *23* (7). https://doi.org/10.3390/molecules23071737.

(128) Patyk-Kaźmierczak, E.; Kaźmierczak, M. A New High-Pressure Benzocaine Polymorph-towards Understanding the Molecular Aggregation in Crystals of an Important Active Pharmaceutical Ingredient (API). *Acta Crystallogr B Struct Sci Cryst Eng Mater* **2020**, *76*, 56–64. https://doi.org/10.1107/S2052520619016548.

(129) Polak, S.; Ghobadi, C.; Mishra, H.; Ahamadi, M.; Patel, N.; Jamei, M.; Rostami-Hodjegan, A. Prediction of Concentration-Time Profile and Its Inter-Individual Variability Following the Dermal Drug Absorption. *J Pharm Sci* **2012**, *101* (7), 2584–2595. https://doi.org/10.1002/jps.23155.

(130) Deng, J.; Zhu, X.; Chen, Z.; Fan, C. H.; Kwan, H. S.; Wong, C. H.; Shek, K. Y.; Zuo, Z.; Lam, T. N. A Review of Food–Drug Interactions on Oral Drug Absorption. *Drugs* **2017**, *77* (17), 1833–1855. https://doi.org/10.1007/s40265-017-0832-z.

(131) Üstündağ Okur, N.; Çağlar, E. Ş.; Arpa, M. D.; Karasulu, H. Y. Preparation and Evaluation of Novel Microemulsion-Based Hydrogels for Dermal Delivery of Benzocaine. *Pharm Dev Technol* **2017**, *22* (4), 500–510. https://doi.org/10.3109/10837450.2015.1131716.

(132) Puglia, C.; Sarpietro, M. G.; Bonina, F.; Castelli, F.; Zammataro, M.; Chiechio, S. Development, Characterization, and in Vitro and in Vivo Evaluation of Benzocaine- and Lidocaine-Loaded Nanostructrured Lipid Carriers. *J Pharm Sci* **2011**, *100* (5), 1892–1899. https://doi.org/10.1002/jps.22416.

(133) Gana, I.; Barrio, M.; Do, B.; Tamarit, J. L.; Céolin, R.; Rietveld, I. B. Benzocaine Polymorphism: Pressure-Temperature Phase Diagram Involving Forms II and III. *Int J Pharm* **2013**, *456* (2), 480–488. https://doi.org/10.1016/j.ijpharm.2013.08.031.

(134) Desiraju, G. R. Crystal Engineering: From Molecule to Crystal. *J Am Chem Soc* **2013**, *135* (27), 9952–9967. https://doi.org/10.1021/ja403264c.

(135) Nangia, A. K.; Desiraju, G. R. Crystal Engineering: An Outlook for the Future. *Angewandte Chemie - International Edition* **2019**, *58* (13), 4100–4107. https://doi.org/10.1002/anie.201811313.

(136) Ferreira, J. T.; Schoonbee, H. J.; Smit, G. L. The Use of Benzocaine-Hydrochloride as an Aid in the Transport of Fish. *Aquaculture* **1984**, *42* (2), 169–174. https://doi.org/10.1016/0044-8486(84)90364-8.

(137) Henck, J. O.; Bernstein, J.; Ellern, A.; Boese, R. Disappearing and Reappearing Polymorphs. The Benzocaine:Picric Acid System. *J Am Chem Soc* **2001**, *123* (9), 1834–1841. https://doi.org/10.1021/ja002113o.

(138) Sheldrick, G. M. SHELXT - Integrated Space-Group and Crystal-Structure Determination. *Acta Crystallogr A* **2015**, *71* (1), 3–8. https://doi.org/10.1107/S2053273314026370.

(139) B. A. I. Bruker, 2012.

(140) Macrae, C. F.; Edgington, P. R.; McCabe, P.; Pidcock, E.; Shields, G. P.; Taylor, R.; Towler, M.; Van De Streek, J. Mercury: Visualization and Analysis of Crystal Structures. *J Appl Crystallogr* **2006**, *39* (3), 453–457. https://doi.org/10.1107/S002188980600731X.

(141) Spackman, P. R.; Turner, M. J.; McKinnon, J. J.; Wolff, S. K.; Grimwood, D. J.; Jayatilaka, D.; Spackman, M. A. CrystalExplorer: A Program for Hirshfeld Surface Analysis, Visualization and Quantitative Analysis of Molecular Crystals. *J Appl Crystallogr* **2021**, *54*, 1006–1011. https://doi.org/10.1107/S1600576721002910.

(142) Hubatsch, I.; Ragnarsson, E. G. E.; Artursson, P. Determination of Drug Permeability and Prediction of Drug Absorption in Caco-2 Monolayers. *Nat Protoc* **2007**, *2* (9), 2111–2119. https://doi.org/10.1038/nprot.2007.303.

(143) Gupta, R.; Dwadasi, B. S.; Rai, B.; Mitragotri, S. Effect of Chemical Permeation Enhancers on Skin Permeability: In Silico Screening Using Molecular Dynamics Simulations. *Sci Rep* **2019**, *9* (1). https://doi.org/10.1038/s41598-018-37900-0.

(144) Edwards, A. M.; Baric, R. S.; Saphire, E. O.; Ulmer, J. B. *Stopping Pandemics before They Start: Lessons Learned from SARS-CoV-2*. https://covid19.trackvaccines.org/agency/who.

(145) Behl, A.; Nair, A.; Mohagaonkar, S.; Yadav, P.; Gambhir, K.; Tyagi, N.; Sharma, R. K.; Butola, B. S.; Sharma, N. Threat, Challenges, and Preparedness for Future Pandemics: A Descriptive Review of Phylogenetic Analysis Based Predictions. *Infection, Genetics and Evolution*. Elsevier B.V. March 1, 2022. https://doi.org/10.1016/j.meegid.2022.105217.

(146) Edelson, P. J.; Harold, R.; Ackelsberg, J.; Duchin, J. S.; Lawrence, S. J.; Manabe, Y. C.; Zahn, M.; LaRocque, R. C.

Climate Change and the Epidemiology of Infectious Diseases in the United States. *Clin Infect Dis* **2023**, *76* (5), 950–956. https://doi.org/10.1093/cid/ciac697.

(147) Liz-Marzán, L. M.; Nel, A. E.; Brinker, C. J.; Chan, W. C. W.; Chen, C.; Chen, X.; Ho, D.; Hu, T.; Kataoka, K.; Kotov, N. A.; Parak, W. J.; Stevens, M. M. What Do We Mean When We Say Nanomedicine? *ACS Nano*. American Chemical Society September 27, 2022, pp 13257–13259. https://doi.org/10.1021/acsnano.2c08675.

(148) Fan, Y.; Marioli, M.; Zhang, K. Analytical Characterization of Liposomes and Other Lipid Nanoparticles for Drug Delivery. *Journal of Pharmaceutical and Biomedical Analysis*. Elsevier B.V. January 5, 2021. https://doi.org/10.1016/j.jpba.2020.113642.

(149) Dimov, N.; Kastner, E.; Hussain, M.; Perrie, Y.; Szita, N. Formation and Purification of Tailored Liposomes for Drug Delivery Using a Module-Based Micro Continuous-Flow System. *Sci Rep* **2017**, *7* (1). https://doi.org/10.1038/s41598-017-11533-1.

(150) Bangham, A. D.; Standish, M. M.; Watkins, J. C. Diffusion of Univalent Ions across the Lamellae of Swollen Phospholipids. *J Mol Biol* **1965**, *13* (1), 238–252. https://doi.org/10.1016/S0022-2836(65)80093-6.

(151) Tenchov, R.; Bird, R.; Curtze, A. E.; Zhou, Q. Lipid Nanoparticles from Liposomes to MRNA Vaccine Delivery, a Landscape of Research Diversity and Advancement. *ACS Nano*. American Chemical Society November 23, 2021, pp 16982–17015. https://doi.org/10.1021/acsnano.1c04996.

(152) Gregoriadis, G.; Ryman, B. E. Fate of Protein-Containing Liposomes Injected into Rats: An Approach to the Treatment of

Storage Diseases. *Eur J Biochem* **1972**, *24* (3), 485–491. https://doi.org/10.1111/j.1432-1033.1972.tb19710.x.

(153) Large, D. E.; Abdelmessih, R. G.; Fink, E. A.; Auguste, D. T. Liposome Composition in Drug Delivery Design, Synthesis, Characterization, and Clinical Application. *Advanced Drug Delivery Reviews*. Elsevier B.V. September 1, 2021. https://doi.org/10.1016/j.addr.2021.113851.

(154) Sesarman, A.; Muntean, D.; Abrudan, B.; Tefas, L.; Sylvester, B.; Licarete, E.; Rauca, V.; Luput, L.; Patras, L.; Banciu, M.; Vlase, L.; Porfire, A. Improved Pharmacokinetics and Reduced Side Effects of Doxorubicin Therapy by Liposomal Co-Encapsulation with Curcumin. *J Liposome Res* **2021**, *31* (1), 1–10. https://doi.org/10.1080/08982104.2019.1682604.

(155) Kapoor, M.; Lee, S. L.; Tyner, K. M. Liposomal Drug Product Development and Quality: Current US Experience and Perspective. *AAPS Journal* **2017**, *19* (3), 632–641. https://doi.org/10.1208/s12248-017-0049-9.

(156) Lou, G.; Anderluzzi, G.; Schmidt, S. T.; Woods, S.; Gallorini, S.; Brazzoli, M.; Giusti, F.; Ferlenghi, I.; Johnson, R. N.; Roberts, C. W.; O’Hagan, D. T.; Baudner, B. C.; Perrie, Y. Delivery of Self-Amplifying MRNA Vaccines by Cationic Lipid Nanoparticles: The Impact of Cationic Lipid Selection. *Journal of Controlled Release* **2020**, *325*, 370–379. https://doi.org/10.1016/j.jconrel.2020.06.027.

(157) Gregoriadis, G. Liposomes and MRNA: Two Technologies Together Create a COVID-19 Vaccine. *Med Drug Discov* **2021**, *12*, 100104. https://doi.org/10.1016/j.medidd.2021.100104.

(158) Prakash K Soni, T. R. S. Purification of Drug Loaded Liposomal Formulations by a Novel Stirred Cell Ultrafiltration Technique. *Pharm Nanotechnol* **2021**, 347–360.

(159) Danaei, M.; Dehghankhold, M.; Ataei, S.; Hasanzadeh Davarani, F.; Javanmard, R.; Dokhani, A.; Khorasani, S.; Mozafari, M. R. Impact of Particle Size and Polydispersity Index on the Clinical Applications of Lipidic Nanocarrier Systems. *Pharmaceutics*. MDPI AG May 18, 2018. https://doi.org/10.3390/pharmaceutics10020057.

(160) Heberle, F. A.; Pabst, G. Complex Biomembrane Mimetics on the Sub-Nanometer Scale. *Biophysical Reviews*. Springer Verlag August 1, 2017, pp 353–373. https://doi.org/10.1007/s12551-017-0275-5.

(161) Dong, H.; Kim, J. S.; Chirikjian, G. S. Computational Analysis of SAXS Data Acquisition. *Journal of Computational Biology* **2015**, *22* (9), 787–805. https://doi.org/10.1089/cmb.2015.0115.

(162) Li, T.; Senesi, A. J.; Lee, B. Small Angle X-Ray Scattering for Nanoparticle Research. *Chemical Reviews*. American Chemical Society September 28, 2016, pp 11128–11180. https://doi.org/10.1021/acs.chemrev.5b00690.

(163) Brzustowicz, M. R.; Brunger, A. T. X-Ray Scattering from Unilamellar Lipid Vesicles. *J Appl Crystallogr* **2005**, *38* (1), 126–131. https://doi.org/10.1107/S0021889804029206.

(164) Levine, Y. K.; Wilkins, M. H. F. Structure of Oriented Lipid Bilayers. *Nat New Biol* **1971**, *230* (11), 69–72. https://doi.org/10.1038/newbio230069a0.

(165) Wilkins, M. H. F.; Blaurock, A. E.; Engelman, D. M. Bilayer Structure in Membranes. *Nat New Biol* **1971**, *230* (11), 72–76. https://doi.org/10.1038/newbio230072a0.

(166) Blaurock, A. E. Locating Protein in Membranes. *Nature* **1973**, *244* (5412), 172–173. https://doi.org/10.1038/244172a0.

(167) Blaurock, A. E.; Lieb, W. R. X-Ray Diffraction Studies of Biomembranes. *Nature* **1975**, *255* (5507), 370–371. https://doi.org/10.1038/255370a0.

(168) Atkinson, D.; Hauser, H.; Shipley, G. G.; Stubbs, J. M. Structure and Morphology of Phosphatidylserine Dispersions. *BBA - Biomembranes* **1974**, *339* (1), 10–29. https://doi.org/10.1016/0005-2736(74)90329-0.

(169) Bouwstra, J. A.; Gooris, G. S.; Bras, W.; Talsma, H. Small Angle X-Ray Scattering: Possibilities and Limitations in Characterization of Vesicles. *Chem Phys Lipids* **1993**, *64* (1–3), 83–98. https://doi.org/10.1016/0009-3084(93)90059-C.

(170) Ilavsky, J.; Jemian, P. R. Irena: Tool Suite for Modeling and Analysis of Small-Angle Scattering. *J Appl Crystallogr* **2009**, *42* (2), 347–353. https://doi.org/10.1107/S0021889809002222.

(171) Breßler, I.; Kohlbrecher, J.; Thünemann, A. F. SASfit: A Tool for Small-Angle Scattering Data Analysis Using a Library of Analytical Expressions. *J Appl Crystallogr* **2015**, *48*, 1587–1598. https://doi.org/10.1107/S1600576715016544.

(172) Konarev, P. V.; Petoukhov, M. V.; Dadinova, L. A.; Fedorova, N. V.; Volynsky, P. E.; Svergun, D. I.; Batishchev, O. V.; Shtykova, E. V. BILMIX: A New Approach to Restore the Size Polydispersity and Electron Density Profiles of Lipid Bilayers from Liposomes Using Small-Angle X-Ray Scattering Data. *J Appl Crystallogr* **2020**, *53*, 236–243. https://doi.org/10.1107/S1600576719015656.

(173) Manalastas-Cantos, K.; Konarev, P. V.; Hajizadeh, N. R.; Kikhney, A. G.; Petoukhov, M. V.; Molodenskiy, D. S.; Panjkovich, A.; Mertens, H. D. T.; Gruzinov, A.; Borges, C.; Jeffries, C. M.; Sverguna, D. I.; Frankea, D. ATSAS 3.0: Expanded Functionality and New Tools for Small-Angle

Scattering Data Analysis. *J Appl Crystallogr* **2021**, *54*, 343–355. https://doi.org/10.1107/S1600576720013412.

(174) Lewis-Laurent, A.; Doktorova, M.; Heberle, F. A.; Marquardt, D. Vesicle Viewer: Online Visualization and Analysis of Small-Angle Scattering from Lipid Vesicles. *Biophys J* **2021**, *120* (21), 4639–4648. https://doi.org/10.1016/j.bpj.2021.09.018.

(175) Trapasso, E.; Cosco, D.; Celia, C.; Fresta, M.; Paolino, D. Retinoids: New Use by Innovative Drug-Delivery Systems. *Expert Opin Drug Deliv* **2009**, *6* (5), 465–483. https://doi.org/10.1517/17425240902832827.

(176) Sodhi, R. K.; Singh, N. Retinoids as Potential Targets for Alzheimer's Disease. *Pharmacol Biochem Behav* **2014**, *120*, 117–123. https://doi.org/10.1016/j.pbb.2014.02.016.

(177) Duester, G. Retinoic Acid Synthesis and Signaling during Early Organogenesis. *Cell* **2008**, *134* (6), 921–931. https://doi.org/10.1016/j.cell.2008.09.002.

(178) A., T.; A., K.; H., G. Update in Retinoid Therapy of Acne. *Dermatol Ther* **2006**, *19* (5), 272–279.

(179) Van De Kerkhof, P. C. M. Update on Retinoid Therapy of Psoriasis in: An Update on the Use of Retinoids in Dermatology. *Dermatol Ther* **2006**, *19* (5), 252–263. https://doi.org/10.1111/j.1529-8019.2006.00082.x.

(180) Lens, M.; Medenica, L. Systemic Retinoids in Chemoprevention of Non-Melanoma Skin Cancer. *Expert Opin Pharmacother* **2008**, *9* (8), 1363–1374. https://doi.org/10.1517/14656566.9.8.1363.

(181) Ferreira, R.; Napoli, J.; Enver, T.; Bernardino, L.; Ferreira, L. Advances and Challenges in Retinoid Delivery Systems in

Regenerative and Therapeutic Medicine. *Nat Commun* **2020**, *11* (1). https://doi.org/10.1038/s41467-020-18042-2.

(182) Temova Rakuša, Ž.; Škufca, P.; Kristl, A.; Roškar, R. Retinoid Stability and Degradation Kinetics in Commercial Cosmetic Products. *J Cosmet Dermatol* **2021**, *20* (7), 2350–2358. https://doi.org/10.1111/jocd.13852.

(183) Jin, Y.; Teh, S. S.; Lau, H. L. N.; Xiao, J.; Mah, S. H. Retinoids as Anti-Cancer Agents and Their Mechanisms of Action. *Am J Cancer Res* **2022**, *12* (3), 938–960.

(184) Cristiano, M. C.; Cosco, D.; Celia, C.; Tudose, A.; Mare, R.; Paolino, D.; Fresta, M. Anticancer Activity of All-Trans Retinoic Acid-Loaded Liposomes on Human Thyroid Carcinoma Cells. *Colloids Surf B Biointerfaces* **2017**, *150*, 408–416. https://doi.org/10.1016/j.colsurfb.2016.10.052.

(185) Zhang, Y.; Zhao, J.; Sun, J.; Huang, L.; Li, Q. Targeting Lung Cancer Initiating Cells by All-Trans Retinoic Acid-Loaded Lipid-Plga Nanoparticles with Cd133 Aptamers. *Exp Ther Med* **2018**, *16* (6), 4639–4649. https://doi.org/10.3892/etm.2018.6762.

(186) Cardarelli F., B. F. T. P. M. ; C. G. ; P. D. Determination of the Supramolecular Organization of Encapsulated Molecules by Luminescence Lifetime Analysis. WO2022097108A1, 2021.

(187) Tentori, P.; Signore, G.; Camposeo, A.; Carretta, A.; Ferri, G.; Pingue, P.; Luin, S.; Pozzi, D.; Gratton, E.; Beltram, F.; Caracciolo, G.; Cardarelli, F. Fluorescence Lifetime Microscopy Unveils the Supramolecular Organization of Liposomal Doxorubicin. *Nanoscale* **2022**, *14* (25), 8901–8905. https://doi.org/10.1039/d2nr00311b.

(188) Weber, G. Resolution of the Fluorescence Lifetimes in a Heterogeneous System by Phase and Modulation

Measurements. *Journal of Physical Chemistry* **1981**, *85* (8), 949–953. https://doi.org/10.1021/j150608a006.

(189) Bernardi, M.; Cardarelli, F. Nanoscopy on Drug-Encapsulating Nanosystems by Phasor-Based Fluorescence Lifetime Analysis. *Biophys J* **2023**, *122* (3S1). https://doi.org/10.1016/j.bpj.2022.11.1585.

(190) Ranjit, S.; Malacrida, L.; Jameson, D. M.; Gratton, E. Fit-Free Analysis of Fluorescence Lifetime Imaging Data Using the Phasor Approach. *Nat Protoc* **2018**, *13* (9), 1979–2004. https://doi.org/10.1038/s41596-018-0026-5.

(191) Kasian, N.; Vashchenko, O.; Budianska, L.; Brodskii, R.; Lisetski, L. Cooperative Domains in Lipid Membranes. *J Therm Anal Calorim* **2019**, *136* (2), 795–801. https://doi.org/10.1007/s10973-018-7695-8.

(192) Malacrida, L.; Ranjit, S.; Jameson, D. M.; Gratton, E. The Phasor Plot: A Universal Circle to Advance Fluorescence Lifetime Analysis and Interpretation. *Annu Rev Biophys* **2021**, *50*, 575–593. https://doi.org/10.1146/annurev-biophys-062920-063631.

(193) Cametti, C.; De Luca, F.; Macrì, M. A.; Maraviglia, B.; Sorio, P. Audio to Microwave Frequency Dielectric Study of the Pretransition Region in DPL-Water Systems. *Liq Cryst* **1988**, *3* (6–7), 839–845. https://doi.org/10.1080/02678298808086541.

(194) Katsaras, J.; Tristram-Nagle, S.; Liu, Y.; Headrick, R. L.; Fontes, E.; Mason, P. C.; Nagle, J. F. Clarification of the Ripple Phase of Lecithin Bilayers Using Fully Hydrated, Aligned Samples. *Phys Rev E Stat Phys Plasmas Fluids Relat Interdiscip Topics* **2000**, *61* (5), 5668–5677. https://doi.org/10.1103/PhysRevE.61.5668.

(195) Wack, D. C.; Webb, W. W. Synchrotron X-Ray Study of the Modulated Lamellar Phase P in the Lecithin-Water System. *Phys Rev A (Coll Park)* **1989**, *40* (5), 2712–2730. https://doi.org/10.1103/PhysRevA.40.2712.

(196) Viitala, L.; Pajari, S.; Gentile, L.; Määttä, J.; Gubitosi, M.; Deska, J.; Sammalkorpi, M.; Olsson, U.; Murtomäki, L. Shape and Phase Transitions in a PEGylated Phospholipid System. *Langmuir* **2019**, *35* (11), 3999–4010. https://doi.org/10.1021/acs.langmuir.8b03829.

(197) Leekumjorn, S.; Sum, A. K. Molecular Studies of the Gel to Liquid-Crystalline Phase Transition for Fully Hydrated DPPC and DPPE Bilayers. *Biochim Biophys Acta Biomembr* **2007**, *1768* (2), 354–365. https://doi.org/10.1016/j.bbamem.2006.11.003.

(198) Wu, H. L.; Tong, Y.; Peng, Q.; Li, N.; Ye, S. Phase Transition Behaviors of the Supported DPPC Bilayer Investigated by Sum Frequency Generation (SFG) Vibrational Spectroscopy and Atomic Force Microscopy (AFM). *Physical Chemistry Chemical Physics* **2016**, *18* (3), 1411–1421. https://doi.org/10.1039/c5cp04960a.

(199) Leonenko, Z. V.; Finot, E.; Ma, H.; Dahms, T. E. S.; Cramb, D. T. Investigation of Temperature-Induced Phase Transitions in DOPC and DPPC Phospholipid Bilayers Using Temperature-Controlled Scanning Force Microscopy. *Biophys J* **2004**, *86* (6), 3783–3793. https://doi.org/10.1529/biophysj.103.036681.

(200) Drazenovic, J.; Wang, H.; Roth, K.; Zhang, J.; Ahmed, S.; Chen, Y.; Bothun, G.; Wunder, S. L. Effect of Lamellarity and Size on Calorimetric Phase Transitions in Single Component Phosphatidylcholine Vesicles. *Biochim Biophys Acta Biomembr*

2015, *1848* (2), 532–543. https://doi.org/10.1016/j.bbamem.2014.10.003.

(201) Neunert, G.; Tomaszewska-Gras, J.; Baj, A.; Gauza-Włodarczyk, M.; Witkowski, S.; Polewski, K. Phase Transitions and Structural Changes in Dppc Liposomes Induced by a 1-Carba-Alpha-Tocopherol Analogue. *Molecules* **2021**, *26* (10). https://doi.org/10.3390/molecules26102851.